Evolution of trailing vortices around a ship hull at large drift angle

Vom Promotionsausschuss der
Technischen Universität Hamburg

zur Erlangung des akademischen Grades

Doktor-Ingenieur (Dr.-Ing.)

genehmigte Dissertation

von
Dag-Frederik Feder

aus
Wildeshausen

2021

Vorsitzender des Prüfungsausschusses
Prof. Dr.-Ing. Otto von Estorff

Gutachter
1. Gutachter: Prof. Dr.-Ing. Moustafa Abdel-Maksoud
2. Gutachter: Prof. Dr.-Ing. habil. Nikolai Kornev

Tag der mündlichen Prüfung
30. November 2021

Digital Object Identifier (DOI): 10.15480/882.4045

https://orcid.org/0000-0001-9777-7112

Acknowledgements

This thesis is the result of five years of research at the Institute for Fluid Dynamics and Ship Theory (FDS) at Hamburg University of Technology (TUHH). I would like to thank my supervisor Prof. Dr.-Ing. Moustafa Abdel-Maksoud for this opportunity, for his trust in me and his support and for getting to know interesting people during my research. In addition to research, I very much appreciated the exchange with students and the deepening of the content in the context of exercises I held for the following lectures: ship vibrations, analysis of maritime systems and cavitation.

Furthermore, I would like to thank Prof. Dr.-Ing. habil. Nikolai Kornev for reviewing my thesis and Prof. Dr.-Ing. Otto von Estorff for chairing the examination board. My work was funded by the German Research Foundation (DFG), grant 263936466, and by the Office of Naval Research (ONR) Global, Grant N62909-18-1-2080, under the administration of Drs. W.-M. Lin, S. Ahmed, P. Rose and E. McCarthy. This support is gratefully acknowledged.

Dr.-Ing. Ivan Shevchuk helped me a lot with OpenFOAM and turbulence issues in general, I am very grateful for this. My first Foam teacher also came from LEMOS at University of Rostock: thanks to Dr.-Ing. Nawar Abbas for the valuable and pleasant time we spent together. And many thanks to Dr.-Ing Ulf Göttsche for his helpfulness with general software trouble. I would like to thank Prof. Frederick Stern as well as Prof. Visonneau and his team for valuable discussions about turbulence modelling and vortex flows. And thanks to my research assistant Lukas Gerwers for fruitful discussions about circulation and the nice cooperation. Furthermore, special thanks to Alissa for taking care of English grammar and spelling errors.

I had many great teachers during my schooldays. I would particularly like to thank Alexander Jahn for his motivation and encouragement, and Albert Paschke, from whom I learned a lot about writing.

The open-source software tools Linux, OpenFOAM, Octave, Python, LaTeX as well as PGFPlots have proven to be very powerful: I am very grateful to the developers for their work and openness.

My office colleagues helped me to enjoy the time at university, thanks to Dr. Eng. Youjiang Wang, Christian Schulz and Chen Zeng for the pleasant atmosphere, valuable technical discussions and all other conversations. In addition, I was happy to spend enjoyable time with Dr.-Ing. Stephan Berger, Dr. Franz von Bock, Stefan Netzband, Ahmed Sahab, Dr.-Ing. Ivan Shevchuk and Hendrik Simonis. And: I am very happy about the awesome doctor hat!

My grandpa Rolf taught me to love the sea which is why I became a naval architect with a passion for hydrodynamics. That's why I dedicate this thesis to him!

Completing the work took a lot of free time, while my children were well looked after. Many thanks for that to my family, especially my wife for any time, my mother, Omama and Andreas for the weekend days and Omama also for the mondays, Tante Gerhild during the move, Werner for time on the farm, Lisa and Micha for the days at the end of 2020 as well as my grandparents for the thursdays. And thanks to Andreas for 'his' desk.

My two children helped me to complete the work simply by being there or expected and I wanted to spend my time with you, thanks for that to Hannes and Linnea.

My wife Sophia is magnificent. She believed in me, she had a lot of patience and she worked even harder to give me time so that I could finish the thesis the way I wanted. My greatest thanks goes to you. Besides, she always provides valuable knowledge on systems and control theory.

This thesis has taken up a lot of space in my life at times, and my family is now getting it back: that's done, let's go out!

Dag Feder, December 19, 2021

Abstract

The two major trailing vortices close to the KVLCC2 model at 30° static drift and $Re_{L_{oa}} \approx 2.6 \cdot 10^6$ are investigated within the framework of the present thesis. Numerical flow simulations with a hybrid RANS-LES model, the SST-based IDDES proposed by Gritskevich et al. (2012), were conducted with OpenFOAM. This accounts for the unsteady and inhomogeneous wake field contrary to RANS models with curvature correction. Inside the wake, the fore-body side vortex (FSV) and the aft-body bilge vortex (ABV) mark coherent vortices subjected to transverse motions, wandering. Although both vortices are located close to the hull wandering reveals a relative amplitude comparable to Devenport, Rife et al. (1996) and grows linearly. The analysis of 2D flow correlations with proper orthogonal decomposition indicates that wandering is excited by the surrounding free-shear layer. The following vortex characteristics are examined in detail: vortex wandering and its interaction with core turbulence, and the axial velocity overshoot. Furthermore, a brief analysis is conducted for vortex interactions and instability phenomena.

In addition to the in-plane displacement of the vortex, the bending (or curvature) of the vortex axis is considered to form part of wandering too. Although the results may be exaggerated they indicate a considerable bending which means that the vorticity vectors rotate around the mean vortex axes. Therefore, the correction of the flow at vortex planes for the wandering motion would become questionable as the assignment of the planes may render ambiguous. So only the flow at the vortex centre is corrected for the wandering motion. Three different representations for the vortex centre are compared.

As expected, vorticity and pressure extrema are smoothed out due to wandering. This is different for the axial velocity which is highly turbulent indeed. The flow at the FSV and ABV centre reveals a distinct inertial sub-range that represents nearly isotropic turbulence. However, about two thirds of TKE originate from wandering for the FSV. For the ABV the contribution is less which is an indication for the proximity to the stern separation.

The interaction between the FSV pair from the double-body is negligible. And the FSV seems to be subjected to a vortex breakdown at the after shoulder.

Contrary to Anderson, Lawton (2001) no linear relation between the vortex circulation and the axial velocity reveals for the FSV. However, difficulties in determining the unique vortex circulation do not allow a clear conclusion. The deviating results are set in relation to the different scope.

(Deutsch) Die beiden großen nachlaufenden Wirbel in der unmittelbaren Umgebung des KVLCC2-Modells bei 30° Drift und $Re_{L_{oa}} \approx 2.6{\cdot}10^6$ werden im Rahmen der vorliegenden Arbeit untersucht. Numerische Strömungssimulationen mit einem hybriden RANS-LES-Modell, dem SST-basierten IDDES-Modell von Gritskevich et al. (2012), wurden mit OpenFOAM durchgeführt. Damit kann der instationäre und inhomogene Nachstrom berücksichtigt werden, im Gegensatz zu RANS-Modellen mit Krümmungskorrektur. Im Nachstrom sind der fore-body side vortex (FSV) und der aft-body bilge vortex (ABV) als kohärente Wirbel ausgebildet, die Querbewegungen ausgesetzt sind und wandern. Obwohl beide Wirbel nah am Rumpf liegen, weist die relative Wanderbewegung eine vergleichbare Amplitude auf wie in Devenport, Rife et al. (1996) und wächst linear. Die Analyse von 2D-Strömungskorrelationen mit der Methode *proper orthogonal decomposition* zeigt, dass das Wandern von der Umgebung angeregt wird. Im Detail werden folgende Wirbeleigenschaften untersucht: Wandern und die Wechselwirkung mit Turbulenz im Kern, sowie die axiale Übergeschwindigkeit. Außerdem wird eine kurze Analyse von Wirbel-Wechselwirkungen und Instabilitätsphänomenen durchgeführt.

Neben der Verschiebung des Wirbels in der Ebene wird die Krümmung der Wirbelachse als Teil der Wanderbewegung berücksichtigt. Obwohl die Ergebnisse nicht eindeutig sind, deutet sich eine ausgeprägte Krümmung an, die aufzeigt, dass die Wirbelstärke-Vektoren um die mittlere Achse drehen. Dann könnte die Korrektur der Strömung in Wirbelebenen um die Wanderbewegung fragwürdig werden, weil die Zuordnung der Ebenen nicht mehr eindeutig wäre. Daher wird nur die Strömung im Wirbelzentrum um die Wanderbewegung korrigiert. Dabei werden drei verschiedene Darstellungen für das Wirbelzentrum verglichen.

Erwartungsgemäß werden Extrema von Wirbelstärke und Druck durch das Wandern geglättet; was nicht für die axiale Geschwindigkeit gilt, die deutlich turbulenter ist. Die Strömung im FSV- und ABV-Zentrum zeigt einen ausgeprägten Trägheitsbereich, der nahezu isotrope Turbulenz darstellt. Etwa zwei Drittel von TKE stammen dabei aus der Wanderbewegung für den FSV. Beim ABV ist der Beitrag geringer, was möglicherweise aus der Nähe zur Ablösung folgt.

Die Wechselwirkung zwischen dem FSV-Paar aus dem Doppelrumpf ist vernachlässigbar. Und der FSV scheint an der hinteren Schulter aufzuplatzen *(vortex breakdown)*. Im Gegensatz zu Anderson, Lawton (2001) tritt hier kein linearer Zusammenhang zwischen der Wirbelzirkulation und der axialen Geschwindigkeit auf. Schwierigkeiten bei der Bestimmung der Wirbelzirkulation lassen allerdings keine eindeutige Aussage zu. Die abweichenden Ergebnisse werden in Relation gesetzt zu den unterschiedlichen Strömungsfällen.

Contents

List of Tables v

List of Figures vi

1. Introduction 1
- 1.1. Motivation and Aim . . . 1
- 1.2. Approach . . . 6
- 1.3. Structure of the Thesis . . . 9

2. Trailing Vortices: a Review of the Characteristics 10
- 2.1. What is a Trailing Vortex? . . . 10
- 2.2. Wingtip Vortices: Characteristics . . . 18
  - 2.2.1. Wandering . . . 18
  - 2.2.2. Core Turbulence . . . 22
  - 2.2.3. Axial Velocity . . . 24
  - 2.2.4. Interactions and Instabilities . . . 25
- 2.3. Ship Test Cases . . . 28
  - 2.3.1. KVLCC2 . . . 28
  - 2.3.2. Other Hulls and Similar Bodies . . . 31

3. Turbulence Modelling 34
- 3.1. Turbulence as a Phenomenon . . . 34
- 3.2. Turbulence Modelling . . . 35
  - 3.2.1. Reynolds-Averaged Navier-Stokes (RANS) Equations . . . 36
  - 3.2.2. RANS Turbulence Models . . . 37
  - 3.2.3. Hybrid RANS-LES Models . . . 39

4. Test-Case Setup 44
- 4.1. Experiments . . . 44
- 4.2. Physical Aspects . . . 45
- 4.3. Numerical Aspects . . . 46

5. Numerical Results 51
- 5.1. The Vortex System . . . 51
  - 5.1.1. Different Drift Angles . . . 52
  - 5.1.2. Steady Drift of 30° . . . 54
- 5.2. Verification . . . 61

5.3. Wandering Analysis 63
5.4. Vortex Core Flow 70
5.5. Vortex Centre Flow 80
5.6. Summary of Major Findings 90

6. Conclusions **97**
6.1. Summary and Discussion 97
6.2. Outlook 99

Bibliography **101**

A. Existing Experiments **111**

B. Further Details on the Vortex Flow **112**
B.1. General Flow Variables 112
B.2. Numerical Setup 113
B.3. Drift Angle Influence 113
B.4. Verification 115
B.5. Flow Visualisation 120
B.6. Wandering Analysis 121
B.7. Vortex Core Flow 123
B.8. Vortex Centre Flow 125

List of Tables

2.1. Dimensions of KVLCC2 model. 29

4.1. Positions of measuring planes. 46
4.2. Mesh details. 47
4.3. Simulation matrix. 48

A.1. Classification of existing experiments of the vortex system of KVLCC2. . 111

List of Figures

1.1. Lifting wings in different applications creating trailing vortices. 2
1.2. Visualisation of vortex flow instabilities. 3
1.3. Initial vortex formation from wingtip and ship hull. 4
1.4. Comparison of resolved vortical structures for different drift angles. 5
1.5. The vortex system and naming convention. 7

2.1. Interpretations of the wingtip origin. 12
2.2. Formation of swirling vortex flow. 13
2.3. Profiles of a q-vortex. 16
2.4. Exemplary alignment of the instantaneous vortex axis. 19
2.5. Influence of wandering on wingtip vortex. 20
2.6. In-plane Reynolds-shear strain and stress pattern: four-leaf clover. 24
2.7. Visualisations of vortex breakdown. 27
2.8. Vortex system around JBC and DTMB5415. 28

3.1. Comparison of laminar and turbulent separating boundary layer flows. . . 34
3.2. Schematic distinction between RANS- and LES-part. 41

4.1. Arrangement of the double-body model inside the wind-tunnel. 44
4.2. Visualisation of the numerical mesh. 50

5.1. Vortex system for different drift angles. 52
5.2. Vorticity in transom stern plane for different drift angles. 53
5.3. Turbulence in transom stern plane for different drift angles. 54
5.4. Vortex system around double-body model from rear view. 55
5.5. Hull body plan with FSV and ABV, core radius and wandering amplitude. 56
5.6. Visualisation of flow around the vortices. 57
5.7. Visualisation of possible vortex breakdown of FSV. 58
5.8. Visualisation of vortex interactions. 59
5.9. Profiles through FSV. 60
5.10. Profiles through ABV. 61
5.11. Resolved TKE around initial FSV. 62
5.12. Absolute resolved TKE in stern region. 62
5.13. Exemplary wandering formation. 63
5.14. Visualisation of exemplary vortex wandering. 64
5.15. Wandering characteristics of FSV. 67

5.16. Wandering characteristics of ABV. 68
5.17. Angle between vortex axis and x-axis. 68
5.18. Wandering amplitude for different inflow speed. 69
5.19. Correlation coefficient of FSV wandering motion for double-body model. . 69
5.20. Vortex core parameters for FSV and ABV. 71
5.21. Stress-strain lag around FSV at X12. 72
5.22. Stress-strain lag around ABV at X15. 74
5.23. POD analysis of FSV at X12 76
5.24. POD analysis along streamwise evolution of FSV. 77
5.25. Vortex system for different inflow speed. 77
5.26. Flow in FSV planes for varied inflow speed. 78
5.27. Turbulence and its production in a plane through the FSV. 79
5.28. Vortex core parameters for FSV at varied inflow speed. 80
5.29. Comparison of FSV and ABV centre for the different representations. . . 81
5.30. Time-averaged and wandering-corrected flow at FSV swirling centre. . . . 82
5.31. Turbulence at the FSV centre. 83
5.32. Time-averaged and wandering-corrected flow at ABV swirling centre. . . . 84
5.33. Turbulence at the ABV centre. 85
5.34. Portion of TKE originating not from wandering. 86
5.35. Power spectral density for FSV and ABV. 87
5.36. TKE at the swirling centre c1 for varied inflow speed. 88
5.37. Velocity at FSV's centre for different inflow speed. 89

B.1. Visualisation of the numerical mesh close to the hull. 113
B.2. Relative resolved TKE in transom stern plane for different drift angles. . . 114
B.3. Axial flow in transom stern plane for different drift angles. 114
B.4. Blending factor for convection discretisation. 115
B.5. Subdivision of hybrid RANS-LES approach into RANS- and LES-part. . . 115
B.6. Relative resolved TKE for different inflow speed: FSV. 116
B.7. Resolved part of TKE in relation to total one in stern region. 116
B.8. Power spectral density for different mesh resolutions. 117
B.9. Grid study of the flow at the vortex centre: FSV. 118
B.10. Grid study of the flow at the vortex centre: ABV. 119
B.11. Vortex system: 2D front and rear view. 120
B.12. Vortex system: 2D side view. 120
B.13. Vortex system for different isovalues. 121
B.14. Vortex system on different grids. 121
B.15. Wandering amplitude and core radius: FSV. 122
B.16. Angle between vortex axis and coordinate axes y and z: FSV. 122
B.17. Vortex angle for different inflow speed. 123
B.18. Principal axes and RMS of FSV wandering (double-body). 123
B.19. In-plane shear stress for q-vortex wandering related to CFD. 124
B.20. Flow around FSV for varying inflow speed. 125

B.21. Influence of wandering on different representations for the 'axial' velocity. 126
B.22. Exemplary visualisation of the different centre representations. 126
B.23. Flow at different centre representations: FSV. 127
B.24. Flow at different centre representations: ABV. 129
B.25. Axial velocity for varying inflow speed: ABV. 129
B.26. Helicity at FSV's centre for different inflow speed. 130
B.27. Axial velocity as a function of vortex circulation: FSV. 130
B.28. Comparison of single- and double-body flow at FSV centre. 130
B.29. Wandering-corrected Reynolds-stress components: FSV. 131
B.30. Wandering-corrected Reynolds-stress components: ABV. 131
B.31. Time-averaged and wandering-corrected TKE: ABV. 132
B.32. Power spectral density for different velocity components. 132

1. Introduction

The topic of this thesis is the analysis of physical characteristics of the vortex centre flow. The scope is the wake within the immediate vicinity (up to an eighth dowmstream of the transom stern) of a full-block ship hull with a large drift angle. The actual test case is the KVLCC2 model with a drift angle of 30° and Reynolds number of about $2.6 \cdot 10^6$. A turbulence-resolving hybrid RANS-LES model is used to predict the vortex flow where the revelation of the following vortex characteristics drives the analysis: wandering[1], core turbulence, axial velocity surplus and interactions and instabilities.

The thesis' focus is laid on trailing vortices as a dynamic pattern within the flow. This is why it begins with vortices in general and subsequently emphasises the peculiarities of the present case.

1.1. Motivation and Aim

Lifting wings fulfil a human dream: they make them fly. And flying is just one amazing application of 'lifting surfaces' out of a great many: in terms of technical propulsion, rotating wings arranged as a propeller accelerate airplanes to high speeds or push huge ships through the ocean. Ships exposed to side-wind keep course as the hull produces lift in drift condition. Windsurfers plane on the water using a sail to generate thrust and a fin to keep course. Fishes use fins to locomote, spoilers push fast cars to the ground, and there are many more examples.

A well known consequence of lifting surfaces is the emergence of vortices from the wingtip: so-called wingtip or tailing vortices, exemplary depicted in Fig. 1.1. These vortices are a direct consequence of the lift: according to an intuitive explanation, the pressure difference between pressure and suction side triggers the flow to bend around the tip and form a swirling pattern.[2] Various phenomena accompany the presence of trailing vortices that are mentioned in the following paragraph.

A wingtip vortex acts back onto the wing's lift, as the induced velocities reduce the effective angle of attack and result in a reduced lift-to-drag ratio, a phenomenon called induced drag (Green 1995, p. 430). Due to the pressure decrease inside the vortex, water

[1] Wandering denotes the coherent, transverse motion of a vortex, refer also Sec. 2.2.1.
[2] See Sec. 2.1 for further details and other explanations.

(a) Distinct wingtip vortex visualised by condensation at takeoff, photo by M. Visser/ CC BY-SA 2.0.

(b) Smoke retracted into wingtip vortices, photo by Jez B/ CC BY-NC-ND 2.0 (clipped).

(c) Flight of birds in V-formation where following birds benefit from the vortex-induced upwash, photo by B. Fritsch/ CC BY 2.0.

(d) Air-propeller tip vortex visualised by condensation, photo by M. Visser/ CC BY-SA 2.0 (clipped).

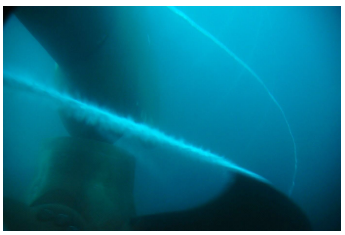

(e) Ship-propeller tip vortex visualised by cavitation. Photograph through window in hull (Schiller et al. 2013).

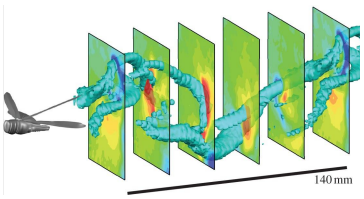

(f) Visualisation of desert locust wake with T-PIV showing a full stroke (Bomphrey et al. 2012).

Figure 1.1.: Lifting wings in different applications creating trailing vortices. A review of the latter's technological relevance can e.g. be found in Green (1995, p. 430).

may condensate[3] or evaporate (vortex cavitation, see e.g. Franc, Michel (2006, ch. 10)) - and so visualises the vortex. Trailing vortices as a flow pattern possess some distinct peculiarities: the vortex core size is considerably smaller than wing dimensions (it scales with the boundary layer thickness) and the spatial mean-flow gradients inside the core are huge (e.g. about 100 m/s peak swirling flow for a landing Boeing 757, see Sec. 2.1). During roll-up, the wing's bound circulation continuously enters the vortex, or in other words the shed vorticity accumulates in the tip vortex: this free-shear layer introduces retarded flow and turbulence into the vortex core. A consequence of the swirling flow is the pressure decrease that accelerates the axial flow. Depending on the balance with the retarding boundary-layer influence, there may be a velocity deficit or excess. A deviation of the axial velocity from the undisturbed inflow poses another source for turbulence production whereas the swirling flow stabilises and sometimes relaminarises the

[3]The pressure drop goes along with a temperature decrease that drives the condensation or even freezing (Green 1995, p. 434).

(a) Contrails visualise long-wave-type or Crow-instability where two vortices interact, superimposed by short-wave instabilities, photo by G. Beltz/ CC BY 2.0.

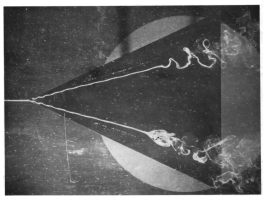

(b) Dye visualises short-wave instabilities: delta wing at large incidence showing both types of vortex breakdown, from Lambourne, Bryer (1961, p. 23), see also Fig. 2.7.

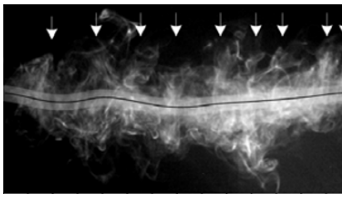

(c) Instantaneous wingtip vortex axis, from Bailey et al. (2018) with spatial variation of displacement from mean centre position and surrounding secondary azimuthal structures, see also Fig. 2.4.

Figure 1.2.: Visualisation of exemplary effects of trailing vortices that reveal different types of instabilities, small-scale surrounding structures and axis displacement also known as wandering.

incoming turbulent free-shear-layer flow. The latter is the reason for vortex persistence over sometimes thousands of wing chords (Green 1995, p. 458). Vortex unsteadiness is usually present, even a laminar or axisymmetric vortex generally reacts to surrounding perturbations. Vortices may interact in various scenarios, e.g. as co- or counter-rotating ones, where full wings generate vortex pairs of the latter type. Additionally, they may experience a sudden transformation from ordered to disordered flow pattern during vortex breakdown. Exemplary vortex flows are visualised in Fig. 1.2. The thorough analysis of the vortex core flow for a distinct case is the topic of the present thesis.

Previous and current investigations cover all mentioned aspects in the near (Chow et al. 1997b) and far field[4] (Devenport, Rife et al. 1996), with varying degrees of Reynolds and Mach numbers or free-stream turbulence (Bailey et al. 2018), with multiphase flows (Franc, Michel 2006, ch. 10) and within all kinds of applications. The investigations often bear an airplane context focussing far-field questions like vortex persistence and possible interactions with following aircrafts or helicopter blades (see e.g. Jacquin, Pantano (2002) and P. R. Spalart (1998)).

In contrast, the present research focusses the near field close to the body which is relevant for a ship hull at drift conditions. Figure 1.3 reveals the main differences between typical wings and a ship hull in drift condition:[5] first, the aspect ratio of a ship is much smaller[6] which implies a less homogeneous and more unsteady wake flow compared to a wing

[4] A distinction of the near and far field is provided in Sec. 2.1.

[5] Admittedly, the incidence differs by 20° but as shown e.g. in Fig. 5.1 at least two distinct trailing vortices would emerge from the present hull at a similar angle of attack of 12°.

[6] For example, the aspect ratio of the A380 and Boeing 777 is around 9, a typical sailplane has an even higher ratio of more than about 30 whereas commercial ships have an aspect ratio considerably below unity as the draught is much smaller than its length.

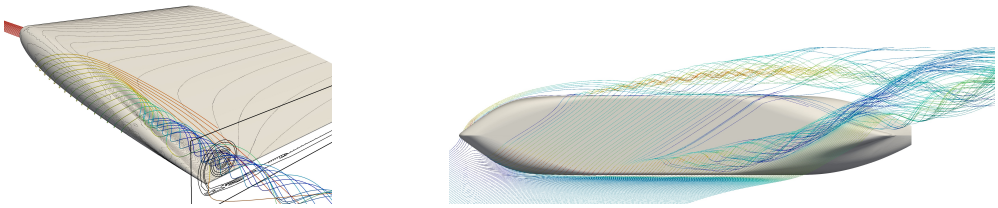

(a) Wing test case from Chow et al. (1997a) with small aspect ratio, one separation line for single tip vortex, see also Fig. 2.2.

(b) Current ship hull at drift with three dominant initial vortices from windward bilge, leeward bow and stern, see also Fig. 1.5.

Figure 1.3.: Initial formation of trailing vortices shed from smooth wingtip shape and blunt ship hull. Streamlines of time-averaged flow predicted with CFD.

with a high aspect ratio. Second, the 'tip' shape of a ship is less smooth and more blunt compared to wings which leads to the separation of multiple initial vortices that merge further downstream. The focus on the near field for the present case in contrast to the far field for typical wings implies a vortex flow with a higher level of inhomogeneity and unsteadiness.[7] Summarising, the **scope** of the present thesis comprises the near field of two trailing vortices shed from a ship hull in drift condition with large incidence. Therefore, the flow at the distinct vortex centre is the major aspect investigated. In addition, the surrounding vortex core flow is also treated and the global vortex wake is discussed in short.

There are few benchmarking ships whose vortex wake was intensively investigated, this is essentially the surface combatant DTMB5415, the bulk carrier JBC and the present hull of a crude carried KVLCC2.[8] Compared to typical wings, the angles of attack studied are higher, between 10° and 30°. The choice of KVLCC2 was motivated by previous investigations at TUHH that left open questions on the vortex characteristics for both EFD and CFD (Abdel-Maksoud et al. 2015). The **aim** of the thesis is to provide a contribution to answering fundamental questions of vortex flows for the mentioned scope. In comparison to previous investigations on ship hulls (discussed in Sec. 2.3) the dynamic evolution of the vortex marks the thesis' focus similar to approaches of aerodynamic investigations on wingtip vortices (in the far field). The present results will be compared to the aerodynamic scope. The following aspects will be examined: the wandering motion and its interaction with turbulence, the velocity excess and briefly also the interaction of vortex pairs and instability phenomena; which raise some questions:

[7] This is discussed e.g. by Green (1995, p. 463) and Devenport, Rife et al. (1996, p. 68): in contrast to the vortex far field after about two to three chord lengths downstream, the near field flow is rather complex driven by the proximity to the separation of the free-shear layer. In addition, the leeward vortex of ship hulls shows some similarities to the leading-edge vortex along delta-wings that is prone to become instable.

[8] KVLCC2 and JBC are full-block hulls and DTMB5415 is slender and the vortex system dominated by the sonar dome separation. So the latter case owns distinct differences compared to commercial hulls.

- Wingtip vortices: where are differences to trailing vortices emerging from wings?
- Turbulence: is the flow at the vortex centre turbulent? How large is the contribution of a possible transverse vortex motion?
- 'Wandering'[9]: is there a coherent transverse motion of the vortex itself and, if so, how does it compare to far-field cases of wingtip vortices? What could be the origin and what's the consequence?
- Axial velocity excess: does the excess correlate with the vortex circulation like beyond wingtip vortices (Anderson, Lawton 2001)?
- Double-body influence: is there an interaction of the counter-rotating FSV pair as they are close together?

Using turbulence resolving numerical methods (hybrid RANS-LES or DES) the two major wake vortices around the KVLCC2 hull will be investigated at a 30° drift angle. For this high drift angle, the modelling error of the underlying hybrid RANS-LES approach reduces to an acceptable level, because strong inherent flow instabilities assure a fast natural development of resolved turbulent structures, see also Fig. 1.4.[10] Larsson, Stern,

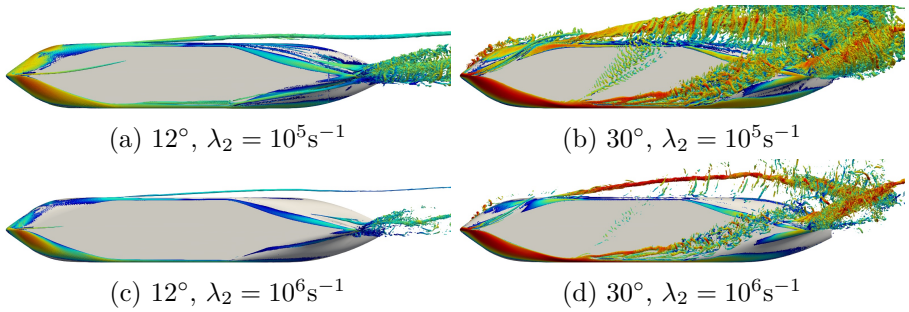

(a) 12°, $\lambda_2 = 10^5 s^{-1}$ (b) 30°, $\lambda_2 = 10^5 s^{-1}$

(c) 12°, $\lambda_2 = 10^6 s^{-1}$ (d) 30°, $\lambda_2 = 10^6 s^{-1}$

Figure 1.4.: Resolved vortical structures for two drift angles for two isovalues λ_2: for 12° the different isovalues reveal that no secondary structures surround the leeward vortex. These structures should separate from the bottom boundary layer. In contrast, for 30° there are plenty of resolved tiny eddies that represent the proper resolution of the hybrid RANS-LES turbulence model. Coarse meshes, isosurfaces coloured by velocity magnitude.

Visonneau (2014, p. 316) state the importance of strong inherent flow instabilities, e.g. due to a blunt hull or a large drift angle, for the proper applicability of partially turbulence resolving models. Furthermore, the high incidence leads to a separated leeward vortex from the hull which increases the reliability of the related experimental measurements because laser-reflections from the wall play a minor role. The choice of a wind tunnel as the testing facility in opposition to a towing tank represents the focus of the investigation on the vortices, the free-surface is omitted but the models needs not to be towed.

[9] A proper definition is provided in Sec. 2.2.1.

[10] The target is to reduce the grey area where the LES lacks turbulent fluctuations, see Sec. 3.2.3 for further information.

From the view of naval architecture, the work's focus tends to be of fundamental character. A steady drift angle of 30° for a huge commercial ship is out of usual operating conditions. But the findings of the vortex core flow analysis do also apply for smaller drift angles in principle - because essentially it's a near-field trailing vortex - which are more difficult to study numerically and experimentally. One question of technical relevance is the degree of non-uniformity and unsteadiness (or in other words, the Reynolds stresses) in the wake field if trailing vortices are present (Abbas, Kornev 2016b; Visonneau, Guilmineau et al. 2020a). Both the coexistence of high vorticity and high turbulence intensity and the stress-strain lag inside the cores cannot be predicted even with sensitised RANS turbulence models. Instead, the resolution of turbulence with a scale-resolving model is necessary, see e.g. Chow et al. (1997a) for a wing geometry or Hino et al. (2021), Kornev, Shevchuk et al. (2019), Larsson, Stern, Visonneau (2014) and Visonneau, Guilmineau et al. (2018) for a ship hull geometry.

As an aside, it is important to mention the reliability of turbulence modelling approaches (RANS) in terms of forces: during manoeuvring high drift angles occur and the flow forces on the hull can be predicted quite accurately with RANS, see e.g. Abbas, Kornev (2016b) and Larsson, Stern, Visonneau (2014). So the improved prediction of the vortex flow with scale-resolving approaches is motivated more by fundamental questions as explained above and not in terms of practical issues concerning the prediction of ship manoeuvrability. In addition, the numerical results and the appertaining postprocessing algorithms provide a basis for future comparison with the corresponding experimental data. At the time of writing the wind-tunnel data was not finally processed.

The next section provides an overview of the test case investigated and of the numerical and experimental methods used within this thesis.

1.2. Approach

The test case KVLCC2 at 30° drift angle and a Reynolds number $Re \approx 2.6 \cdot 10^6$ is investigated numerically with respect to two major trailing vortices. In addition, the numerical results and the appertaining postprocessing algorithms provide a basis for future comparison with the related experimental data. At the time of writing the wind-tunnel data was not finally processed.

Test Case The vortex system, shown in Fig. 1.5, consists of the following trailing vortices, the bold ones will be studied in detail:[11]

[11] A good description of the vortex system can also be found in Fureby et al. (2016, Sec. 5.1).

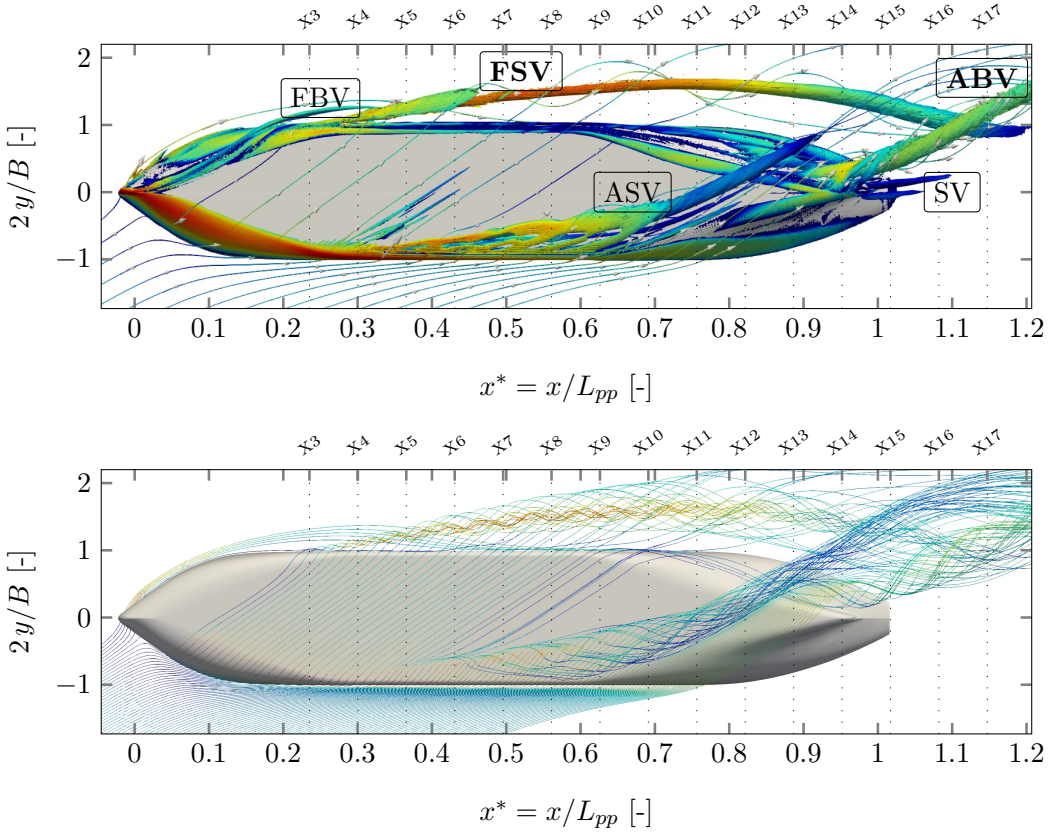

Figure 1.5.: The vortex system, represented by $\overline{\lambda_2} = 10^5 \mathrm{s}^{-1}$ isosurface and exemplary streamlines of different density indicating the swirling vortex flow. Both coloured by velocity magnitude.

- **Fore-body side vortex (FSV)**: it separates near the forward shoulder and extends along the hull with a certain distance. Most of the bottom's boundary layer rolls up into the FSV, there is an initial jet-like core flow, the instantaneous axis displacement increases and finally the vortex becomes unstable downstream of the rear shoulder. Considering a delta wing, the FSV resembles a leading-edge vortex. The vortex core flow is investigated herein.
- **Aft-body bilge vortex (ABV)**: it separates at the ship stern and is initially surrounded by a strong mixing flow due to the large stern separation. There is a merging-like interaction of the co-rotating FSV and ABV. This vortex is studied also in detail.
- Fore-body bilge vortex (FBV): a tiny elongated vortex that bends around the bow section and is entrained by the FSV.

- Aft-body side vortex (ASV): there is a long separation over the midship on the windward bottom that forms a vortex at the rear shoulder which proceeds inside the boundary layer. The vortex tends to diffuse after separating from the hull.
- Stern vortex (SV): the only vortex with a different rotation direction emerges at the stern region.

Additionally, unsteady vortical structures separate from the bow and oblique vortices may extend along the bottom. And secondary vortical structures surround the trailing vortices that originate from the well-defined separation at the blunt edges. The time-averaged streamlines in Fig. 1.5 unveil how the swirling vortex flow dominates the wake. And the entrainment of the separated flow into the FSV (leeward separation), ASV (windward) and ABV (stern). Further, the figures indicate the coordinate system and the placement of the measuring planes X3 to X17 where the FSV and ABV centre flow is analysed thoroughly.

Methods In order to resolve the turbulent vortex core flow properly a **hybrid RANS-LES turbulence model** according to Gritskevich et al. (2012) is used (SST-based IDDES): the hull boundary layer is modelled with RANS and the separated vortex flow with LES. The simulations are conducted with OpenFOAM (Weller et al. 1998).

The analysis of the turbulent flow field which is inherently three dimensional and unsteady, is based on standard statistical algorithms (first and second statistical moments), vortex wandering correction and proper orthogonal decomposition (POD). This forms a basis for a future comparison with 3D wind-tunnel data that was gained with tomographic particle image velocimetry (tomo/T-PIV) and so provides also a temporal and three-dimensional representation of the vortex flow.

Procedure The instantaneous vortex axis is subject to a transverse displacement, called wandering, which marks a central aspect of the thesis: first the wandering motion will be analysed statistically and second its influence on the time-averaged flow will be revealed, or in other words the centre flow is corrected for the wandering motion. Three different local identification schemes for the revelation of the vortex centre will be compared.

With regard to a future comparison of CFD and EFD results, wandering correction may allow the reduction of different influencing factors on the numerical and experimental flow. Apart from inherent modelling and methodological errors there are imperfections of the wind-tunnel setup, e.g. vibrations of the model, that would influence the vortex flow, see e.g. Bailey et al. (2018) and Devenport, Rife et al. (1996).

The motivation for the variation of the inflow speed is given by the following relations: the spatial gradients of the axial core velocity are the major source of turbulence (Chow et al. 1994) and the relative axial velocity excess or decrease at the core correlates strongly with the inflow speed (Anderson, Lawton 2001).[12]

As opposite 'wingtip' vortices like the FSV may interact in terms of long-wave instabilities, the numerical results for a single- and double-body configuration will be compared.

Specifics of the Approach The analysis of the wandering motion and its correction for the centre flow has not been applied to the near field. Here, it is applied to trailing vortices upstream of the trailing edge, i.e. transom stern. In addition, the instantaneous orientation of the vortex axis is considered which reveals a significant bending (or curvature). The results render the correction only for the in-plane displacement (Heyes et al. 2004; Miloud et al. 2020) questionable for the present case. Furthermore, three different centre representations are compared directly.

In terms of vortex interaction and possibly emerging long-wave instabilities of counter-rotating trailing vortices form very-low aspect ratio wings, the numerical analysis comprises the single- and double-body model. The findings of Anderson, Lawton (2001) for the relation between vortex circulation and axial velocity excess/ overshoot will be verified within the near field for the FSV.

1.3. Structure of the Thesis

The detailed description of trailing vortices marks the foundation for the research in Ch. 2. Characteristic flow features are described in relation to the best known example for trailing vortices: wingtip vortices. In addition, previous research on trailing vortices around ship hulls is summarised. Chapter 3 provides a review on turbulence as a phenomenon and its modelling. This is crucial for the analysis of the vortex core flow. Physical and numerical details on the test case are presented in Ch. 4. Chapter 5 is the core of the present thesis as it provides a thorough interpretation of the numerical flow prediction. It concludes with a detailed summary and the last chapter 6 provides a global conclusion of all findings.

The appendix contains one short part, the overview of existing measurements of the present test. Chapter B provides a short presentation of major flow variables used throughout the thesis and valuable supplementary results, some are referred directly in Ch. 5 but further visualisations of the vortex flow are worth to be considered generally.

[12] These experimental observations reveal a linear relation between the circulation strength and the relative axial velocity in a certain range in the extended near field and the far field of wingtip vortices, see Sec. 2.2.3 for further details.

2. Trailing Vortices: a Review of the Characteristics

This chapter provides the theoretical background on the phenomenon trailing vortex. A general description of the flow feature "trailing vortex" marks the beginning. Second, the simplest and most investigated type is examined: wingtip vortices. The characteristics axial velocity, wandering, core turbulence, instabilities and interactions deserve special attention. As trailing vortices shed from ship hulls usually matter within the near field, this region is considered mainly.[1] Following, popular benchmarking ship test cases in manoeuvring conditions and similar bodies in inclined inflow are analysed with regard to the evolution of trailing vortices in the wake.

This chapter focuses on the detailed description of the vortex evolution and refers mostly to experimental investigations. For the detailed numerical analysis of the vortex evolution turbulence needs to be at least partially resolved to account for the complexity of the near-field vortex core flow: it is a non-uniform, anisotropic, unsteady mixing zone and so involves several scales (e.g. small ones from the separating shear layer and comparatively larger ones like vortex wandering). Additionally, the high mean flow gradients interact with turbulence production (axial velocity gradients) and diffusion (stabilising swirling flow).

The visualisation of vortex flows is an impressive approach towards its analysis. Some books provide a collection of valuable figures showing the complex nature of vortex evolution, the interested reader is referred to Van Dyke (1982, pp. 42), Green (1995, pp. xvii) and Lambourne, Bryer (1961).

2.1. What is a Trailing Vortex?

Trailing[2] "vortices occur wherever a lifting surface terminates in a fluid" (Green 1995, p. 427). They are represented by the swirling flow structure that extends far (in terms of model dimensions) downstream in the wake; their axes are approximately aligned to

[1] Persistence of trailing vortices is a significant feature but relates more to the far-field and hence is not considered in detail.

[2] "Trailing" vortex is preferred to "tip" vortex within the current thesis, because "tip" relates to wingtip and a ship hull is not a wing at the first glance, whereas "trailing" is a more universal term.

the surrounding flow.[3] Trailing vortices show almost always the following three peculiarities:

- **Fast formation:** most of the roll-up - in terms of circulation this represents the accumulation of shed vorticity inside the vortex - occurs within a short distance; short means about two to three times the chord, e.g. Green (1995, p. 447). It describes the formation of a strength and shape that sustains far downstream.
- **Persistence:** trailing vortices persist far downstream; far means many times the chord length; usually much more than 10, some report more than 1000, see e.g. Devenport, Rife et al. (1996) (about 20 spans, not chord) or Green (1995, p. 458) (more than 1000). Vortex core parameters and strength diminish very little during downstream progression compared to the extremely long extent. Jacquin, Pantano (2002) and Zeman (1995) provide further analysis of vortex persistence.
- **High gradients, small scales:** close to the vortex axis, so inside the core, the mean flow gradients are very high. Two examples illustrate that: considering a full-scale aircraft Boeing 757 in landing approach, its peak tangential velocity reaches about 100 m/s (Page, Clawson 1991). And the number of revolutions per second observed within an experiment (elliptical foil, $Re \approx 3.4 \cdot 10^5$) was found to be about 1000 (Franc, Michel 2006, p. 234). Furthermore, intense pressure reduction may lead to tip vortex cavitation (Franc, Michel 2006, pp. 223) or condensation[4] (Green 1995, p. 434). The small vortex core radius (definition with Eq. 2.2) represents the limitation of the high mean flow gradients to a small region. Its size depends mainly on the boundary layer thickness and is mostly less than 5% chord (Devenport, Rife et al. 1996).[5]

Next, common explanations for vortices are provided and its initial roll-up is described, followed by the distinction of the near and far field and the presentation of a common vortex model.

Origin and Formation Green (1995, pp. 427) summarises the three established mechanisms that explain the origin of a vortex: compensation of pressure difference, misalignment between free-shear layer and undisturbed flow, and the continuation of the wing's bound vortex. Figure 2.1 shows a sketch.

[3] Stating a universally valid definition of a fluid vortex leads to several difficult challenges, because vortices can be of very different structure, size or origin, ranging from tiny turbulent vortices in the boundary layer flow to large structures like hurricanes. Further information can be e.g. in Chong et al. (1990), Haller (2005) and Sujudi, Haimes (1995). Within the present context a universal definition would exhibit no benefit, because the presence and location of the trailing vortices is fairly obvious which is typical for trailing vortices (Green 1995, p. 8).

[4] The temperature decreases with the pressure and effectively drives condensation (Green 1995, p. 434).

[5] According to Arndt (2002, p. 159) the core radius grows with chord Reynolds number or boundary-layer thickness as revealed by several experiments. However, a proper relation has not been found.

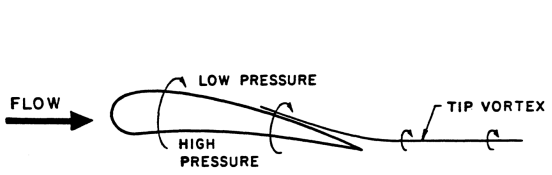

(a) Pressure field interpretation.

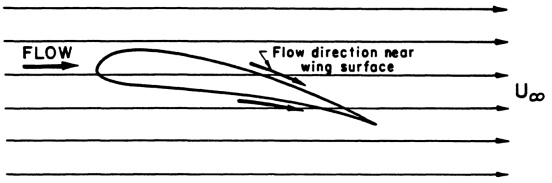

(b) Shear layer interpretation.

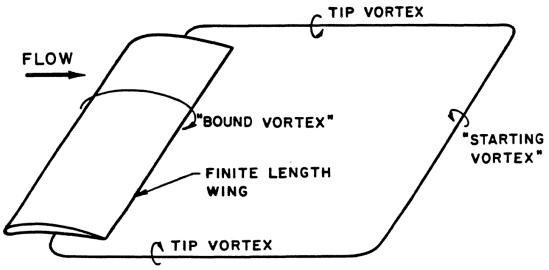

(c) Helmholtz vortex laws interpretation.

Figure 2.1.: Illustrations showing different interpretations of the origin of a trailing vortex, all figures from Green (1995, pp. 428).

(a) The pressure difference between the pressure and suction side of a wing is a measure for the lift force. At the wing tip the flow bends around the tip following the pressure gradient and thus creates a swirling flow.

(b) The wing changes the local direction of the flow. Hence, the misalignment between the shear layer at the wing tip and the undisturbed flow leads to the emergence of vorticity. Considering a wing with two tips, the vorticity creates counter-rotating tip vortices at each tip.

(c) According to the Helmholtz vortex laws "vortex tubes" cannot terminate in the fluid. Hence, the tip vortices are the link between the "bound vortex" and the "starting vortex". The bound vortex is represented by the net circulation around the wing which again is a consequence of the wing's lift (Kutta-Joukowski law). The starting vortex represents the antipode of the bound vortex which follows from Kelvin's theorem (see Green (1995, pp. 11) or Schade et al. (2013, ch. 10) for further information on the vortex laws).

Figure 2.2 presents two proper examples: rising smoke next to the runway visualises the right wingtip vortex (a). Within this context, the hazard a vortex poses to following airplanes becomes clear. A CFD result (b) shows the formation of a trailing vortex. The flow bends around the wingtip, separates and forms a swirling elongated flow structure, the vortex.[6] The separated boundary layer flow, visualised by vorticity isolines right downstream of the trailing edge, is termed free shear layer. It rolls up continuously into the vortex feeding it with vorticity or in other words circulation. Therefore, the vortex marks the centre of a spiral that usually consists of highly turbulent flow (laminar wings

[6]The initial vortex formation often takes place above the suction side upstream of the trailing edge (Chow et al. 1997a; Devenport, Rife et al. 1996).

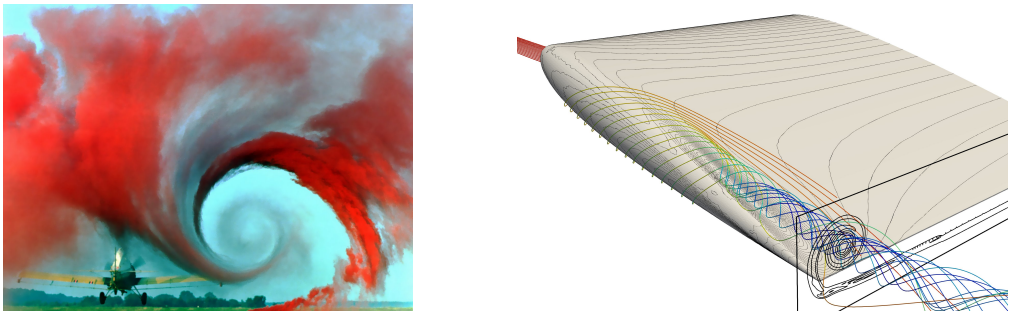

(a) Full-scale approaching aircraft, photo by NASA/ CC BY.

(b) Simulation of initial wingtip vortex evolution.

Figure 2.2.: Formation of a wingtip vortex: (a) vortex visualised with coloured smoke that represents its swirling flow, (b) RANS result (SST-CC turbulence model) of the Chow testcase (Chow et al. 1997a). Surface pressure represented by contour lines, streamlines showing vortex swirl, coloured by pressure. Just downstream of the trailing edge vorticity contour lines show the free shear layer and its roll-up into the vortex core where the vorticity concentrates.

excepted).[7] In the context of the lifting line theory, streamwise vorticity (or in other words bound circulation) is shed from the trailing edge of a wing and rolls up into the vortex. As most of the vorticity is shed near the tip (due to the high spanwise gradient of the bound circulation near the tip), its accumulation - or roll-up - into the tip vortex happens fast.

The fast swirling motion leads to a pressure reduction at the vortex centre which in turn accelerates the axial vortex flow. A velocity overshoot usually reverses downstream of the near field (within two or three chord lengths downstream of the trailing edge (Devenport, Rife et al. 1996, p. 68)), details on this effect are presented in Sec. 2.2.3.

Near and Far Field The streamwise extent of a trailing vortex can be divided roughly into two regions based on different vortex properties, the near field and the far[8] field. These properties include its structure but also different aspects like its motion.

[7] This fact is important for the flow pattern inside the core as well as its motion and will be referred to later on.

[8] Some authors propose further distinctions of the present far field (e.g. Jacquin, Fabre, Geffroy et al. (2001, p. 5)), but as the current research focuses on the near field, this is not further specified.

- **Near field:** here, the initial roll-up takes place. It extends about one chord downstream of the trailing edge.[9] The flow is not self-similar or axisymmetric, indeed it is highly three-dimensional and unsteady due to the proximity to the surface and the unsteady separation. For a review of examples see (Green 1995, p. 456) or Devenport, Rife et al. (1996, p. 68). Core turbulence is driven by the intrusion from the free-shear layer that has just separated (Chow et al. 1994). Usually it is initially high and decreases with vortex progression, because the rigid-body like swirling core flow has a stabilising effect (Jacquin, Pantano 2002, p. 160). However, the specific dissipation rate varies significantly (Devenport, Rife et al. 1996, p. 68).
  Within the near field multiple vortices may be present which merge to a single trailing vortex. This effect occurs especially on blunt tip shapes. Usually the wandering motion is assumed to be negligibly small (Chow et al. 1997a).
- **Far field:** downstream of the near field, the far field extends. It represents the extremely long persistence of trailing vortices. The far field is initiated by the transformation towards an axisymmetric core flow that happens between the trailing edge and two or three chordlengths (Devenport, Rife et al. 1996, p. 68). Edstrand et al. (2016, p. 7) found a nice explanation therefore: "The downwash from the vortex separates the trailing-edge wake from the vortex. This separation consequently diminishes the coupling and isolates the vortex, which develops into a classical helical pattern."
  Roll-up is kind of an asymptotic process, however, inside the initial far field most of it has been completed. Vortex core parameters and strength diminish very little during further downstream progression. Usually, double-paired vortices dissipate due to the Crow instability that kind of links both together resulting in highly dissipative vortex rings, see Green (1995, p. 458) or Jacquin, Pantano (2002, p. 159). For typical wings this effect relates to the far-field. But for wings with very a low aspect ratio the wingtip vortices are close together at upstream positions. This is why the possible occurrence of the Crow instability will be considered for the present test case.

Vortex Model Usually, a coherent flow pattern is assumed to be present inside the vortex core. This pattern is described first. A discussion of its actual presence follows in Sec. 2.2.2 that deals with observations of of a highly unsteady flow and the absence of a distinct instantaneous pattern.

A cylindrical coordinate system (r, θ, z) is the convenient choice for the description of the vortex velocity field: the swirling (also termed tangential or circumferential) flow around the vortex axis[10], the axial flow parallel to the vortex axis and the radial flow away from the centre (the latter is usually negligibly small Green (1995, p. 457)).

[9] The distinct value varies slightly: about one chord (Chow et al. 1997b; Jacquin, Fabre, Geffroy et al. 2001), one to two chords (Birch et al. 2003, 2004; Ramaprian, Zheng 1997))

[10] A proper representation of the vortex axis is e.g. the vorticity vector at the centre.

Several existing models describe the vortex velocity and pressure profiles, an overview can be found e.g. in Del Pino et al. (2011), Hommes et al. (2015) and Tryggeson (2007). A proper compromise between simplicity and accuracy[11] in terms of showing main core flow characteristics is provided by the ***q*-vortex** (also termed **Batchelor vortex**).[12] Here, the formulation according to Devenport, Rife et al. (1996, pp. 74) is used; the model was proposed by G. K. Batchelor (1967) as a laminar[13] solution of the Navier-Stokes equations, the tangential velocity corresponds to a Lamb-Oseen vortex (Lamb 1932).

The tangential velocity profile is

$$V_\theta(r) = \frac{\Gamma_\infty}{2\pi\, r}\left(1 - e^{-\alpha\left(\frac{r}{r_1}\right)^2}\right) \tag{2.1}$$

$$= V_{\theta 1} \underbrace{\left(1 + \frac{1}{2\alpha}\right)}_{=\frac{1}{1-e^{-\alpha}}} \frac{r_1}{r}\left(1 - e^{-\alpha\left(\frac{r}{r_1}\right)^2}\right) \tag{2.2}$$

with the radius/ distance from vortex axis r and the constant[14] $\alpha \approx 1.256$. The viscous core radius r_1 denotes the position of the peak tangential velocity $V_{\theta 1}$. The tangential velocity profile bridges smoothly the two different types of a "rotation": from rigid-body like near the centre to potential far away from the core. The vortex circulation follows to

$$\Gamma_\infty = \frac{2\pi\, r_1\, V_{\theta 1}}{1 - e^{-\alpha}} \approx 8.78\, r_1\, V_{\theta 1} \tag{2.3}$$

and its radial profile can be obtained e.g. from its definition as a ring integral of the tangential velocity profile over the circumference

$$\Gamma(r) = \oint_0^{2\pi\, r} V_\theta(r)\, ds = \Gamma_\infty\left(1 - e^{-\alpha\left(\frac{r}{r_1}\right)^2}\right). \tag{2.4}$$

The radial velocity is neglected. The axial velocity profile is

$$V_{ax}(r) = V_\infty + \Delta V_{ax}\, e^{-\alpha\left(\frac{r}{d}\right)^2} \tag{2.5}$$

[11] Several authors (Jacquin, Fabre, Geffroy et al. 2001; P. R. Spalart 1998) point out the differences between trailing vortices and the q-vortex which is easily comprehensible imaging e.g. the turbulent(!) free-shear layer that rolls up into the vortex. Del Pino et al. (2011) propose to use a vortex model from Moore, Saffman (1973) instead of the q-vortex.

[12] The Burgers vortex (Burgers 1948) consists of the same tangential velocity field, but both radial and axial components differ; the latter does not depend on the radius which generally contradicts trailing vortices (Alekseenko et al. 2007, p. 145).

[13] Models for turbulent vortices exist (Del Pino et al. 2011), but the essential features of a trailing vortex - concentration of vorticity inside core - can be clearly shown with the q-vortex.

[14] A more accurate value can be calculated e.g. by solving the above equation at $r = r_1$, so $\alpha \approx 1.256431209$.

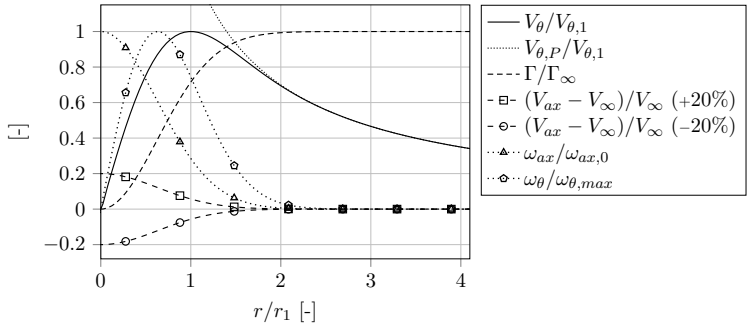

Figure 2.3.: Radial profiles of a q-vortex scaled to individual extrema. $V_{\theta,P}$ represents the potential part of the q-vortex. After about twice the core radius the vortex visually coincides with its potential part. An exemplary axial velocity overshoot/ deficit of 20% is shown, its radial scale is set to the core radius $d = r_1$ (see text). The axial and tangential component of the vorticity is ω_{ax} and ω_θ respectively.

with the free stream velocity V_∞ and its difference[15] to the value at the vortex centre $\Delta V_{ax} = V_{ax,0} - V_\infty$, d is the radial scale of the axial velocity profile.

The vorticity profile follows from the formulation of the curl in cylindrical coordinates (see e.g. Merziger et al. (2007, p. 145)), the radial component is zero, the axial and tangential ones are

$$\omega_{ax}(r) = \frac{1}{r}\frac{\partial\,(r\,V_\theta)}{\partial r} = 2\alpha\,\frac{V_{\theta 1}}{r_1}\,(1+\frac{1}{2\alpha})\,e^{-\alpha\left(\frac{r}{r_1}\right)^2} \tag{2.6}$$

$$\omega_\theta(r) = -\frac{\partial\,V_{ax}}{\partial r} = 2\alpha\,\Delta V_{ax}\,\frac{r}{d^2}\,e^{-\alpha\left(\frac{r}{d}\right)^2} \tag{2.7}$$

Its tangential component $\omega_\theta(r)$ maximises at about $0.631\,d$ which represents the inflection point of the axial velocity. The composition of the vorticity magnitude from the axial and tangential component that differ in their extreme points indicates that for a real vortex the spatial scatter of the vorticity maximum may surpass the one of the swirling flow minimum. This observation becomes important in the context of the evaluation of the FSV wandering motion.[16]

Figure 2.3 depicts the profiles as a function of the normalised radius[17]. It is obvious that the flow gradients inside the core $r \leq r_1$ are very high and negligible beyond twice the core radius $r > 2r_1$ where the q-vortex resembles very much its potential part. According

[15] For a velocity overshoot (deficit) the axial velocity incrases (decreases).

[16] The wandering amplitude represented by the vorticity centre exceed the one predicted by the swirling flow centre, see e.g. Fig. 5.15.

[17] For simplicity, the assumption $r_1 = d$ is introduced like in Edstrand et al. (2016) and Jacquin, Pantano (2002). However, e.g. for Devenport's results, d is about 40% larger than r_1.

to Stokes' theorem, circulation is the integral of the vorticity component normal to the surface over the surface S:

$$\Gamma = \int_S \boldsymbol{\omega} \cdot d\boldsymbol{S}. \tag{2.8}$$

This is represented by the integral evolution of the circulation curve. To provide a quantification of this radial behaviour: half the circulation is contained within about 3/4 of the core radius, 90% within 1.35 core radius and more than 99% at twice core radius.

The vortex core radius gradually separates viscous and potential flow. There exist a further radial fragmentation to classify the flow characteristics more precisely (see e.g. Bosschers (2018, p. 9) or Phillips (1981, p. 455)). However, this is linked to a developed trailing vortex in the far field and of little benefit within the current context as the flow of a near-field vortex is quite inhomogeneous.

The swirl parameter (or number) relates the swirling flow to the axial flow

$$q \approx 1.56 \frac{V_{\theta 1}}{|\Delta V_{ax}|}, \tag{2.9}$$

see Jacquin, Pantano (2002, p. 162) or Green (1995, p. 338). The suppression of disturbances in terms of velocity fluctuations correlates with q. A critical value was found to be $q^* = 1.5$ above which the vortex core flow tends to become laminar and small-scale turbulence is going to be suppressed during progression; "strong rotation stabilizes all the perturbations" (Jacquin, Fabre, Sipp et al. 2005, p. 408). However, this criterion is usually applied to separated axisymmetric wingtip vortices in the far field.

The following remarks highlight the link between a manoeuvring ship hull and a wing in terms of trailing vortices. Trailing vortices evolve downstream of a streamlined body generating lift. The most prominent example is a wing and a wingtip vortex: This is obviously present for any type of wings like aircraft wings, propeller wings and foils or fins used to generate lift. Considering a ship hull in manoeuvring conditions, e.g. steady drift, the hull is a streamlined body generating lift, and the trailing vortices are basically wingtip vortices. The peculiarity here is the shape of the hull (e.g. bulbous bow or transom stern), possible appendages and the very small aspect ratio (draught to length). Besides, the region of interest is close to the hull, so interactions with following vehicles play a negligible role.

2.2. Wingtip Vortices: Characteristics

Vortices shed from wingtips are the most convenient example of trailing vortices, because the wing usually has a streamlined shape and the vortex develops with very little disturbances. In addition, wingtip vortices as test cases have been extensively studied and this large data basis permits the analysis of vortex effects for various similar conditions.

This sections aims to provide detailed explanations of vortex characteristics or effects. The basis are many intensive experimental investigations, numerical considerations are treated shortly if certain effects require distinct modelling. The section starts with the transverse motion of vortices and continues with the flow structure inside the core. Finally, the axial flow, interactions and instabilities are discussed.

2.2.1. Wandering

Wandering (also called meandering) describes the coherent low-frequency side-to-side movement of a vortex (Devenport, Rife et al. 1996, p. 67):

- coherent relates to the well ordered evolution of the displacement and
- the frequency is very small compared to turbulent motions.

A necessary condition for the existence of wandering according to the above definition is the presence of a coherent or distinct pattern in the vortex core flow whose temporal variation in space is considered.[18] A sufficient condition implies also the excitation of this motion, possible mechanisms are discussed below and are usually present in technical flows. Or in other words, it is highly probable that a vortex wanders confirmed by many guiding wind-tunnel experiments. And this occurrence was the main motivation for previous investigations.[19] Figure 2.4 visualises its definition: the current displacement of the vortex from its mean position.

Two aspects related to wandering are treated within this study: wandering is regarded as a property of a trailing vortex, so its characteristics and possible mechanisms are analysed. And mean flow measurements need to be corrected for the individual wandering motion to reveal important flow details which would be smeared otherwise. Both aspects rely on a detailed description on the phenomenon: first, the wandering motion of wingtip vortices will be described including consequences and influencing factors. Second, possible explanations for the origin will be presented.

[18] In contrast, a fully turbulent core flow also exhibits variations of a centre, but these variations are more chaotic and not well ordered.

[19] The presence of wandering in full scale flight conditions is not certain (e.g. Chow et al. 1997a): disturbances are smaller - the free-stream turbulence is very small compared to wind-tunnel tests - but other mechanisms are still present.

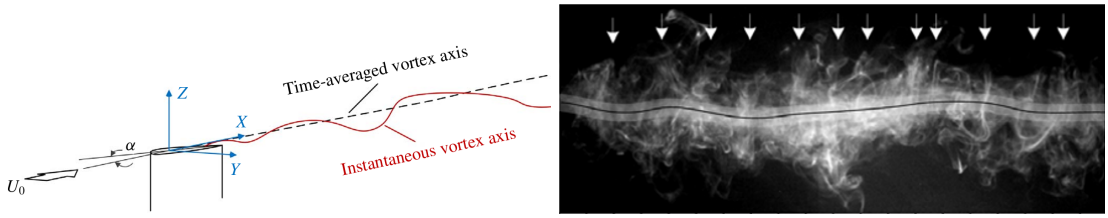

(a) Sketch with wingtip and mean vortex axis. The deviation of the instantaneous axis from its time-averaged location is termed as wandering motion.

(b) Laser-induced fluorescence image: black line - vortex axis, surrounding grey region - uncertainty bounds, white arrows - location of secondary azimuthal structures.

Figure 2.4.: Exemplary alignment of the instantaneous axis of a wingtip vortex, both from Bailey et al. (2018). Wandering is the current displacement of the vortex from its mean axis.

Pioneering work on this topic has been conducted by Bailey et al. (2018), Corsiglia et al. (1973), Devenport, Rife et al. (1996), Edstrand et al. (2016), Heyes et al. (2004) and Jacquin, Fabre, Geffroy et al. (2001). After the discovery in the 1970s (see e. g. Corsiglia et al.), Devenport, Rife et al. (1996) conducted a guiding wind-tunnel study on wandering which provided much information on wandering behaviour; later research focuses on the mechanisms and often refers to Devenport and colleagues. They remarked that the wandering amplitude increases monotonically (approximately linear) with downstream distance (confirmed e.g. by Edstrand et al. (2016) and Heyes et al. (2004)) and decreases with a larger angle of attack. The latter finding can be generalized: The wandering amplitude decreases linearly with the vortex strength, as other studies led to similar findings (Heyes et al. 2004). An increase in free-stream turbulence leads to an increase in the wandering amplitude (e.g. Bailey et al. 2018). Previous experiments show a small wandering amplitude compared to the dimensions of the wing, e.g. below 30% of the core radius and below 1% chord in Devenport, Rife et al. (1996) or about 1% chord in Heyes et al. (2004). Chow et al. (1997a) investigated the near field and a wing with a high loading, so a strong vortex, which supports their observation that wandering amplitudes were found to be small and not worth to be corrected. Usually, wandering is investigated and corrected in the far field. Gursul (2005) provides an exception as wandering is analysed for a leading-edge vortex over a delta wing: he highlights the strong impact even in the near field.

Most studies on wandering assume or report (approximately) Gaussian PDFs for the wandering motion (Devenport, Rife et al. 1996; Edstrand et al. 2016; Heyes et al. 2004). However, this behaviour is not certain (P. R. Spalart 1998), wandering in the form of a sine wave would result in an M-shaped PDF.

Using a fixed grid for the temporal analysis of the vortex flow (e.g. hot wire, PIV or FVM in CFD), wandering leads to spatial averaging (Green 1995, p. 445) of the high flow

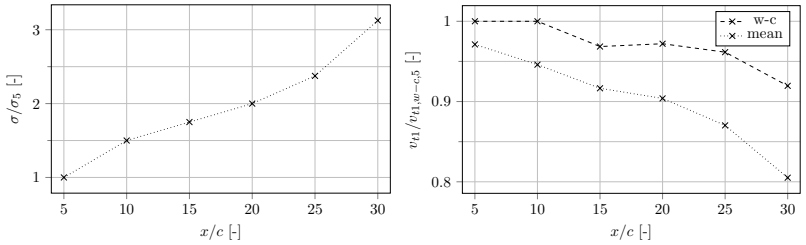

(a) Averaged in-plane wandering amplitude: monotonic increase downstream.

(b) Peak tangential velocity: the mean vortex shows stronger decay than the wandering-corrected (w-c) one.

Figure 2.5.: Wandering amplitude and its effect onto the peak tangential velocity, between five and 30 times the chordlength c downstream of the trailing edge, both reproduced from Devenport, Rife et al. (1996). The curves are normalized with the value at $x/c = 5$.

gradients inside the vortex core.[20] Any mean vortex profile would degenerate towards a Burgers vortex if the wandering amplitude was sufficiently high (Devenport, Rife et al. 1996). This finding highlights the need for wandering-corrected vortex core flow in the context of a detailed vortex analysis, e.g. to reveal its real profile. Figure 2.5 shows the influence of wandering on the vortex flow: the uncorrected mean flow suggests a vortex decay which is much less pronounced for the wandering-corrected flow and originates mostly from the downstream increase of the wandering amplitude. Here, wandering correction was realised based on the assumption of a Gaussian PDF.

Although the consideration of the motion is of utmost importance, they concluded that the influence of wandering on the vortex development is probably negligible because of the difference to turbulent motions in terms of frequency. Moreover, the influence on the mean flow quantities is limited to the vicinity of the core (about three times the core radius, similar observations were made within other studies, e.g. by Baker et al. (1974)), so a wandering correction outside of this region becomes redundant. The wandering motion was found to follow a preferred direction, so it was anisotropic (Devenport, Rife et al. 1996, p. 80). However, the degree of anisotropy was small as the RMS of the major and minor axis varied mostly by about 10% only (compare $\sigma_{y/z}$ in Devenport's table 2). Spectral analysis revealed the broadband spectrum of the wandering motion in low-frequency regimes compared to turbulence.

Correction Considering measurements with fixed probes (hot-wire anemometry or Laser-Doppler Anemometry, LDA) the instantaneous centre of the vortex cannot be tracked in time. Therefore Devenport, Rife et al. (1996) developed a statistical correction al-

[20]The circulation is insensitive of the in-plane wandering (Devenport, Rife et al. 1996, p. 75).

gorithm to deduce the real vortex velocity profiles that are not smeared. It is based on the assumption of a distinct wandering behaviour and not further presented here.

Heyes et al. (2004) were the first to conduct a straight correction for wandering from instantaneous PIV snapshots: they merged all instantaneous velocity fields with respect to their individual swirling flow centre. However, this approach is only a planar-like wandering-correction because a possible change of the vortex axis due to wandering is not considered. For the far field this is probably acceptable. Heyes and colleagues corrected also Reynolds-stress components for the wandering motion: The uncorrected fields show characteristic patterns (see 2.2.2) and the corrected ones do not. Instead, the vortex core is actually laminar. Devenport and colleagues made similar observations. The link between turbulence and wandering will be examined in the next subsection.

Mechanisms Next, the question of the origin of the wandering motion will be treated. Summarising previous investigations Jacquin, Fabre, Sipp et al. (2005) provides a valuable overview and distinguished six possible mechanisms driving wandering. They suppose some kind of vortex instability and note that different types may superimpose.

In accordance with that, Edstrand et al. (2016) analysed experimental results and concluded that some flow instability may be the reason for the observed wandering motion. This finding is based on two approaches: first, the authors revealed the most energetic structures of the vortex core flow using Proper Orthogonal Decomposition (POD). Second, they detected the primary stability mode of a matched vortex for which a linear stability analysis revealed marginal stability. Comparing the results of both approaches shows that the first POD mode and the primary instability mode are very similar. Therefore, Edstrand and colleagues supposed that wandering may be driven by an instability.

Until now, the mechanisms driving the wandering motion are not fully understood and this topic is content of present and future research (e.g. Edstrand et al. (2016) and Qiu et al. (2020) or for a review Bailey et al. (2018)). The present thesis will contribute another example with focus on the near field.

Finally and in relation to the next section on turbulence, it is important to state that two aspects of turbulence are treated: turbulence in the wake surrounding the vortex and turbulence in the vicinity of the vortex axis. The former may induce wandering, the latter may result at least partly from the (wandering) motion of a vortex: the temporal velocity change on a fixed grid can be interpreted as Reynolds stresses (Chow et al. 1997a, p. 1565).

2.2.2. Core Turbulence

The discussion on the turbulent content of the vortex core flow is started with an illustrating example: is there a coherent structure, in terms of e.g. a q-vortex like velocity profile? If yes, it seems quite probable that the coherent structure moves, because several different perturbation types exist: the vortex is the centre of the highly turbulent shear-layer rolling-up, and further perturbations (wing vibrations, inflow variations) or instabilities may contribute. Being time-averaged the unsteady nature may be interpreted as turbulence. If there is no coherent structure, a vortex relates to the region of swirling flow with high vorticity. A wandering motion cannot be defined as it relies on the motion of a flow pattern that changes little in time and space - or in other words, is coherent. Temporal changes of the flow would represent turbulence and be rather chaotic.

The question whether the flow inside the vortex core is laminar or turbulent considers several aspects treated in the following. First, both a qualitative and quantitative definition of turbulence are presented, second the origin of possible turbulence is discussed, third the actual state of the core flow and finally its characteristics in terms of a quantitative view of turbulence (Reynolds stresses) are analysed.

Definition Turbulence as a phenomenon is defined in detail in Sec. 3.1. For the current question one feature of a turbulent flow is important: its random nature (Pope 2000, p. 34). Turbulent velocity fields can be distinguished by the absence of a regular spatial or temporal pattern in the velocity field. The flow reacts highly sensitive to small perturbations and seems to be chaotic.

In terms of a quantifying measure of turbulence, it is common practice to use the Reynolds decomposition (refer to section 3.2.1 for more details) as an approach to define secondary statistical moments that describe turbulent velocity fluctuations u_i': the Reynolds stress tensor

$$\overline{u_i' u_j'} \tag{2.10}$$

and half its trace, the Turbulent Kinetic Energy (TKE, see Eq. 3.10). These velocity fluctuations are defined as the deviation from a mean value which in turn represents the time average. Hence all velocity fluctuations are taken as turbulence.[21] Or in other words, the averaging time presets whether coherent velocity variations are taken as turbulence. An example would be the Karman vortex street in the wake of a cylinder: Applying long-time averaging the coherent vortices would be seen as turbulence.

[21] The separation of the flow field into a mean and a fluctuating part can also be used for experimental data or turbulence-resolving simulations.

Origin: where does it come from? In the specific case of a trailing vortex, the separating shear layer - that is highly turbulent - rolls up into the vortex itself. This is a continuous source of turbulent fluctuations entering the vortex core. Furthermore, high axial mean-flow gradients produce turbulence. Chow et al. (1997a, p. 1567) observed this to be the dominant source for turbulence in the near field. Mostly the axial gradients limit themselves as the produced turbulence acts mainly on the reduction of the velocity overshoot (Devenport, Rife et al. 1996, p. 97, 99). In contrast the inherent swirling motion imposes a trend towards re-laminarisation as viscous forces due to the solid-body rotation are comparatively high. This effect has been extensively discussed, see e.g. Green (1995, p. 458) or Jacquin, Pantano (2002, p. 160). Probably the relaminarisation dominates with increasing progression as both mean-flow axial gradients and the turbulence level of the free-shear layer decrease.

Laminar or Turbulent? On the one hand, the turbulent surrounding and high axial flow gradients in the vortex core generate turbulence. On the other hand the circumferential flow is similar to a rigid-body rotation and exhibits a huge stability suppressing the propagation of perturbations - an effect called relaminarisation. The distinct degree of turbulence or its absence depends on the interaction of these mechanisms. The near field tends to be turbulent because the turbulence intensity inside the free shear layer is higher at upstream positions. Further, possible high deviations of the axial flow from the inflow diffuse further downstream. Chow et al. (1997a) reported this behaviour up to about a chord length downstream of the trailing edge. However, the far field tends to be laminar (Jacquin, Fabre, Geffroy et al. 2001, p. 15). Devenport, Rife et al. (1996) observed a laminar core between five and 30 times the chord downstream. They could explain the high Reynolds stresses with the "inactive motion" [p. 67] excited by the surrounding shear-layer turbulence. Both the laminar flow and the wandering motion leading to high Reynolds stresses were confirmed by Heyes et al. (2004) for a different wing between one and 23 times chord downstream. Further findings were reported by Bandyopadhyay et al. (1991) and Miloud et al. (2020).

Stress-Strain Lag The Reynolds-shear stress in the plane normal to the vortex axis shows a typical pattern around the vortex core that is exemplary depicted in Fig. 2.6. The stress contours are rotated by 45° compared to the corresponding mean strain rates, or in other words: the stress lags the strain. Considering turbulence modelling, this effect cannot be modelled with isotropic eddy-viscosity RANS models.

This pattern is observed for many different kinds of trailing vortices, e.g. for a near field tip vortex Chow et al. (1997a) and a trailing vortex next to a ship hull Visonneau, Guilmineau et al. (2020a). The interesting point is that both a highly anisotropic and inhomogeneous core flow and also an ideal q-vortex result in a similar stress pattern. Jacquin, Fabre, Geffroy et al. (2001) and Zeman (1995) provide more details, see also

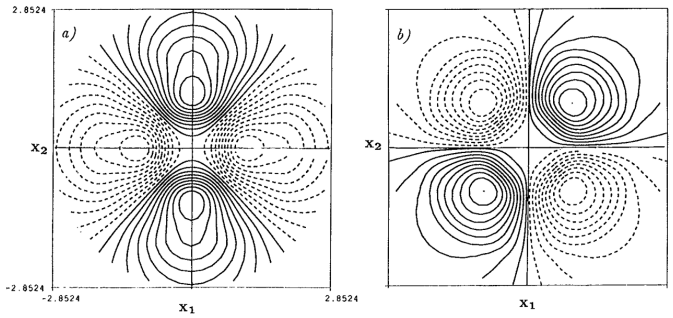

Figure 2.6.: Pattern of the in-plane strain rate $\left(U_{y,z} + U_{z,y}\right)$ (a/ left) and the respective Reynolds-shear stress $\overline{u'_y u'_z}$ (b/ right) downstream of a wing (Zeman 1995, p. 141). Negative contour lines are dashed. The common phrase four-leaf clover pattern relates to this stress pattern.

Sec. B.7. This highlights the potential impact of a wandering motion on the time-averaged velocity fluctuations. Even in the presence of turbulence the wandering motion of a vortex that in turn deviates from the q-vortex may produce the mentioned pattern.

2.2.3. Axial Velocity

The vortex axial velocity is the projection of the velocity vector onto the vortex axis at the position of the vortex centre. A possible representation of the vortex axis is the vorticity vector. Depending on some key flow features the axial velocity can be smaller than the inflow one (deficit) - termed wake-like - or larger (excess) - termed jet-like. The driving mechanisms, the key flow features and various examples will be provided in the following.

The initial formation of the vortex is driven by two mechanisms: the roll-up of the separated boundary layer flow and the development of the characteristic swirling flow. Both have an influence on the axial velocity: the free shear layer has a momentum deficit and therewith incorporates a deceleration of the flow; the tangential velocity leads to a low pressure at the vortex centre (sometimes causing visible effects like condensation or cavitation) and so induces an axial pressure gradient that leads to an acceleration of the flow (G. Batchelor 1964; Moore, Saffman 1973).

Shekarriz et al. (1993) explain this further and provide several exemplary studies. The swirling flow induces an increase or decrease of the axial velocity depending on the axial gradient of the vortex flow: during the initial roll-up the tangential velocity grows along the vortex axis (negative axial pressure gradient and increase of axial velocity), within decay the tangential velocity reduces (decrease). The individual formation of a jet-like or wake-like axial velocity depends on the interaction of both mechanisms (momentum deficit/ swirling flow) which is driven by individual conditions. According to G. Batchelor (1964) the Bernoulli equation can be used to qualify this effect. This was extensively

discussed by other authors (Anderson, Lawton 2001; P. R. Spalart 1998). However, the distinct determination of the viscous loss is hard to quantify.

Anderson, Lawton (2001) found a linear relation between the relative axial velocity and the circulation parameter[22]

$$U_x/U_\infty \propto \frac{\Gamma}{U_\infty\, b} \tag{2.11}$$

for own experiments and five benchmarking cases. The tip shape deserves special attention (see also T. Lee, J. Pereira (2010)). Anderson and Lawton stated that "the cause of the velocity excess is streamwise directed downwash" (p. 1). This means that a portion of the induced velocities - originating from the vortex filaments wrapped around the vortex centre on a helix - is aligned with the vortex axis. Due to the Biot-Savart law, the relation between the vortex circulation and the axial velocity becomes linear. Considering the experiments this effect seems to be dominant and no nonlinear influence is present, i.e. a varying helix pitch due to vortex stretching. This correlation will be analysed within the near field in the present study.

2.2.4. Interactions and Instabilities

Within the present context interaction relates to evolved trailing vortices, e.g. co- or counterrotating trailing vortices. As their interaction may induce long-wave instabilities, both interactions and instabilities are summarised within one section. Instability relates to growing amplitudes of the vortex motion (e.g. the Crow instability) or the occurrence of sudden chaotic behaviour (e.g. vortex breakdown) that originate from little disturbances.

Short-wave instabilities often refer to the behaviour of a single trailing vortex whereas long-wave instabilities refer to the interaction of a vortex pair, also termed cooperative instabilities because of the mutual action.Refer to Jacquin, Fabre, Sipp et al. (2005) for a valuable review of vortex instability. A distinction between wandering, instabilities and turbulence may be made by the frequency range covered: Devenport, Zsoldos et al. (1997, p. 90) state that "wandering dominates the low-frequency end of velocity spectra in the core, instabilities may be a factor at mid frequencies", turbulence describes the apparently random occurrence of fluctuation within the flow and is ofter attributed to the intertial sub-range.

[22] Here, Γ is the vortex circulation, b the full wing span, U_x the axial velocity and U_∞ the inflow speed. Considering experiments with half-wings mounted inside a wall, b is twice the wing's semispan. Anderson and Lawton further present a modification of b to account for the wing's tip shape.

Interaction Devenport, Vogel et al. (1999) and Devenport, Zsoldos et al. (1997) published extensive results on the interaction of co- and counter-rotating wingtip vortices. The experiments follow on the guiding one in 1996. The counter-rotating vortices are found to experience an increase of turbulence in the far field after they had relaminarised. This is in contrast to their single evolution that tends towards a laminar condition and is entirely driven by their interaction. The interaction is assumed to stimulate transition inside the cores that manifests in short-wave instabilities. In relation to vortex wandering it is important to highlight that they found it to be one consequence of the Crow instability.

The co-rotating wingtip vortices studied spiral around each other and merge in the far field. Within the merging region they initially develop a single turbulence structure which initially links both cores with an 'S'-like pattern. Turbulence becomes highly anisotropic but the merged vortex undergoes relaminarisation also.

These effects can be summarised with P. R. Spalart (1998, p. 130): "After the initial roll-up, vortices interact in three essential ways: They induce each other's basic nearly 2D motion; they can support 3D instabilities; and they can merge, particularly if corotating." The 2D motion relates to the vortex in-plane displacement, i.e. wandering and 3D instabilities refer e.g. to the Crow instability. Various further investigations exist on this topic, see e.g. Chen et al. (2018) and Misaka et al. (2012). Valuable visualisations of the Crow instability can be found in De Visscher et al. (2013) and Misaka et al. (2012).

Both co- and counter-rotating vortices are present for the double-body model test case analysed within the following investigations. Possible interactions and instabilities will be considered.

Vortex Breakdown Vortex breakdown[23] is a sudden event of slender vortices that destroys the coherent flow structure. Sudden refers to the short streamwise distance of its formation, Saffman (1992, p. 285) e.g. refers to the order of the core radius, and slender represents a vortex with a small core radius compared to axial changes, see Saffman (1992, p. 285) or Althaus et al. (1995, p. 377). Extensive reviews on this effect have been presented by Althaus et al. (1995), Lambourne, Bryer (1961) and Lucca-Negro, O'Doherty (2001).

[23] Vortex bursting is a similar phenomenon but relates to the far field, see e.g. Jacquin, Fabre, Sipp et al. (2005, p. 410).

Green (1995, p. 433) adds up that the vortex flow transform "from high tangential velocity, small core radius flow, to highly turbulent, low tangential velocity, reversed axial velocity, large core radius flow". The central backflow at the breakdown and the following fluid deceleration are further features. At the vortex centre, both vorticity and TKE peak in contrast to pressure and axial velocity that drop (Lucca-Negro, O'Doherty 2001; Morton 2009; Son et al. 2015). Helicity drops too (Lucca-Negro, O'Doherty 2001, p. 462). Lambourne, Bryer (1961) show fotographs of experiments revealing interesting details on the structure of the breakdown.

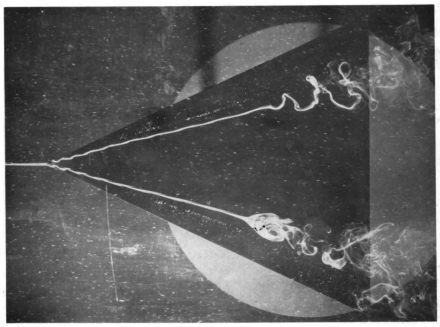

(a) Delta wing at large incidence showing both spiral-type (top) and bubble-type (bottom) vortex breakdown visualised with dye (Lambourne, Bryer 1961, p. 23).

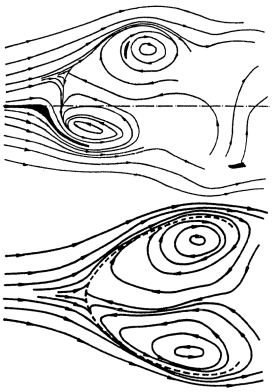

(b) Corresponding similar schematic visualisation of streamlines. Both Figures from Brücker (1993) and Brücker, Althaus (1992)

Figure 2.7.: Vortex breakdown as photograph from experiment and corresponding similar 2D-view in longitudinal plane.

A visual impression of the phenomenon is given by Fig. 2.7. Two main types of breakdown[24] disrupt the leading-edge vortex as the dye filaments represent the strong deformation of the streamlines. The detailed structure of both breakdown types are shown right. The in-plane streamlines show a similar pattern for both types: The swirling flow splits up and a backflow with an internal stagnation point is formed inside the vortex core, the outer streamlines widen and the time-averaged vortex decreases in strength. The difference between both types is that the stagnation point of the spiral one rotates around the mean centreline whereas it remains on the mean vortex axis for the bubble type. The latter consists of a toroidal-like vortex that creates backflow at the centre. This leads to a post-breakdown wake with greater mixing compared to the spiral type.

[24]Further variants of this major classification can be deduced, see e.g. Lucca-Negro, O'Doherty (2001, p. 435).

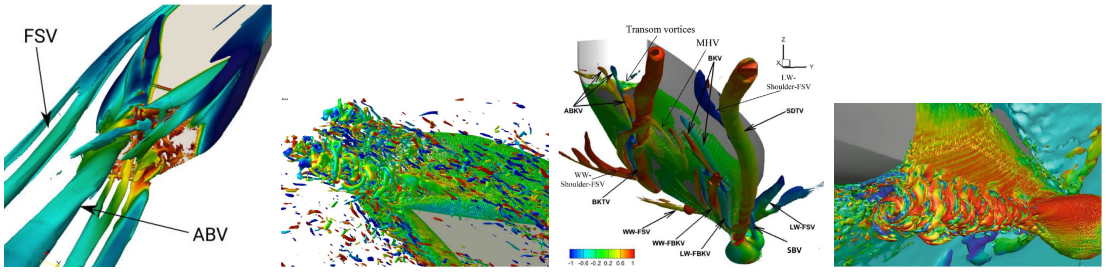

(a) JBC: major vortices FSV and ABV at 8° drift (Shevchuk et al. 2020).

(b) JBC: separation at straight ahead (Queutey et al. 2016).

(c) DTMB5415: major vortices (Bhushan, Yoon, Stern et al. 2019).

(d) DTMB5415: sonar dome separation (Visonneau, Guilmineau et al. 2020a).

Figure 2.8.: Vortex system around popular ship test cases in steady drift conditions and a specific region of interest.

2.3. Ship Test Cases

Manoeuvring ships generate trailing vortices usually at the separation on blunt edges as a consequence from the lift. These vortices resemble wingtip vortices and are almost always studied within the near-field. As the current thesis relates to the maritime context, the popular test cases are described separately. The focus is put on the vortex effects and both their experimental detection and numerical prediction. Similarities between different ship models are highlighted at the end of the present section.

Monohull test cases cover the full block crude and oil carriers KVLCC2 and Japan Bulk Carrier (JBC) and the slender surface combatant DTMB (David Taylor Model Basin) 5415. Figure 2.8 provides an overview of the vortex system for the two latter test cases: JBC and DTMB5415. Details are presented in the following.

2.3.1. KVLCC2

Geometry Variants Two variants of the KRISO Very Large Crude Carrier (KVLCC*) model - no full-scale version exists - were designed by the Korea Research Institute of Ships and Ocean Engineering (KRISO) as "a modern [ca. 1997] 300 K tanker ship with bulb bow and stern" (SIMMAN 2008). Both variants differ in the stern shape: KVLCC1 has barge type stern frame-lines with a fine stern end bulb, i.e. more V-shaped frame-lines. And KVLCC2 tends towards U-shaped stern frame-lines. Besides, KVLCC2-M denotes the addition of a fairing around the propeller shaft and the extension of the stern to avoid an immersed transom. The reason is to avoid flow separations at sharp edges and hence reduce the complexity of the stern flow. The hull form differs slightly.

Table 2.1.: Dimensions of KVLCC2 full-scale and model used herein. The model scale values are rounded to millimeters. There is a typo for the values marked with * in Abdel-Maksoud et al. (2015). Several other models with a different scale have been investigated.

Main particulars			Ship	Model
Length over all	L_{oa}	[m]	333.6	1.600
Length between perpendiculars	L_{pp}	[m]	320.0	1.535
Moulded breadth	B	[m]	58.0	*0.278
Moulded draught	T	[m]	20.8	*0.100
Modified draught	D	[m]	21.5	0.103
Block coefficient	$C_B(T)$	[-]	0.810	0.810
Scale	λ	[-]	1.0	208.5

Herein, the variant KVLCC2 with a fairing around the shaft is used in bare-hull configuration (no appendages, no rudder, no bilge keels). In order to obtain a smoother shape at the intersection of the waterline, i.e. symmetry plane, and the forward perpendicular for the double-body model, the draught is increased by 0.68m compared to the design condition (Abdel-Maksoud et al. 2015, p. 3). Table 2.1 shows the dimensions of the KVLCC2 hull, for full-scale and for the model used within this research. The body plan together with the vortices FSV and ABV is shown in Fig. 5.5.

CFD Workshops The KVLCC2 hull is subject of study within several CFD Workshops on Ship Hydrodynamics: the focus is set on the manoeuvring behaviour of the hull and hence on the forces in drift or sway conditions. Further aspects like shallow water and the wake field at the propeller plane are studied. This also concerns the performance of hybrid RANS-LES models (Larsson, Stern, Visonneau 2014, p. 316). The core flow of the trailing vortices is not analysed.

Two SIMMAN workshops (Simonsen, Stern 2014; Stern, Agdrup 2008) were held with a focus on forces and trajectories during manoeuvring motions (PMM, DMT, FREE) for both deep and shallow water. During the Gothenburg workshops Gothenburg 2000 (Larsson, Stern, Bertram 2003) and 2010 (Larsson, Stern, Visonneau 2014) the wake field around propeller plane for straight ahead flow was investigated. In addition, the presented experiments by S.-J. Lee et al. (2003) are treated below. The KVLCC2 model is not part of the Tokyo 2015 and the Wageningen 2021 workshops.

Previous Experiments Table A.1 gives an overview over existing experiments. The first row shows the experiments conducted relating to this research for an easy comparison. The first (wind-tunnel) experiments by S.-J. Lee et al. (2003) revealed the wake field and the wall streamlines for straight ahead inflow. Kume et al. (2006) conducted measurements inside a towing-tank of the forces, the hull pressure and the wake field for

different drift angles. The FSV was clearly visible in the wake flow but no further analysis on the trailing vortices was conducted. Preliminary to the experiments used within the present thesis, Abdel-Maksoud et al. (2015) conducted tests with the same model in the same facility at little higher inflow speed.[25] The oil film visualises the separation and smoke indicates the vortex swirling pattern. Stereoscopic PIV measurements are conducted in planes normal to the inflow and the time-averaged centre flow for the FSV, ABV and ASV is analysed. A distinct velocity overshoot with a maximum of 20% occurs. Secondary vortical structures surrounding the FSV are suspected to accelerate the axial flow similar to a leading-edge vortex of a delta wing. All in all, the only previous experiments on the vortex system revealed the need for a thorough investigation with a higher spatial and temporal resolution which was realised at the wind tunnel of TUHH in summer 2020. The data was not finally processed at the time of writing and may be part of a future comparison with the presented numerical results.

Previous Simulations Previous studies contributing essential findings on the vortex core flow are presented in chronological order.[26] Fureby et al. (2016) provides results for RANS, DES and LES approaches for straight-ahead as well as 12 and 30° drift. Major vortices were found to be surrounded or even replaced by a "cloud of coherent vortices" (p. 15). Some exhibit helical instabilities. The time-averaged velocity and the axial normal Reynolds-stress are similar for the different turbulence models, but the turbulence resolving approaches are closer to the experimental data from Kume et al. (2006) for the wake flow. A general conclusion states the accuracy of RANS for global flow predictions and its limitation concerning higher statistical moments of the flow. However, turbulence resolving approaches predict the side force and the moment with higher accuracy. A possible explanation may be the similarity to delta wings where the distinct leading-edge vortex creates 'vortex lift'. Abdel-Maksoud et al. (2015) published the results of a cooperative NATO research project with several CFD submissions including RANS (SST, SST-CC, EARSM), DES and LES approaches. A main conclusion was that different turbulence models promote advantages for different flow aspects and none is superior in all aspects. The axial velocity surplus was predicted only by a hybrid RANS-LES approach on a structured mesh. Larsson, Stern, Visonneau (2014) provides a valuable overview of various approaches in relation with the Gothenburg 2010 workshop on ship hydrodynamics. It targets the performance and applicability of hybrid RANS-LES approaches with a thorough analysis of the errors. Xing et al. (2012) used RANS and DES for 0, 12 and 30° inflow angle. A vortex breakdown of FSV was observed shortly after initial separation indicated by (modelled) TKE and pressure increase as well as velocity and vorticity decrease in relation to Gursul (2005). An interesting point is the presentation of the TKE budget for the FSV: turbulent production and viscous diffusion are the driving counteracting terms. Stern, Ismail et al. (2008) considered straight-ahead inflow and 12 and 30° drift angle. The focus was set on the numerical performance of different

[25] Due to slight vibrations the inflow was reduced herein.

[26] The author published a preliminary study on this case (Feder et al. 2019) that was focused on the time-averaged vortex core flow.

convection schemes. The analysis of the TKE budget revealed the aspects mentioned also by Xing et al. (2012). They highlighted the link between the ship hull and a delta wing, e.g. the similarity between the FSV and a leading-edge vortex.

All in all, the complexity of the unsteady vortex structures has been revealed, a distinct jet-like core flow and details on the accumulation of TKE inside the core also. The following points have not been considered but are part of the present investigation: a possible coherent wandering motion of the FSV especially and the corresponding correction to reveal the unsmoothed core flow. Furthermore, vortex core parameters and a variation of the inflow speed have not been considered. A distinction of different centre representations and the thorough analysis of the centre flow (e.g. vortex angle, helicity, turbulent stresses) are also a novelty of the present thesis.

Further studies deal with inclined inflow without a distinct consideration of the vortex core flow, see e.g. the following latest publications Abbas, Kornev (2016b), Jin et al. (2016), Toxopeus, Simonsen et al. (2013) and X. Yang et al. (2019). There the focus is laid on manoeuvring forces, influence of confined walls or the wake flow quality. Abbas, Kornev (2016a) used RANS, DES and LES approaches to predict the non-uniformity and unsteadiness of the wake flow and the action onto the propeller loadings. The general vortex system for straight-ahead and for 12° drift was analysed. The complex turbulent mixing wake was described.

Futher publications on the KVLCC2 hull consider straight-ahead conditions only and deal generally with stern flow separation or turbulence resolving methods, i.e. in terms of propeller wake quality prediction: e.g. Abbas, Kornev et al. (2015), Kornev, Shevchuk et al. (2019) and F. S. Pereira et al. (2019).

2.3.2. Other Hulls and Similar Bodies

JBC As there is a flow separation at straight-ahead inflow, see Fig. 2.8, most investigations focus on details of the wake flow around the propeller plane, e.g. Kornev, Abbas (2018), Kornev, Shevchuk et al. (2019), Queutey et al. (2016) and Visonneau, Deng et al. (2016). During the Tokyo 2015 workshop many different predictions have been compared (Hino et al. 2021).

In the framework of NATO-AVT 253 "Assessment of Prediction Methods for Large Amplitude Dynamic Manoeuvres for Naval Vehicles" drift (8° incidence) and sway inflow conditions have been studied experimentally and numerically, see also Shevchuk et al. (2020) and Fig. 2.8. The flow properties at the vortex centre are considered. The importance of proper grid resolution and consideration of DES-like pitfalls is highlighted. At the FSV the initially high total TKE decreases and the possible origin of missing grid resolution is mentioned. The axial velocity reveals a deficit of about 30%.

DTMB5415 The hull DTMB 5415 is a model of a slender US Navy surface combatant designed by the David Taylor Model Basin (DTMB). As the hull narrows above the waterline, it is also called ONR Tumblehome. Two special characteristics of the model are the sonar-dome bow and the transom stern. Mostly the model is used as a bare hull with bilge keels. It was investigated at straight-ahead, sway and drift conditions (10 and 20°).

Following on the previous work in NATO AVT-183, AVT-253 (Toxopeus, Jasak et al. 2020) deals with the flow around the 5415 hull at 10°. Here, new towing-tank experiments with TPIV are conducted and several new simulations by different groups with focus on hybrid RANS-LES are done. CFD results are provided by several groups and include linear and non-linear RANS and different hybrid RANS-LES approaches. Hull forces can accurately be modelled with RANS and less accurately with hybrid RANS-LES. But RANS approaches significantly underpredict both vortex strength and core TKE. The authors do not observe "[consistent improvements of] non-linear RANS models [...] over linear models". Concerning vortex progression, the core location and velocity magnitude are predicted well with hybrid RANS-LES. But the vortex strength and TKE shows a wide variation between the submissions, mostly both are significantly underpredicted in comparison to EFD. Only on the fine grids the strength and TKE are overpredicted at vortex onset. The error is about 20%. Additionally, the analysis of the TKE budget at the vortex centre shows contradictory results between two submissions (p. 70). Therefore, the authors propose to further investigate the prediction of vortex flow with hybrid RANS-LES approaches. A focus should be set on modelling (boundary layer shielding) and numerical (vortex grid refinement) aspects.

Further interpretations of the results are provided by Visonneau, Guilmineau et al. (2018, 2020a) and Visonneau, Guilmineau et al. (2020b). Non-/linear RANS models predict a relaminarisation of the core flow, so a reduction of TKE, during its progression, but this is not confirmed by EFD. Both EFD and hybrid RANS-LES models show the coexistence of local maxima for TKE and vorticity along the whole vortex path until ship's stern. This effect can be predicted only by hybrid RANS-LES, as the small unsteady vortices that form the average coherent vortex are resolved. An unsteady separation at vortex onset downstream of the sonar dome leads to the high levels of TKE in the core. Along the whole vortex path the production of TKE is maintained at a high level which is revealed by an analysis of the TKE budget. The authors conclude that "none of the RANS approaches was able to predict the right flow physics in the core of these vortices". Further numerical results with similar findings are presented by Bhushan, Yoon, Stern et al. (2019) and Bhushan, Yoon, Stern (2016)

Further Hulls Fewer investigations have been conducted on the series 60 $C_B = 0.6$ hull, see e.g. Longo, Stern (2002) and Tahara et al. (2002). Towing tank experiments and RANS approaches were conducted to reveal hull forces, wave pattern and the wake field. Furthermore, the Delft catamaran Delft-372 as a twin-hull was extensively studied, see e.g. Broglia et al. (2020) and Dogan (2013). Both RANS and DES approaches were

used to predict the free-surface pattern and the vortex system between 0 and 30° drift. As a consequence of the twin-hull the interaction drives the vortex system and the investigation.

Similar Bodies Next to wingtip vortices there are many technical applications where trailing vortices have a significant impact on the near-field flow. The followings examples are restricted to bodies with an aspect ratio in the range of ships or even smaller. Any vehicle experiencing inclined inflow, e.g. submarines, trains or cars, generate trailing vortices. Streamlined body parts, like the submarine's tower, render a distinct vortex evolution (e.g. Broglia et al. (2020) and Xue et al. (2020)).

Simple shapes are analysed in order to retrieve general conclusions. Liefendahl et al. (2020) e.g. analysed a generic elliptical spheroid - that is basically similar to a bare submarine - at 10 and 20° drift to reveal general conclusions on the potential of different turbulence modelling approaches within ship flows. RANS provides good results for the mean flow but bad ones for higher statistical orders, i.e. turbulence properties. And IDDES on RANS and LES grids shows "confusing" results. The onset of separation is possibly not as well defined as for a blunt ship hull and less pronounced so the grey-area issue is bigger here.

Summary on Vortex Characteristics The following findings can be summarized from the research mentioned above: RANS approaches can accurately predict hull forces and moments, hybrid RANS-LES approaches show a higher margin of error; usually an underprediction attributed to the log-layer mismatch (LLM) or missing resolved turbulence[27]. If trailing vortices progress downstream close to the hull, hybrid models may improve the prediction of the side or lift force distribution as the proper prediction of the vortex is necessary. This case resembles a leading-edge vortex of a delta wing that generated 'vortex lift' (Green 1995, p. 373, 463).

Considering the instantaneous complex core flow and its turbulent stresses, the prediction requires a resolution of most of the bulk TKE which is the target of hybrid RANS-LES approaches. Even anisotropic RANS models fail and erroneously tend to predict a relaminarisation instead of the coincidence of high TKE and high vorticity levels.

[27] As the turbulence transport across the RANS-LES interface is not reproduced, there is a deficit of resolved stresses which leads to an underprediction of the friction (Kornev, Shevchuk et al. 2019, p. 94), see also grey-area effect and MSD for further information.

3. Turbulence Modelling

Turbulence and its modelling play a central part in the formation of vortices: the boundary layer, usually turbulent in technical flows, separates into a so-called free-shear layer that rolls up into the vortex. Turbulence may be produced for a strong separation and entrained into the vortex. However, vortices tend to relaminarise close to the core. As turbulence marks a delicate topic for vortex flows, the present chapter provides fundamentals of the physical features of turbulence, their mathematical modelling and numerical realisation.

3.1. Turbulence as a Phenomenon

An intuitive approach to turbulence may be gained best by analysing photos (or videos) of its chaotic nature. The extensive collection in Van Dyke (1982) is one possibility, see Fig. 3.1. Laminar flows consist of ordered flow structures. An example is the thin and

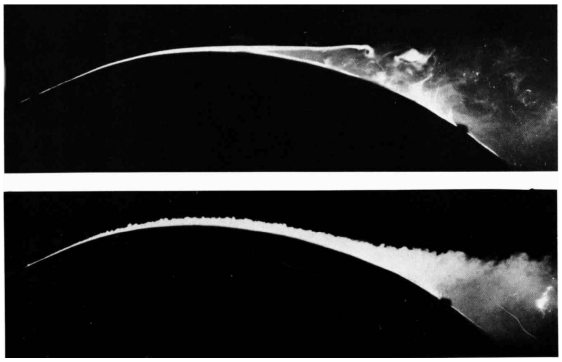

Figure 3.1.: Comparison of laminar and turbulent separating boundary layer flows over a convex surface (Van Dyke 1982, p. 91).

straight boundary layer separation in the figure. The clarity of the flow pattern manifests in the comparison to its opposite: a turbulent flow. The bottom figure shows the separation in turbulent state that seems to be driven by the presence of chaos. Turbulent flows are the usual formation and this has driven its understanding and modelling for more than hundred years (Boussinesq 1877; Reynolds 1895). The most apparent characteristic of turbulent flows is the certain randomness that manifests in strong spatial and temporal variations. The flow is unstable and reacts to all kinds of perturbations. Flow structures

occur within a large spatial range: from dimensions close to the boundary conditions to tiny ones representing diffusion. Mixing describes the interaction of these structures, that can be represented by the stretching of vortical structures which is accompanied by a transfer of energy along the whole range. Valuable phenological descriptions can be found in e.g. Pope (2000), Sagaut et al. (2013) and Versteeg, Malalasekera (2007).

3.2. Turbulence Modelling

The following section aims to explain different accesses to the modelling of turbulence. The basis is the statistical description of fluctuations in the fluid which is a basis for simple turbulence models and a possibility for the description of measured or resolved turbulence. Turbulence modelling and resolving approaches will be described. The model used for the flow simulations was presented by Gritskevich et al. (2012) and implemented by Shevchuk (2016). The repetition of its detailed description is omitted.

The Navier-Stokes equations 3.1 and 3.2 provide a complete set of equations that describe the flow, this includes also turbulent flow. In the presence of turbulence the flow field includes the turbulent motions which cover a large spatial range. The continuity and momentum[1] equation for an incompressible Newtonian fluid can be written like in Pope (2000, ch. 2):

$$\frac{\partial u_i}{\partial x_i} = 0 \tag{3.1}$$

$$\frac{D u_i}{D t} = -\frac{1}{\rho}\frac{\partial p}{\partial x_i} + \nu \frac{\partial^2 u_i}{\partial x_j^2} \tag{3.2}$$

with p and u_i as pressure and velocity, kinematic viscosity ν and with the substantial derivative

$$\frac{D u_i}{D t} = \frac{\partial u_i}{\partial t} + u_j \frac{\partial u_i}{\partial x_j}. \tag{3.3}$$

In vector notation both equations are

$$\nabla \cdot \boldsymbol{U} = 0 \tag{3.4}$$

$$\frac{D \boldsymbol{U}}{D t} = -\frac{1}{\rho}\nabla p + \nu \Delta \boldsymbol{U} \tag{3.5}$$

with the velocity vector $\boldsymbol{U}$ and the Laplace operator $\Delta = \nabla^2$.

[1] The last term on the right-hand side was simplified with the continuity equation.

The approaches dealing with turbulent flows can be roughly distinguished into three groups: those that model turbulence effects, those that resolve turbulent fluctuations, also termed turbulent-flow simulation, and those that both model and resolve a part of the turbulent flow. Considering the latter approach generally, several ways exist to combine modelling and resolving. These three groups of approaches are RANS equations with turbulence models, DNS and LES. Within this section, the RANS approach and the hybrid RANS-LES approach as a combination of RANS and LES will be analysed in detail.

3.2.1. Reynolds-Averaged Navier-Stokes (RANS) Equations

For many flows of technical relevance, statistical conclusions on the flow are satisfactory, e.g. on the resistance of bodies or the global pattern of flows. The RANS approach aims at solving the mean flow and modelling statistical fluctuations. The following short overview is based on Pope (2000), Versteeg, Malalasekera (2007) and Wilcox (2006). The RANS equations are a statistical formulation of the Navier-Stokes equations and form the basis for so-called RANS turbulence models that are part of the following section.

Reynolds (1895) proposed the decomposition of the instantaneous flow ϕ into a mean part $\overline{\phi}$ and a fluctuating part ϕ'

$$\phi = \overline{\phi} + \phi'. \tag{3.6}$$

Introducing the Reynolds decomposition for the velocity and pressure field into the continuity 3.1 and the momentum equation 3.2 and taking the mean yields the well-known set of equations for the mean flow (Pope 2000, ch. 4)

$$\frac{\partial \overline{u_i}}{\partial x_i} = 0 \tag{3.7}$$

$$\frac{\partial \overline{u_i}}{\partial t} + \overline{u_j} \frac{\partial \overline{u_i}}{\partial x_j} = -\frac{1}{\rho} \frac{\partial \overline{p}}{\partial x_i} + \nu \frac{\partial^2 \overline{u_i}}{\partial x_j^2} - \frac{\partial \overline{u_i' u_j'}}{\partial x_j}. \tag{3.8}$$

Both equations together are referred to as the Reynolds-Averaged Navier-Stokes (RANS) equations.[2] The difference between the Navier-Stokes momentum equation 3.2 and the RANS momentum equation 3.8 are the velocity covariances

$$\overline{u_i' u_j'}. \tag{3.9}$$

They incorporate the effects of velocity fluctuations on the mean flow field, the corresponding stress is $-\rho\,\overline{u_i' u_j'}$. These so called Reynolds stresses originate from the Reynolds-averaging of the non-linear convection term. Compared to the viscous stresses $\mu\,\nabla^2 U$ (with the dynamic viscosity) the Reynolds stresses may dominate. They represent the effect of turbulent fluctuations on the mean flow.

[2] Here, the RANS momentum equation 3.8 contains a time derivation which actually is termed unsteady RANS (URANS) equation. Refer to Sagaut et al. (2013, p. 237) for transient modelling aspects.

The four RANS equations contain more than four unknowns: three velocity components, the pressure and six Reynolds stresses. Following, this system of equations cannot be solved without additional information on the flow fluctuations: this is termed the closure problem. A solution is the use of a turbulence model that closes the system of equations. Refer to the next section for details on RANS turbulence models.

Independent of the use of the RANS equations to model turbulent flows, the following remarks provide information on the analysis of turbulent flows - using the RANS equations. First, the Reynolds stress tensor is described as it may also be used for the interpretation of turbulent flow in both experiments or scale-resolving simulations (SRS). The stresses are symmetric what follows from their definition in Eq. 3.9. Normal stresses ($\overline{u_i'^2}$) fill the diagonal components and shear stresses (e.g. $\overline{u_y' u_z'}$) fill the off-diagonal components. The turbulent kinetic energy (TKE) k is defined as half the trace of the stress tensor

$$k = \frac{1}{2}\,\overline{u_i' u_i'} = \frac{1}{2}\left(\overline{u_x'^2} + \overline{u_y'^2} + \overline{u_z'^2}\right) \tag{3.10}$$

and represents the mean kinetic energy (per unit mass) in the unsteady velocity field. Pope (2000, p. 88, 121) provides further relations that describe statistical details of the complex flow.

3.2.2. RANS Turbulence Models

Reynolds-averaging of the Navier-Stokes equations adds up six unknowns, the Reynolds stress components $\overline{u_i' u_j'}$, to the continuity and momentum equations so that the system of equations becomes unclosed. This system can be closed by the introduction of turbulence models. These model the effect of turbulent velocity fluctuations, represented by the Reynolds stresses, on the mean flow field. Hence, the details of the unsteady oscillations cannot be predicted, or in other words, only the mean flow field $\overline{u_i}$ is resolved. For many engineering views on technical flows this limitation is no drawback. In contrast, the efficient prediction of mean quantities is highly appreciated.

Two approaches of RANS turbulence models can be distinguished: turbulent-viscosity models are based on Boussinesq's hypothesis that introduces the turbulent viscosity ν_T similarly to the physical viscosity. Reynolds-stress models provide additional transport equations to model all Reynolds-stress components. Both approaches are presented in the following.

Turbulent-Viscosity Models Boussinesq (1877) proposed the turbulent-viscosity (or eddy-viscosity) hypothesis that describes the Reynolds stresses similar to viscous stresses in a Newtonian fluid: proportional to the mean strain-rate

$$-\rho\,\overline{u_i' u_j'} = \rho\,\nu_T\,\overline{S}_{ij} - \frac{2}{3}\,\rho\,k\,\delta_{ij}. \tag{3.11}$$

The turbulent viscosity ν_T is the positive proportionality factor, k is the turbulent kinetic energy (TKE), δ_{ij} the Kronecker delta and $\overline{S}_{ij}$ the mean rate-of-strain tensor

$$\overline{S}_{ij} = \frac{\partial \overline{u_i}}{\partial x_j} + \frac{\partial \overline{u_j}}{\partial x_i}. \tag{3.12}$$

Turbulent-viscosity models predict ν_T and so close the RANS equation system 3.7 and 3.8.

RANS turbulence models provide good results for simple shear flows (Pope 2000, p. 365). However, the turbulent-viscosity hypothesis predicts significant errors e.g. for strongly swirling flows (Sagaut et al. 2013, p. 234). This is a consequence from the alignment of the Reynolds-stress tensor with the mean-strain rate tensor.

Advanced Formulations Apart from well-known isotropic RANS approaches there are advanced formulations considering the anisotropy of the Reynolds-stress tensor. As full Reynolds-Stress Models (RSM) tend to reveal stability issues (Wilcox 2006) nonlinear formulations of the eddy-viscosity relation or (explicit) algebraic RSM (E/ARSM) provide a proper compromise between isotropic modelling and turbulence resolving approaches. The global potential of non-linear constitutive relations in closing the gap between efficient and expensive approaches is highlighted within the extensive monograph of Stern, J. Yang et al. (2013), because the increase in accuracy overwhelms the increase in effort. They permit the prediction of inhomogeneous and anisotropic stresses inside the vortex core, see e.g. Churchfield, Blaisdell (2013) and Revell et al. (2011) for lag-RST model that captures the stress-strain lag using a third transport equation. Although the latter effect is captured the model comprises a limited improvement of the mean-flow features compared to an isotropic Spalart-Allmars model with curvature correction (P. R. Spalart, M. Shur 1997). As mentioned by P. R. Spalart, Garbaruk (2019) RANS models with curvature-correction tend to overpredict relaminarisation inside vortex cores.

Additionally, a distinct feature of trailing vortices in the near field, the coexistence of both high vorticity and TKE inside the core, can be predicted only with partly resolving approaches like DES, see e.g. Visonneau, Guilmineau et al. (2020b): the sensitised EARSM (Hellsten, Wallin 2009) fails in this regard. Similar observations were presented e.g. in Schauerhamer, Robinson (2017). For an impressive insight into a different modelling topic dealing with model predictive control refer to Cisneros et al. (2016).

3.2.3. Hybrid RANS-LES Models

A proper prediction of the vortex flow needs to consider the evolution of the turbulent flow. Modelling turbulence inside the attached boundary layer and resolving the complex unsteady flow features around the trailing vortex is a promising approach: the simulation of the detached eddies, DES, also called hybrid RANS-LES.

Preliminary Remarks on the Concept of Large-Eddy Simulation (LES) This paragraph provides a short introduction into the LES approach to highlight aspects that become important for hybrid RANS-LES models, i.e. its LES-sub region. LES targets to resolve the 'large' scales of a turbulent flow and model the effect of the smaller-scale motions. A motivation for the separation into large and small scales is the assumption that the large scales depend on the boundary conditions and contain the majority of the Reynolds stresses. Due to turbulent mixing small scales are more isotropic, less dependent on individual boundary conditions and so more suitable for simple modelling. Pope (2000) addresses four conceptual steps:

1. A filtering operation is used to split up the velocity field into a resolved (i.e. filtered) and a residual part, also called subgrid-scale). The resolved velocity field contains the 'large' eddies.
2. The underlying equations for the resolved part are similar to the Navier-Stokes equations Eq. 3.2. The difference is the addition of the residual-stress tensor (also called sub-grid scale - SGS - tensor) like the Reynolds stress tensor for the RANS equations.
3. The system of equations is closed by modelling the residual-stress tensor. This model is similar to an eddy-viscosity model.
4. The numerical solution "provides an approximation to the large-scale motions in one realization of the turbulent flow" (Pope 2000, p. 559). This highlights the complex unsteady nature of turbulent flows and the statistical modelling.

The resolution of the near-wall flow is extremely expensive because "all eddies are small" (Wilcox 2006, p. 436). However, the computational effort inside strong mixing zones is manageable. Whereas "grid refinement aims at numerical accuracy" within RANS approaches, it "weakens the role of the modelled eddies" within LES approaches and so targets to "enrich turbulence physics" (Sagaut et al. 2013, p. 236). Or in other words, modelled stresses correlate with the grid spacing which is not the case for RANS.

Mockett (2009) summarises important demands to the numerical scheme and grid resolution. The numerical dissipation should be minimised and the mesh should be isotropic to account for the 3D structure of the turbulent flow. Pope (2000, p. 560) stated that the mesh resolution should allow the resolution of at least 80% of the total TKE.

Concept

Hybrid RANS-LES models combine the statistical modelling of turbulent flows with RANS approaches and the partial resolution of the turbulent flow field with LES approaches. Different realisations of the coupling between RANS and LES exist which are represented by well-known methods: e.g. SAS, VLES, DES, WMLES or zonal/ embedded LES. A categorisation of hybrid approaches can be found in Fröhlich, Von Terzi (2008), Gritskevich et al. (2012), Mockett (2009) and Sagaut et al. (2013) and is not repeated here, because the present approach relies on one approach only: detached-eddy simulation (DES). This choice will be explained during the description of the method.

Both approaches RANS and LES differ extremely in terms of computational costs and in terms of accuracy considering flows in general: in a nutshell, RANS is fast and LES is accurate. However, in some flow regimes RANS models provide accurate results and in other regimes the computational costs of LES are acceptable: attached boundary-layer flows are well predicted by RANS models and zones with large eddies (massive separation) require an acceptable level of resources for LES. Refer for further information e.g. Mockett (2009, p. 52) or Sagaut et al. (2013, p. 234). The intention of DES as a hybrid RANS-LES approach is to benefit of each model's advantage for different flow regimes: using RANS in attached boundary-layer flows and LES for "detached eddies" or in other words: for flow separation regions with large unsteady structures.

How is the combination of RANS and LES realised within the DES approach? The DES approach relies on one turbulence model within the whole computational domain that acts as a subgrid-scale model in regions with proper grid resolution for LES and as a RANS model in the other regions. Following the motivation for a hybrid approach, wall-bounded flows are modelled with a RANS model and mixing zones with high grid density are resolved with LES. Usually, a RANS turbulence model is chosen as base model which is modified to act as a subgrid model inside LES regimes (Fröhlich, Von Terzi 2008, p. 355). Following the use of a single turbulence model is possible. This model contains an automated switch to distinguish between RANS and LES. No preliminary decomposition of the computational domain by the user is required. It is possible because the LES equations are conceptually similar to the RANS equations, both contain a term to model turbulent stresses (sub-grid or Reynolds stresses respectively).

The switch between RANS and LES is assumed to take place at the so-called interface, although the change happens in a continuous manner as variables are blended. A critical part from modelling view is the missing conversion between modelled and resolved turbulent fluctuations at the interface. Considering for example an interface with upstream RANS part, the modelled Reynolds stresses are not reconstructed to resolved velocity fluctuations - these need to develop within the LES part from inherent flow instabilities. The so-called grey area is referred below again.

In the following, selected models are presented: the original model and improved ones.

First Model Formulation P. R. Spalart, Jou et al. (1997) proposed the initial DES model formulation and designated it DES97. Although several improvements and modifications have been presented, this model consists of a very straight formulation which helps to highlight the main DES aspect: the switch between two different strategies to deal with turbulence. Taking the Spalart-Allmaras eddy-viscosity RANS model as a basis, its length scale L_{RANS} is replaced with the DES length scale

$$L_{DES} = \min\left(L_{RANS}, L_{LES}\right) \tag{3.13}$$
$$L_{RANS} = d_w \tag{3.14}$$
$$L_{LES} = C_{DES}\,\Delta \tag{3.15}$$
$$\Delta = \max\left(\Delta_i, \Delta_j, \Delta_k\right), \tag{3.16}$$

where d_w is the distance to the nearest wall, C_{DES} a model constant and $\Delta_{i/j/k}$ the local cell size for the hexahedral structured grid. Near walls a RANS mesh is highly anisotropic with a small spacing in the wall-normal direction and much larger spacings in wall-parallel directions. Following, near to the wall ($d_w < L_{LES}$) the model acts in RANS mode ($L_{DES} = L_{RANS}$). Far away from the wall where the mesh usually becomes isotropic, the grid-dependent LES length scale is used. The authors showed that the basic RANS model acts as a proper subgrid-scale (SGS) model inside the LES region, see Mockett (2009, p. 54, 74) and Sagaut et al. (2013, p. 271).

Sagaut et al. presented Fig. 3.2 which shows the separation of a boundary layer flow. The upstream boundary layer is modelled with URANS because its thickness δ is smaller then the LES length scale: $d_w \leq \delta < C_{DES}\,\Delta$. The "detached eddies" downstream of the separation are resolved with LES as the grid is fine enough $L_{RANS} > C_{DES}\,\Delta$. As the unsteady pressure field inside the LES region acts onto the boundary layer flow (represented with $P(t)$), the latter becomes unsteady (URANS). Inside the so-called "grey area" zone the modelling behaviour is questionable, this aspect is addressed below.

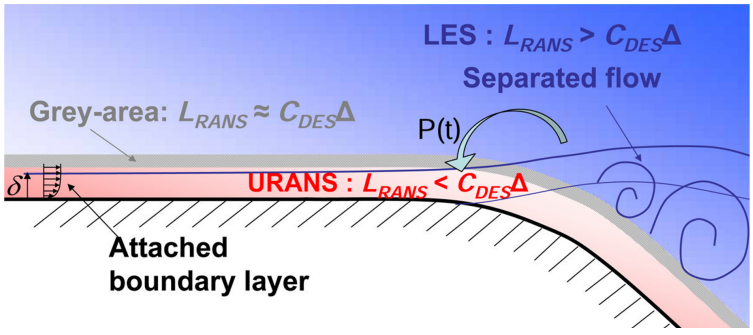

Figure 3.2.: Exemplary visualisation of RANS and LES regions within a DES approach, from Sagaut et al. (2013, p. 267).

The location of the interface between RANS and LES is determined only by the grid. If the boundary layer thickness is smaller than the LES length scale $\delta < C_{DES}\,\Delta$, LES

will be activated inside the boundary layer flow without proper LES resolution. This drawback can be omitted with model modifications presented below.

The DES model presented can be formulated also for different RANS turbulence models. But then the formulation is less straight because the RANS length scale is explicitly/ implicitly contained in multiple terms of the RANS model's transport equations (Mockett 2009, p. 55).

Shortcomings Several shortcomings of the original model formulation exist which were partly addressed in P. R. Spalart, Jou et al. (1997). These relate generally to the RANS-LES interface.

Around the RANS-LES interface there is a region where neither RANS nor LES is properly applied, because the resolved turbulent fluctuations are not reconstructed from modelled ones in the RANS part and so need to develop from inherent flow instabilities. The developers of DES (P. R. Spalart, Jou et al. 1997; P. Spalart 2000) termed this region the **grey area**. Further information can also be found in (Mockett 2009, p. 57) and Sagaut et al. (2013, p. 280, 283).

Right downstream of the interface, the Reynolds stresses or the turbulent kinetic energy are underpredicted. P. R. Spalart, Deck et al. (2006) termed this effect **Modelled-Stress Depletion** (MSD) to highlight that the RANS "modelled" turbulence is not resolved by LES. So the missing resolved turbulent fluctuations near the RANS-LES interface can be designated as MSD inside the grey area. This effect highlights the importance of flow instabilities that lead to the fast generation of resolved turbulence.

If the interface is located inside the boundary layer, MSD can lead to flow separation, because it is accompanied with less skin friction. This effect is termed **Grid-Induced Separation** (GIS). Aside from this, both velocity profiles inside the boundary layer predicted by RANS and by LES would reveal a mismatch which was termed **Log-Layer Mismatch** (LLM) (P. R. Spalart, Deck et al. 2006). The mentioned drawback of the original formulation has led to the formulation of various modifications. In the following, a brief description of the formulation that will be applied later is presented.

Delayed DES The "incursion of the LES mode inside the boundary layer" (Mockett 2009, p. 56) leads to MSD and may enforce GIS. A solution is the "shielding" of the boundary layer from LES activity. In the present thesis, the formulation of Gritskevich et al. (2012) is used. It is a combination of the model presented in M. Strelets (2001) with the shielding presented in P. R. Spalart, Deck et al. (2006) adapted to the SST model (F. Menter, Esch 2001): SST-**DDES**. Further evaluation on the model can also be found in Sagaut et al. (2013, pp. 286).

Improved DDES Within the present thesis, the **SST-based IDDES** model proposed by Gritskevich et al. (2012) was used. Originally proposed by M. L. Shur, P. R. Spalart et al. (2008), it "[addresses] the bridge between wall-resolved and wall-modelled DDES" (Sagaut et al. 2013, p. 289) switching between the DDES and the wall-modelled LES (WMLES) branch. The model targets to reduce the occurrence of MSD as WMLES may be activated if the grid resolution close to the wall allows it. Consider the above mentioned publications for further details on the IDDES length scale and the subgrid length scale.

Mockett (2009, p. 52) pointed out that the requirements for the spatial and temporal resolution within the LES zone for hybrid models are inherited from general LES. This aspect will be addressed in Sec. 5.2. The emergence of turbulent fluctuations for the present case is discussed in Sec. 5.1.1. For details on the actual numerical setup refer to Sec. 4.3.

4. Test-Case Setup

Details on the physical and numerial setup of the flow configuration are presented within the present chapter. As experiments form the basis for the investigation these are shortly described first. Following, a physical description of the flow and the evaluation and secondly, the numerical considerations on the realisation dealing with schemes, algorithms and the grid are presented.

4.1. Experiments

Wind-tunnel experiments form the basis for the whole investigation of the vortex flow. These experiments of a double-body KVLCC2 hull model were conducted in 2020 at Hamburg University of Technology. At the time of writing they were not finally processed and so may be considered for a future comparison with CFD. However, the setup prescribes the boundary conditions of the flow and therewith have a distinct influence on the flow simulations.

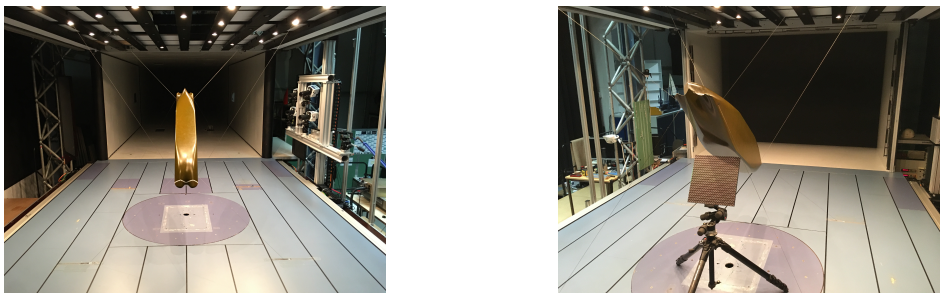

(a) Front-view, laser and cameras on the right, oil seeding on the bottom further downstream.

(b) Target used for the calibration of the measurement system.

Figure 4.1.: Arrangement of the double-body model inside the wind-tunnel's test section. The orientation is termed 'bow down'.

Figure 4.1 depicts the placement of the KVLCC2 model with 30° drift inside the open test section. The model dimensions coincide with the numerical ones, see Tab. 2.1, the test section dimensions are: height 2m, width 3m and length 5.5m. On one side of the model there are plates embedded into the bottom. The tiny gaps may act as trip wires supporting laminar-turbulent transition. This side relates to the little weaker vortex.

Trip wires in the form of zig-zag strips are attached to the bulbous bow at the forward perpendicular to assure transition. Operated in closed circuit loop mode, the low-speed wind tunnel presets the inflow of 25 m/s with a turbulence intensity of below 0.3%. A higher inflow speed is not considered in order to avoid disturbing model vibrations.

Tomographic Particle Image Velocimetry is used to capture the flow inside the measuring planes at a frequency of 500 Hz. Tracer particles of Di-Ethyl-Hexyl-Sebacat (a kind of oil abbreviated DEHS) are illuminated by a laser and their trajectories reveal the 3D-velocity field. For further details on the measurement technique refer to Raffel et al. (2018, ch. 9.2) or Wieneke (2017). As multiple layers in proximity to the plane are placed, spatial gradients in all directions can be determined, e.g. the complete vorticity vector. This is the improvement of T-PIV compared to stereoscopic or S-PIV. Inside vortex cores the accumulation of particles is slightly reduced due to the higher density compared to air, see e.g. Liew et al. (2013). The measuring planes are frame-planes, see e.g. Fig. 5.5. Four 4MP cameras record the double-pulsed laser reflections. There is no intrusion into the test section for a minor influence onto the flow. Comparing camera resolution and field of view leads to a resolution of about nine pixel for each millimetre.

The fine temporal three-dimensional resolution of the vortex flow allows a statistical comparison with the turbulent flow simulations.

4.2. Physical Aspects

The KVLCC2 hull's dimensions are shown in Tab. 2.1 and further information is provided within the corresponding section 2.3.1. It is aligned by 30° to the inflow. The average temperature during the measurements in the summer of 2020 at TUHH was about 22°C with a deviation of about ±2°C. So the viscosity of air is set to exactly $\nu = 1.52 \cdot 10^{-5}\mathrm{m/s}^2$ that corresponds to a Reynolds number of $Re_{L_{oa}} \approx 2.6 \cdot 10^6$. The inflow turbulence is set to an intensity of 0.3% with an eddy viscosity ratio $\nu_t/\nu = 1$.[1]

Proper visualisations of the numerical setup can be found in Fig.s 5.4 and 5.5 that also shows part of the body plan, the coordinate system and the vortices studied. The origin of the coordinate system is placed in the forward perpendicular with x pointing towards the stern, y to the port side of the single-hull and z towards the single-hull's bottom. Figure 4.1 visualises the experimental placement of the model inside the wind-tunnel test section.

[1] Slight deviations are negligible here, because the bulk of turbulence develops as the bottom boundary layer separates, see Sec. 5.2.

Table 4.1 provides the location of the measuring planes used for the experimental and numerical analysis of the vortices. Generally, the planes are arranged every 0.1 m starting from the transom stern plane up- and downstream. The labelling X3, X4 etc. is used throughout the analysis of the results and links to the tenth of the x-coordinate, e.g. X12 is located at $x = \underline{1.2}61$ m. The planes X3b and X4b are used only within the numerical analysis for an increased spatial resolution of the initial FSV.

Table 4.1.: Measuring planes for FSV and ABV. Coordinate origin located in Forward Perpendicular (FP) in waterplane. The second column provides the distance to the transom stern (T-S) (upstream positive).

Name	T-S [m]	x [m]	x/L_{pp} [-]
X3	1.2	0.361	0.235
X3b	*1.15*	*0.411*	*0.268*
X4	1.1	0.461	0.300
X4b	*1.05*	*0.511*	*0.333*
X5	1	0.561	0.365
X6	0.9	0.661	0.431
X7	0.8	0.761	0.496
X8	0.7	0.861	0.561
X9	0.6	0.961	0.626
X10	0.5	1.061	0.691
X11	0.4	1.161	0.756
X12	0.3	1.261	0.821
X13	0.2	1.361	0.887
X14	0.1	1.461	0.952
X15	0	1.561	1.017
X16	-0.1	1.661	1.082
X17	-0.2	1.761	1.147

4.3. Numerical Aspects

First, the computational domain and mesh is described followed by a short presentation of the numerics used to solve the equations presented in Sec. 3.2. OpenFOAM (Weller et al. 1998) is used for the flow simulation with version v1806 and version v1912 for the generation of the grids with `snappyHexMesh`.

Domain and Mesh Details The computational domain extends from the symmetry plane about $1.4L_{pp}$ in z-direction and three times this distance along the y-axis as well as four times this distance along the x-axis. Figure 4.2a shows the mesh at the symmetry plane and the outline of the domain. The hexahedral mesh is created from an isotropic homogeneous block mesh with different density. OpenFOAM's meshing tool snappyHexMesh is used to build a hexahedral unstructured mesh with layers on the hull and refinement regions for the wake and the FSV and ABV cores onto the basic block

Table 4.2.: Properties of the single-hull meshes. The double-body mesh is generated from the medium one mirrored at the symmetry plane. Reduced layer expansion ratio in stern region indicated in parentheses.

Mesh	coarse g3	medium g2	fine g1	coarse-FSV g3fsv8
Cells along z #	16	20	25	16
Refinement factor	1	1.25	1.25	1
Base size [mm]	135	108	86.4	135
Wake size [mm]	2.11	1.69	1.35	2.11
Core size [mm]	1.05	0.84	0.68	0.53
Layer #	18	17	16	17
Exp. ratio	1.2 (1.18)	1.2 (1.18)	1.2 (1.18)	1.2
First layer [mm]	0.027	0.027	0.027	0.027
Coverage [%]	100	100	100	100
Cells # in M	15.6	28.4	52.2	32.8
Faces hull # in k	136	211	330	149

mesh. Figure 4.2 shows the refinement of the wake with boxes and the circular FSV and ABV refinement around the time-averaged vortex centres. The isoline represents the different vortices that are located inside refined regions. As the boundary layer flow is resolved, the mesh becomes fine close to the hull. Figure B.1 depicts the layer cells and the transition to the hexahedral cells.

Table 4.2 provides details on the different meshes. The only differences between the coarse, medium and fine mesh is firstly the number of base cells for the underlying block mesh that increases from 16 with a factor of 1.25. The cell sizes are determined relative to the background mesh. And secondly the number of layers varies. The hull is refined six times (to the wake cell size) and seven times in the stern region to account for the strong separation there. Wake and core size refers to the cell size in the vortex wake and the FSV and ABV core, it refers to six and seven refinement steps and to eight steps for the g3fsv8 mesh. The latter is similar to the coarse mesh g3 with the exception of a refined FSV core. In order to fulfil grid quality constraints the number of added layers was limited. With the presented setup, a full layer coverage of 100% is obtained. Layers are extruded with the expansion ratio of 1.2 and 1.18 in the finer stern region. Generally the fine mesh results are shown.

An overview of the simulations that are evaluated in the next chapter can be found in Tab. 4.3. The use of 25 m/s inflow speed and the hybrid RANS-LES turbulence model is the default condition. Besides, two different inflow angles are investigated on the coarse mesh: straight ahead and 12°. For the medium mesh, the inflow speed is varied by ±24% to 19 and 31 m/s. And the medium mesh is mirrored to obtain a double-hull configuration.

Table 4.3.: Simulations conducted with different inflow, drift angle of attack (AoA) and turbulence modelling approach. The double-body (d-b) hull is created from the medium mesh g2. (*) For 12° the refinement zones for the FSV and ABV vortex cores and the wake are adapted, see Fig. B.2.

Mesh	coarse g3	medium g2	d-b g2	fine g1	coarse-FSV g3fsv8
U_∞ [m/s]	25	19, 25, 31	25	25	25
AoA [°]	0, 12*, 30	30	30	30	30
Turbulence	RANS, DES	DES	DES	DES	DES

As the flow is solved down to the viscous sub-layer, the dimensionless wall distance y^+ is set to unity. Its mean deviates by about 1%, the maximum value is about 3.

Turbulence Modelling A rather industrial approach to consider partially the vortex core flow characteristics is the use of a RANS turbulence model with curvature-correction, see e.g. Arolla, Durbin (2014) and M. L. Shur, M. K. Strelets et al. (2000). In accordance with the stablished SST model (F. Menter, Esch 2001; F. Menter, Kuntz et al. 2003), a corresponding curvature correction model is used (Smirnov, F. R. Menter 2009). As the wake flow reveals no separation of scales, see Fig. 5.35, an unsteady algorithm would render the approach questionable (Fröhlich, Von Terzi 2008; P. Spalart 2000). Instead, the steady SIMPLE algorithm is used.[2]

The turbulence-resolving approach is based on the SST-variant of a hybrid RANS-LES model according to Gritskevich et al. (2012): **SST-based IDDES**. Shevchuk (2016) implemented the model into the OpenFOAM framework and validated it, see also Kornev, Shevchuk et al. (2019) and Shevchuk et al. (2020). For details on the model formulation the reader is referred to Sec. 3.2. An example for the RANS-LES interface is shown in Fig. B.5.

Discretisation and Solver Details For the steady RANS simulations a default discretisation setting with linear-upwind schemes for the convection discretisation. The 'consistent' variant of the SIMPLE algorithm (Van Doormaal, Raithby 1984) is used with a relaxation of 0.9. Convergence is observed after some hundred iterations.

[2]The Semi-Implicit Algorithm for Pressure-Linked Equations was originally proposed by Patankar (2018) and is realised in OpenFOAM as the `simpleFoam` solver.

For the time-dependent solution of the hybrid RANS-LES approach, the PISO algorithm is used.[3] In order to introduce a minimal amount of numerical diffusion, the temporal terms are discretised with a second-order implicit scheme. Inside the LES part of the domain a blending between 99% central differencing and 1% linear upwind discretises the convective terms. To maintain stability inside the RANS region, the LES scheme is blended towards linear upwind according to M. Strelets (2001). An example for the realised blending is shown in Fig. B.5. Turbulent convective terms k and ω are discretised with a TVD scheme. The Laplacian operator is discretised using a linear second-order scheme with non-orthogonal correction (the coefficient of 0.5 assures that the non-orthogonal correction is smaller than the orthogonal part). Gradients are discretised with the hybrid Green-Gauss scheme presented in Shima et al. (2013).

Vuorinen et al. (2014) revealed the dissipative character of the undocumented flux correction in the PISO algorithm implemented in OpenFOAM, which therefore was not used within the present simulations. For a proper temporal resolution of the separation the maximum Courant number is set to 0.8, this leads to a mean time step of about $4.5 \cdot 10^{-6}$s on the fine mesh. Convergence of first and second moments of velocity was observed after $U_\infty * T/L_{pp} \approx 4.1$ which is used for the evaluation of the time-averaged flow. The results of the flow simulation are presented in the following section.

[3] The algorithm termed Pressure-Implicit with Splitting of Operators was developed by Issa (1986), see also Versteeg, Malalasekera (2007) for an explanation, and realised in OpenFOAM as the `pisoFoam` solver.

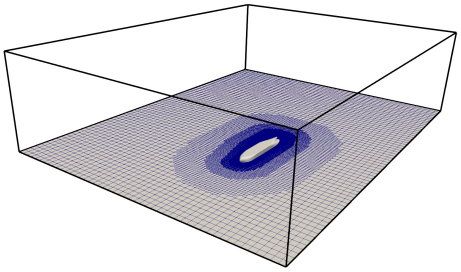

(a) Computational domain.

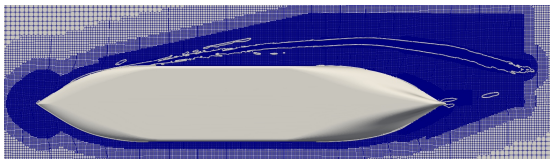

(b) Plane through FSV.

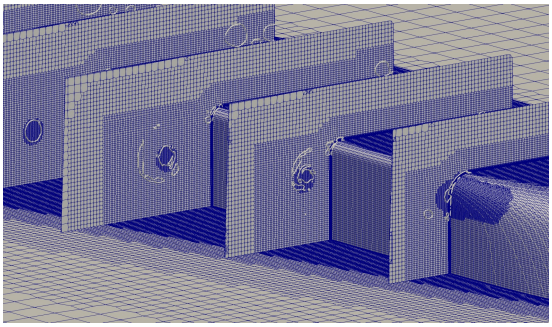

(c) Front view with FSV refinement.

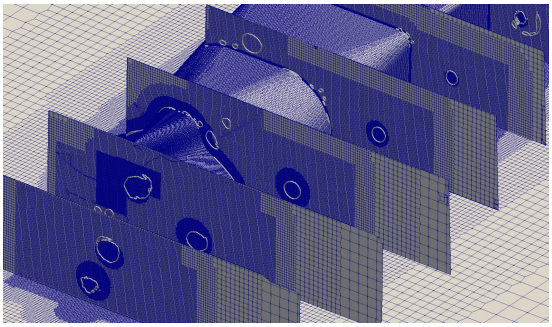

(d) Stern view with FSV, ABV and ASV.

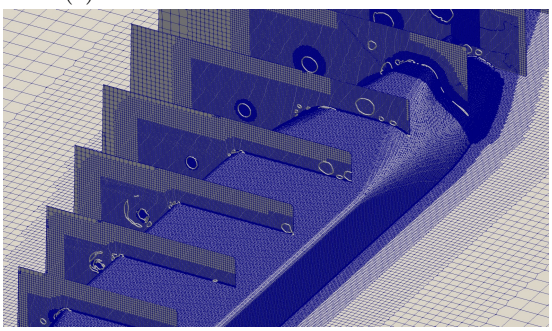

(e) Front view.

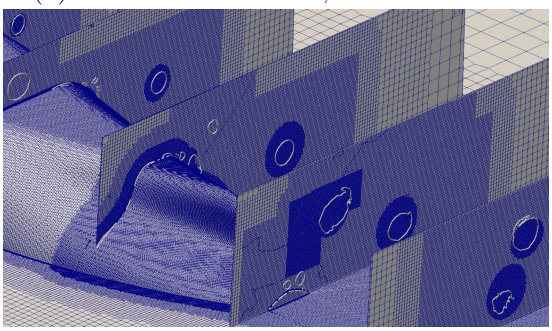

(f) Stern view.

Figure 4.2.: Visualisation of the (coarse) grid for the single-body mesh. The isolines represent $\overline{\lambda}_2 = 10^5$ [1/s].

5. Numerical Results

The central part of the present thesis is the numerical investigation of two major vortices: FSV that elongates along about two-thirds of the hull next to it and ABV that poses the strongest vortex near the stern. The turbulent flow is resolved with a scale resolving approach, termed DES, described in Sec. 3.2.3. The previous section provides further details on the physics and numerics of the setup.

The chapter starts with an introductory description of the global vortex flow features and a visual approach. Next, the verification of the numerical results is discussed. The structure follows starts with a global view of the whole vortex system, continues with the vortex motion itself, i.e. wandering, then with the analysis of the vicinity of the vortices and finishes with the consideration of the distinct centres.

In general the single-body fine mesh g1 is used. For the analysis of the double-body influence and flow visualisations the double-body medium mesh is used. In addition, the medium mesh g2 is used for the analysis of different inflow speeds and the coarse mesh is used with different drift angles. See also Tab. 4.3. Refer to appendix Sec. B.1 for a definition of flow variables used within the present chapter. Here, the focus is set on physical flow features. For additional numerical or statistical considerations refer to appendix Ch. B.

5.1. The Vortex System

This preliminary section provides an overview of the vortex system. Commonly investigated drift angles are treated with respect to physical and modelling aspects and main flow features for the distinct drift angles are presented. Following, major vortex flow characteristics are revealed shortly that will be further analysed focussing the vortex core in Sec. 5.4 and the vortex centre in Sec. 5.5.

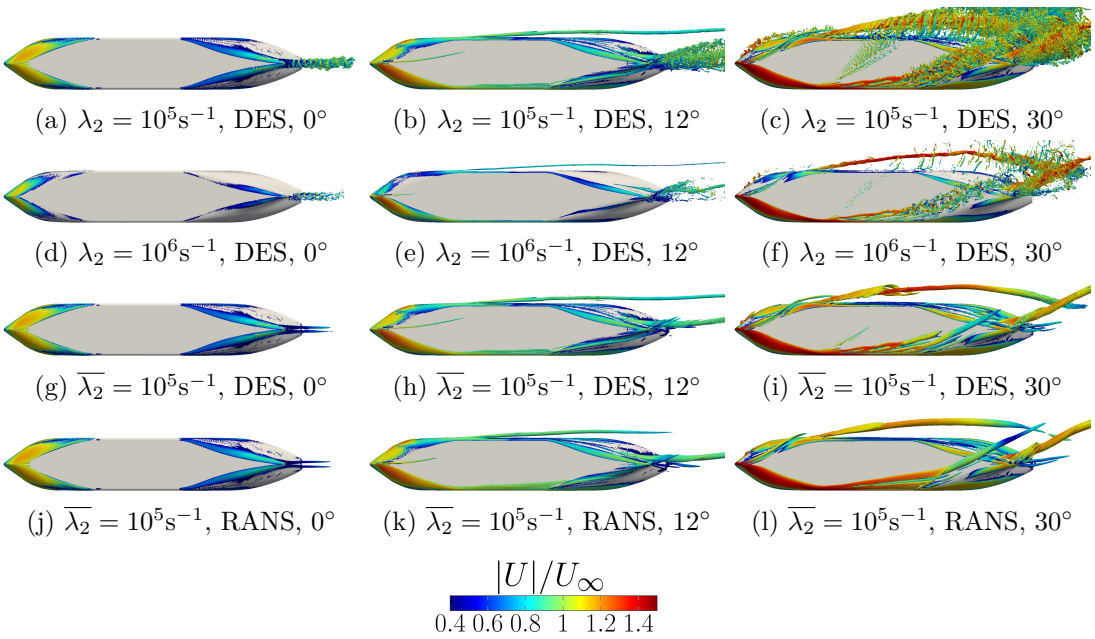

Figure 5.1.: Vortex system for three drift angles: straight ahead 0° (left), 12° (centre) and 30° (right column) coloured by velocity magnitude. CFD results obtained with DES and RANS (SST-CC) on the coarse mesh. Colour map below.

5.1.1. Different Drift Angles

Most existing experimental and numerical investigations on the KVLCC2 focused on three inflow angles: straight ahead, 12° and 30°, see also Sec. 2.3.1. Within the present section, CFD results with RANS and DES are compared to each other.[1] Preliminary EFD measurements are used to proof quantitatively the coexistence of vorticity and TKE inside the vortex core.

Figure 5.1 shows the corresponding vortex system obtained with DES and RANS (lowest row) on the coarse single-hull mesh. Two different isovalues represent instantaneous vortical structures of different strength. For straight ahead inflow, both turbulence models predict two symmetric stern vortices surrounded by some azimuthal structures. For 12° drift a distinct leewards vortex emerges that extends far and close along the hull but is not surrounded by secondary vortices. At the stern, many tiny eddies encompass the major separating vortex. At 30° drift, a bulk of eddies represents the strong separation along the leeward bilge, around the stern and on part of the windward bilge. A distinct vortex exists in the leeward wake, downstream of the stern and above the ship's bottom.

[1] A curvature-corrected variant of the SST model is used according to Smirnov, F. R. Menter (2009). For straight ahead inflow the mesh shown above is used, for 12° the refinement zones are adapted, see also Fig. B.2.

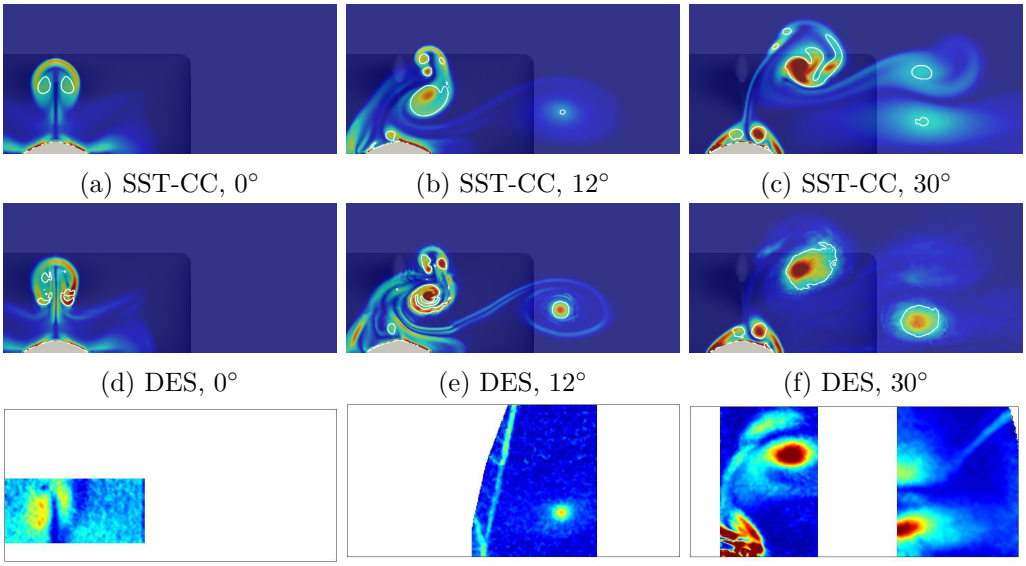

(a) SST-CC, 0° (b) SST-CC, 12° (c) SST-CC, 30°

(d) DES, 0° (e) DES, 12° (f) DES, 30°

(g) EFD, 0° (h) EFD, 12° (i) EFD, 30°

Figure 5.2.: Vorticity in transom stern plane.

All in all, steady RANS can predict quite well the presence and location of the different major vortices compared to DES. With increasing drift angle, the degree of inherent flow instabilities grows which manifests in the increasing density of vortical structures. The comparison of $\lambda_2 = 10^5 \mathrm{s}^{-1}$ and $\lambda_2 = 10^6 \mathrm{s}^{-1}$ reveals that for 0° and 12° these structures are spatially limited to a small portion of the wake near the stern.

The distinct flow in the wake reveals the potential and drawback of turbulence modelling RANS and resolving DES approaches. A qualitative comparison between RANS and DES and the EFD data for the turbulence intensity and the vorticity is shown in Fig.s 5.2 and 5.3, the axial velocity is shown in the appendix in Fig. B.3.[2] The three columns relate to three drift angles: straight ahead 0° (left), 12° (centre) and 30° (right column). The white isolines represent $\lambda_2(\overline{U}) = 10^5$ [1/s]. The hull is visible in the background for CFD, EFD relates to preliminary results. The turbulence represents the resolved part for DES and total one for RANS and EFD where the color map for the latter differs. For 12° no data can be shown.

The objective here is to show the importance of scale-resolving approaches dealing with coherent vortices that manifests in the coexistence of both high vorticity and high TKE inside vortex cores. For RANS, DES and EFD the vorticity peaks in the hull's boundary layer, in the free-shear layer and inside all vortices. The smooth field of the RANS result compared to the DES one is a consequence of the diffusivity of the turbulence modelling

[2]Concerning the comparison of CFD and EFD for 30°, it is important to note that this is the coarse mesh. Figure B.9 shows the influence of the grid refinement which would render the difference of especially the vorticity very small.

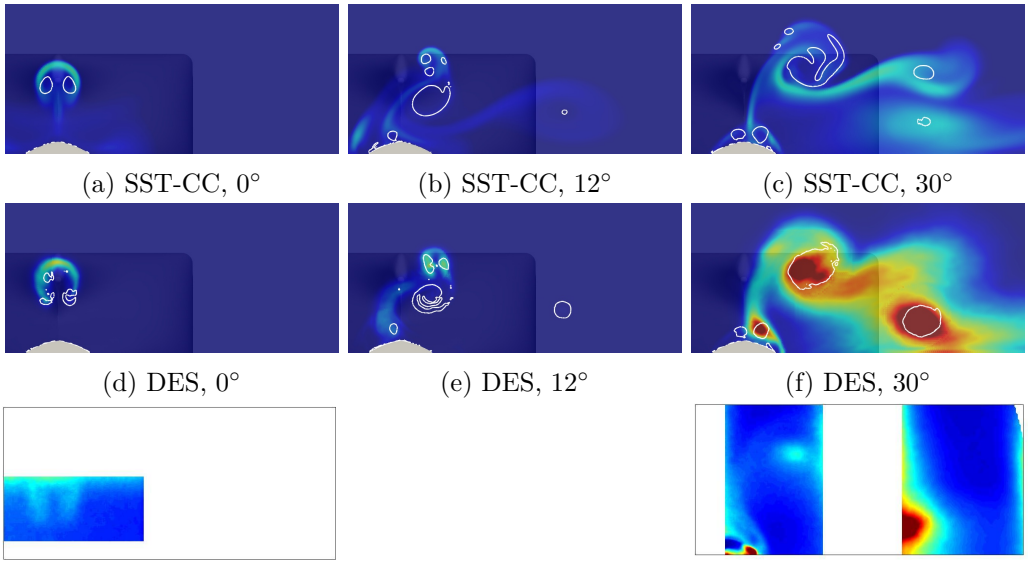

(a) SST-CC, 0° (b) SST-CC, 12° (c) SST-CC, 30°

(d) DES, 0° (e) DES, 12° (f) DES, 30°

(g) EFD, 0° (h) EFD, 30°

Figure 5.3.: Turbulence in transom stern plane.

approach. RANS predicts turbulence in the free-shear layer and little in the both right vortex cores for 30°. DES in contrast predicts a high turbulent intensity inside the vortex cores for 30°. And EFD reveals a local maximum inside the vortex cores as well.

All in all, considering modelling aspects both RANS and DES can predict the wake around the propeller for straight ahead well. Considering 12°, probably both approaches can predict the mean wake flow reasonably well because it is right downstream of a strong separation.[3] But the prediction of the leeward vortex (located right next to the hull) fails for both approaches: RANS is too diffusive and DES is not valid, because nearly no turbulence is resolved. This is clarified in Fig. B.2. And for 30°, most portion of total turbulence is resolved - see Fig. B.2 - and the vorticity accumulation inside the cores ispredicted with DES. This is not possible with RANS. The important physical flow aspect revealed is the coexistence of both local TKE and vorticity maxima inside the vortex cores. This has also been observed for similar cases (Visonneau, Deng et al. 2016, e.g.), see Sec. 2.3.2. Finally, this is an extensive example that motivates the choice of the high drift angle used in the following.

5.1.2. Steady Drift of 30°

Vortex System Figure 5.4 presents a qualitative view of the vortex system investigated thoroughly within the present thesis. For the naming convention, the reader is referred to

[3]RANS cannot predict the flow anisotropy, see e.g. Visonneau, Guilmineau et al. (2018). The strong separation around the stern leads to a small grey-area effect for DES.

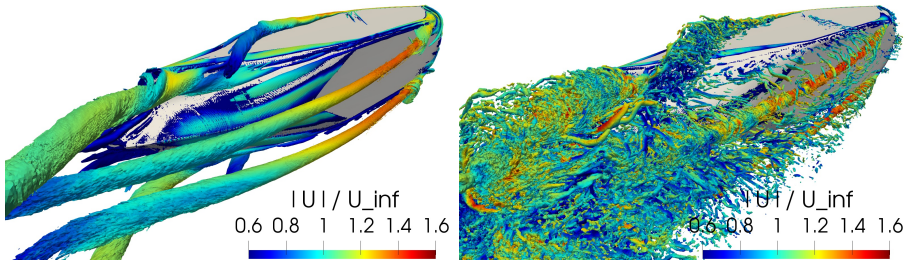

(a) $\overline{U}$ (b) U

Figure 5.4.: Vortex system around double-body model from rear view, left/ right subfigs show instantaneous/ time-averaged isosurface of $\lambda_2 = 10^6 \mathrm{s}^{-1}$/ $\overline{\lambda_2} = 10^5 \mathrm{s}^{-1}$, coloured by velocity magnitude, medium mesh (g2).

Fig. 1.5. The wake flow is dominated by the separation of the bottom's boundary layer and its roll up into the FSV and the strong separation of the ABV near the stern. Both vortices represent the two major trailing vortices, the ASV emerging from the bottom is considerably weaker and so diffuses earlier. Very upstream, vortex shedding occurs especially near the symmetry plane. The small-scale FBV is entrained into the larger FSV that in turn evolves without vortex interaction up to the stern region where the FSV and ABV behave similar to two co-rotating wingtip vortices: They "spiral around each other under their mutual induction and [would] ultimately merge to form a single vortex" (Devenport, Vogel et al. 1999, p. 357). A clear velocity excess is present for the initial FSV which is also surrounded by secondary structures originating from the separated boundary layer flow. Downstream of the rear shoulder, the number of eddies grows suddenly and covers the whole wake - a visual representation for the proper resolution of the bulk of turbulent energy.

Comparing a typical delta wing and the KVLCC2 hull reveals the similarity of a low aspect ratio and the difference that the hull is not swept-back. Taking the similarity as a basis, the FSV would correspond to a stabilized leading edge vortex. This is a possible approach for a classification of the FSV evolution and of its effect on the hull forces in terms of 'vortex lift', see e.g. Green (1995, p. 373, 463).

A quantitative representation of the FSV and ABV centres is provided in Fig. 5.5. Exemplary streamlines of the time-averaged flow represent the swirling flow around the vortex centrelines. The core radius is estimated from the tangential velocity profile along the $+y$-axis, and the wandering amplitude represents the standard deviation. Both vortex core radius and vortex displacement, also termed wandering, see Sec. 5.3, increase with downstream vortex progression. The planes within the wandering analysis of the vortices is conducted are labelled X3 to X17.

The flow in the x-planes is visualised in Fig. 5.6. As both FSV and ABV are approximately aligned parallel to the x-axis, the in-plane flow represents the swirling vortex flow. At upstream positions the characteristic peak tangential velocity is present but

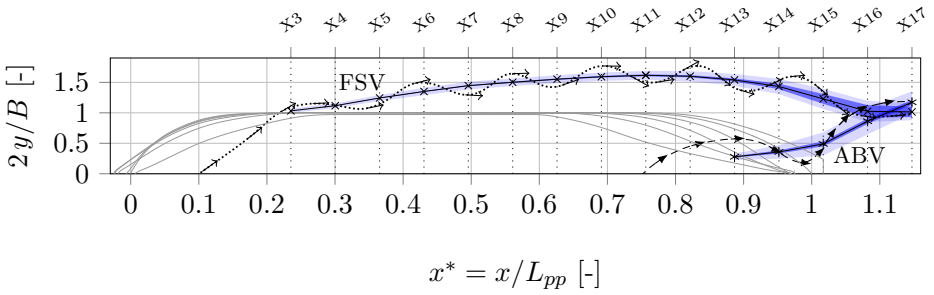

(a) Waterplanes. Scale 1.0 for all curves. For legend see subfigure below. Measuring planes labelled on top from X3 to X17.

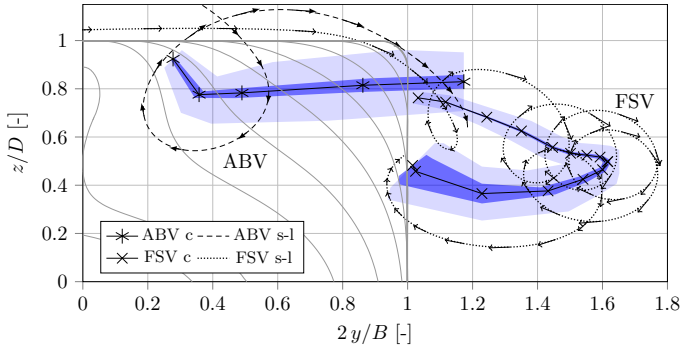

(b) Rear frame planes (for 20th subdivision). Core radius and wandering amplitude scaled by 0.5 for better view. The frame X3 where the initial FSV separation occurs is located upstream of the midship. 'c' stands for centre, 's-l' for streamline.

Figure 5.5.: Hull body plan with FSV and ABV centre location, core radius (light blue) and wandering amplitude (dark blue). Exemplary streamlines with arrows representing velocity.

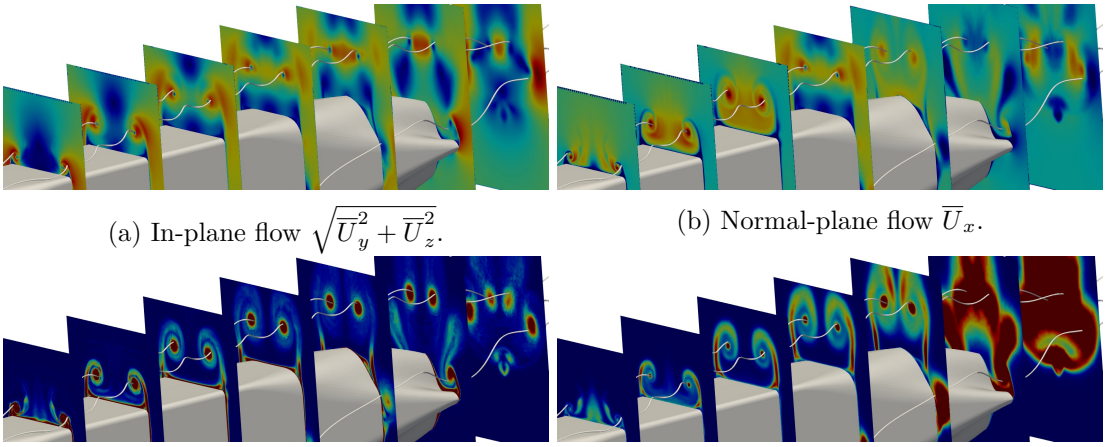

(a) In-plane flow $\sqrt{\overline{U}_y^2 + \overline{U}_z^2}$.

(b) Normal-plane flow $\overline{U}_x$.

(c) Vorticity magnitude $\overline{|\boldsymbol{\omega}|}$.

(d) Resolved TKE k_r.

Figure 5.6.: Time-averaged flow in every second measuring plane from X4 to X16. Exemplary streamlines around FSV and ABV are shown, medium mesh for double-body case.

further downstream the circumferential variation increases with a peak in-between the 'left' and 'right' FSV. This deviation from an ideal q-vortex presented in Eq. 2.2 results from the proximity to the separation and the strong free-shear layer wrapping around the vortex. Around the ABV, the variation of the swirling flow is high, a probable reason the proximity to the strong separation. Within the first three planes the velocity deficit of the free-shear layer is clearly visible and also the distinct maximum inside the vortex core, a jet-like flow with a surplus of up to 40%, see Fig. 5.30. There is no significant deviation from the inflow velocity in the ABV core.

The vorticity represents the FSV and ABV cores as well as the free-shear layers that link both vortices in the stern region in an S-shape pattern, similar to the observations in Devenport, Vogel et al. (1999), see also Sec. 2.2.4. Other vortices like the ASV and the SV are also clearly visible. So is the formation of the resolved turbulence that represents the separating boundary layer rolling up into the FSV cores, the ASV core and the mixing zone around the stern where resolved velocity fluctuations occur in a larger area. All in all the FSV roll-up drives the wake pattern up to little downstream of the rear shoulder where the flow becomes more anisotropic and less homogeneous. In addition, the coexistence of local in-plane maxima of TKE and vorticity is clearly visible. Further visualisations can be found in Sec. B.5.

Vortex Breakdown Downstream of the rear shoulder the FSV core flow reveals a vortex breakdown. Many flow parameters indicate this change which basically is a conversion from an ordered to a disordered state that goes along with a reduction of the vortex

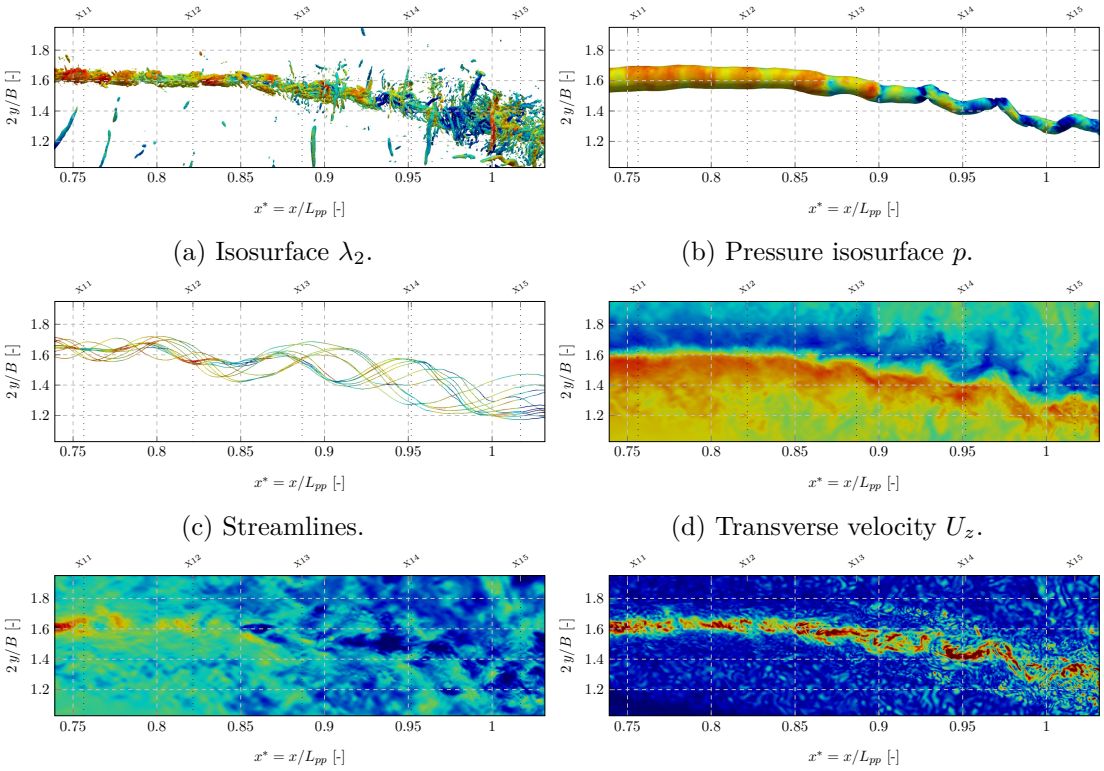

(a) Isosurface λ_2.

(b) Pressure isosurface p.

(c) Streamlines.

(d) Transverse velocity U_z.

(e) Axial velocity U_x.

(f) Vorticity magnitude $|\boldsymbol{\omega}|$.

Figure 5.7.: Visualisation of possible vortex breakdown of FSV. Instantaneous flow fields coloured with jet-colour map. Isosurfaces and streamlines coloured by velocity magnitude 0.6 to 1.6 U_∞.

strength.[4] Figure 5.7 provides a visual impression of the so-called vortex breakdown that occurs around X13. The isosurfaces of vortex strength λ_2 and pressure p reveal bulbs and contractions, as well as a breakup into smaller eddies. Streamlines represent the widening of the core. And the velocity magnitude shows a decrease. Sub-figures d-f show a cut through the FSV: The instantaneous swirl velocity shows the emergence of distortions, a sudden decrease of the axial flow occurs and the vorticity peaks change to a broader spatial range. All these observations are in accordance with typical features of a vortex breakdown like in Lucca-Negro, O'Doherty (2001).

As stated above, the FSV can be seen as a leading-edge vortex similar to the ones separating from a delta wing. The latter "is fairly prone to vortex breakdown" as it "merges smoothly into the tip vortex" (Green 1995, p. 463). This is a possible classification of the FSV breakdown. Further analysis is presented below.

[4]However, not all criteria are observed, e.g. there is no distinct backflow. So it is more the described sudden change of the flow pattern that is termed breakdown herein.

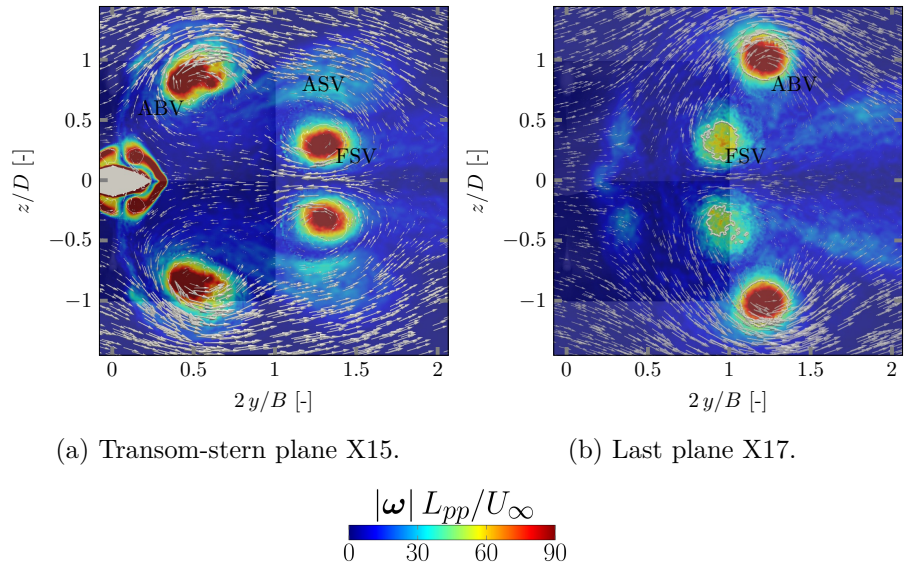

(a) Transom-stern plane X15.

(b) Last plane X17.

Figure 5.8.: Vortex interaction between ABV, ASV and FSV from a single hull and between both FSV, medium mesh for double-hull (s14g2). Arrows represent in-plane velocity, colour map below.

Interactions of trailing vortices Figure 5.8 shows the interaction of the vortex system in the wake with the time-averaged velocity and vorticity field. Both FSV and ABV are clearly visible whereas ASV is nearly diffused. The vertical shear layer shed from the stern is still present at X15. For each hull FSV and ABV are co-rotating so both FSV are counter-rotating. As the in-plane velocity shows, the outer flow bends around the whole vortex system with a peak velocity close to the ABV and a large backflow in-between both FSV due to the reinforcing counter-rotation. In-between the FSV and ABV the velocity drops to nearly zero, a consequence of the co-rotation. Downstream of the whole vortex system and upstream of it in X17 there is a stagnation point with zero in-plane velocity.

Due to the co-rotating swirl, FSV and ABV attract each other, indicating the merging process (Devenport, Vogel et al. 1999, p. 360). This attraction acts more on the swirling velocity field than on the vorticity which is represented by the difference of the swirling flow centre and the vorticity centre. An effect also revealed in Fig. 5.29: downstream of X14 the corresponding time-averaged centres do not coincide.

Vortex Profiles A line along the y-axis through the FSV and ABV centre - the swirling centre - is used to show the time-averaged tangential and axial velocity profiles and the vorticity and turbulence distribution in Fig.s 5.9 and 5.10. For the FSV, there is a two-layered structure visible clearly at X4 and X5 that represents the close free-shear layer. Further downstream, the distance between its outer spiral and the vortex centre increases

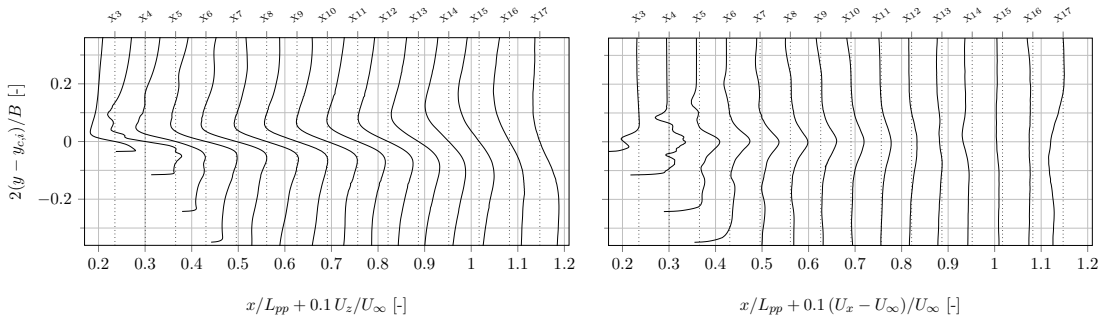

(a) Swirling velocity $\overline{U}_z$ and axial velocity $\overline{U}_x$.

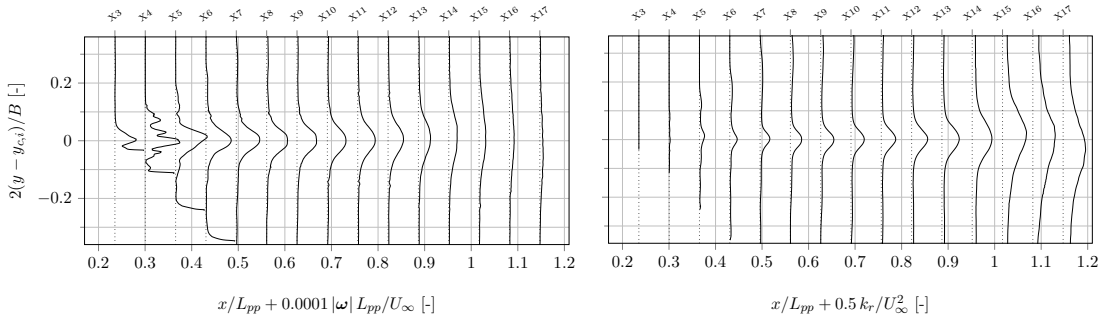

(b) Vorticity magnitude $|\overline{\boldsymbol{\omega}}|$ and resolved TKE k_r.

Figure 5.9.: Profiles along a line parallel to the y-axis through FSV swirling flow centre at all measuring planes X3 to X17 corrected for the individual position $y_{c,i}$.

and the profiles show a typical vortex pattern like for a q-vortex, see Eq. 2.2.[5] At the very last plane X17 the profile does not resemble a typical vortex one. After leaving the boundary layer region, the FSV axial velocity becomes jet-like with a distinct surplus at the centre. This overshoot decreases with downstream distance and finally reverses to a small velocity deficit downstream of the breakdown location. The vorticity distribution represents the vortex core and the free-shear layer spiral. According to the diffusion of the time-averaged vortex, the peak becomes wider. Turbulence peaks at the vortex centre at upstream locations, the peak widens and grows with vortex progression. The vortex breakdown around X13 manifests in a sudden decrease of the vortex strength.

Compared to the FSV, the ABV swirling velocity profile resembles less a q-vortex. The deviation of the axial flow from the inflow is smaller and both vorticity and turbulence are less concentrated to the vortex core. This is a consequence of the strong separation and mixing zone. Summarising, both Fig.s 5.9 and 5.10 provide a quantitative measure for the evolution of the vortices.

[5] As Devenport, Rife et al. (1996, p. 101) show this is not surprising because "any vortex will appear as a q-vortex given sufficient wandering".

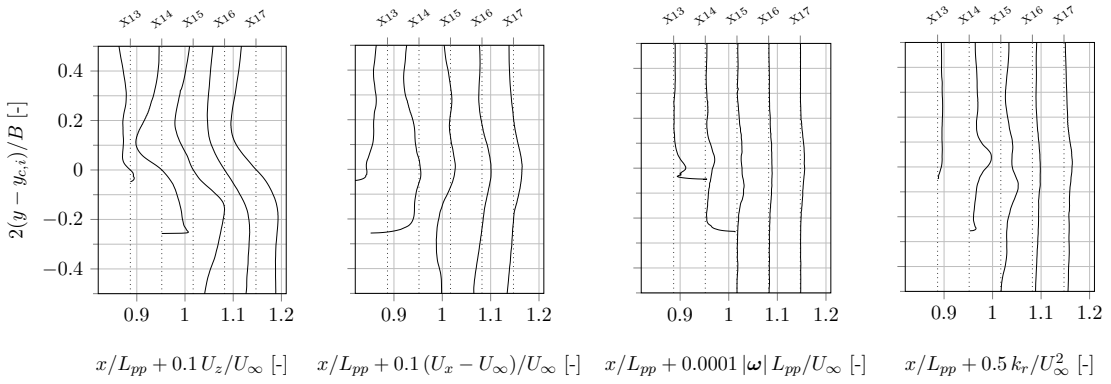

Figure 5.10.: Profiles along a line parallel to the y-axis through ABV swirling flow centre at all measuring planes X3 to X17 corrected for the individual position $y_{c,i}$. From left to right the sub-figures show the swirling $\overline{U}_z$ and axial $\overline{U}_x$ velocity, the vorticity magnitude $|\overline{\boldsymbol{\omega}}|$ and the resolved TKE k_r.

5.2. Verification

The objective of this section is to evaluate the turbulence modelling of the underlying hybrid RANS-LES approach. As grid convergence is no convergence criterion within this approach, the influence of the mesh resolution on the vortex centre flow is analysed only in the appendix, see Sec. B.4. The prediction of hull forces is not as robust and reliable with DES as with RANS, Sagaut et al. (2013, p. 286) e.g. points out that error-cancellation is possible. Besides, hull forces were not measured and this leads to the absence of a consideration of the forces in the present thesis.

Figure 5.11 visualises the absolute and relative portion of the resolved turbulence k_r for the leeward upstream wake. Right after separation, the free-shear layer flow develops resolved turbulence due to large inherent flow instabilities arising from the blunt shape. The grey area is quite small here. However, resolved turbulence around the vortex core develops slower, it is partly entrained from the free-shear layer. The refinement of the whole grid from coarse to fine increases significantly the absolute and relative TKE near the initial separation in the vicinity of the forward shoulder. This is a clear proof of a smaller grey area on finer meshes. For the fine mesh g1 the region surrounding the FSV fulfils the critical requirement of 80% resolved TKE (Pope 2000).

The very right figures show the results for the mesh where only the vortex core region from the coarse mesh is refined by a factor 2. So the core cells are 22% finer compared to the fine mesh g1. As consequence, the absolute TKE is comparable to the coarse mesh and the relative TKE is a little more largely spread. Comparing with the fine mesh reveals the advantage of the refinement in a larger region to obtain a larger degree of resolved TKE in the wake. Another indication for the resolved TKE is presented in Fig. B.14 where the number of eddies depends much more on the overall resolution

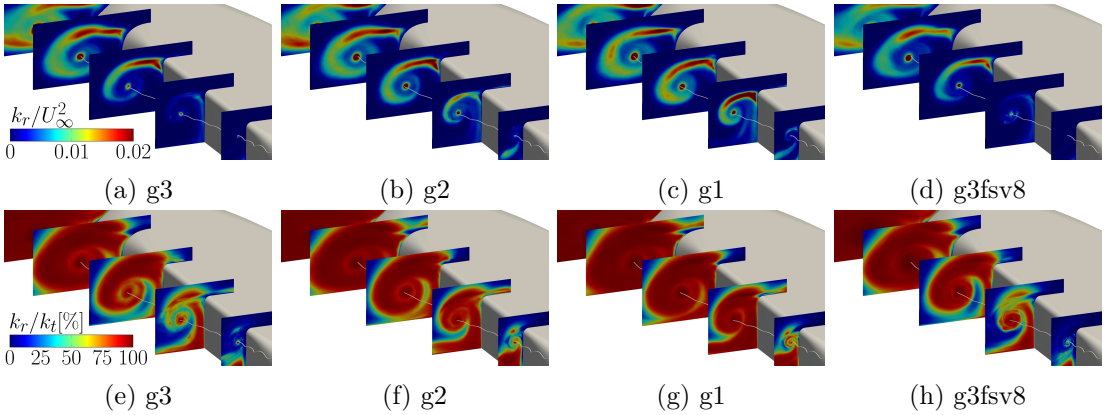

(a) g3 (b) g2 (c) g1 (d) g3fsv8

(e) g3 (f) g2 (g) g1 (h) g3fsv8

Figure 5.11.: Turbulent kinetic energy in the vicinity of the FSV: resolved part scaled to squared inflow velocity (top) and to total TKE $k_t = k_r + k_m$ (bottom). Planes X4, X6, X8, X10, X12 shown and streamlines showing FSV and ABV core from coarse mesh. Subcaptions refer to grid resolution, refer to Tab. 4.2.

and is visually independent of the core grid refinement (g3–g3fsv8). This indicates the importance of a fine mesh to capture turbulence at upstream positions.

In the downstream wake region, the difference of resolved TKE between the coarse and fine grid resolution is visually negligible: see Fig. 5.12. And already on the coarse mesh, the wake turbulence is resolved by more than 95% right outside the boundary layer, see Fig. B.7, so the LES resolution is proper. One observation is that it is most important to resolve the upstream wake with a fine mesh; in downstream regions with developed turbulence a coarser mesh would be sufficient.

Next to the amount of resolved TKE, the convection discretisation is an important aspect: It is blended so that the LES-regions are treated with a minor-diffusive scheme

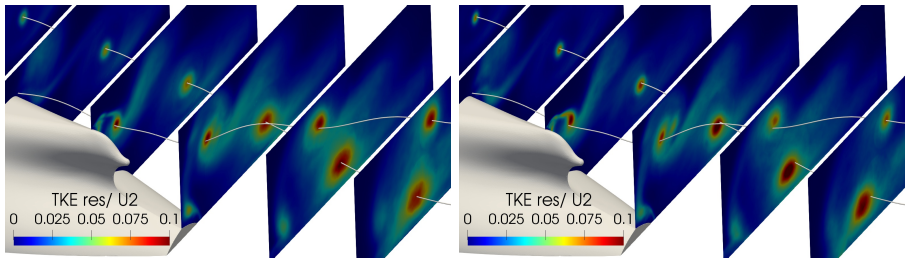

(a) Coarse mesh (g3). (b) Fine mesh (g1).

Figure 5.12.: Resolved turbulent kinetic energy in the stern wake at planes X12, X13, ..., X17 for the coarse and fine mesh. Streamlines showing FSV and ABV core from coarse mesh. Equal colour scale.

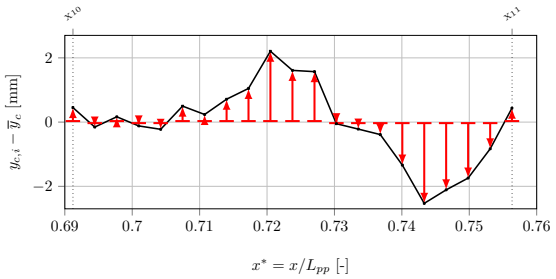

Figure 5.13.: Wandering refers to the in-plane vortex displacement from its mean position, visualised by the red arrows at one time moment between X10 and X11 for the FSV. The axes differ in scale, the maximum angle between the current vortex axis and x is about 12°.

and the RANS-regions are treated with a common stable linear-upwind scheme, see Sec. 4. Figure B.4 visualises the blending coefficient termed 'strelet's blending factor' (SBF) and Fig. B.5 shows the underlying subdivision into a RANS and LES zone.

5.3. Wandering Analysis

An exemplary formation of wandering is visualised in Fig. 5.13 that highlights its definition according to Sec. 2.2.1 for the present application. First, the wandering motion of the vortices is analysed statistically within the present section. Secondly, the wandering-corrected ('w-c') vortex centre flow is investigated in Sec. 5.5. In between, there is a section about the flow in the vicinity of the centre.

The instantaneous displacement of the vortex centre, termed wandering according to Sec. 2.2.1, is tracked using three different representations for the vortex centre[6]:

- centre 1 (c1)[7]: the minimum of the swirling flow inside the $y-z$-plane $\sqrt{U_y^2 + U_z^2}$
- centre 2 (c2): the maximum of the vorticity magnitude
- centre 3 (c3): the minimum of the pressure.

As the FSV and ABV are aligned approximately parallel to the x-axis (see Fig.s 5.17 and B.16), the centres are determined inside the measuring planes X3 to X17. The analysis of wandering as a phenomenon considers the displacement and the angular change of the vortex axis. The latter is represented by the vorticity vector at each centre. Besides, the correlation of the displacement in the x-plane is analysed.

[6] These are rather intuitive descriptions of a vortex centre. A further discussion on different algorithms can be found e.g. in Chakraborty et al. (2005), Jeong, Hussain (1995) and Sujudi, Haimes (1995). The objective here is to use a robust and efficient scheme, because a huge amount of data is considered.

[7] As explained in the following, this is set as default centre.

About 3000 instantaneous snapshots are the basis for the statistical analysis. It is the unfiltered flow field that is used. An approach with less influence of turbulent fluctuations would be the use of reconstructed snapshots from POD analysis. In the present framework, POD analysis is used only to show the low-frequency radial displacement at the centre, see Sec. 5.4. A motivation for the present choice is the coherent structure of the vortex core flow.

Downstream of FSV breakdown the ordered pattern is absent but this also applies for the wandering motion. As the existence of an ordered core flow pattern is a necessary condition for wandering. The opposite is a turbulent vortex where the distinction between the vortex displacement and turbulent fluctuations inside the core is intricate, refer to Sec. 2.2.1 for more details.

Displacement of the Vortices An exemplary formation of the wandering is shown in Fig. 5.14 within X10 and X11 for the FSV. Here, measuring planes have been placed every 5 mm for a higher spatial resolution of the vortex centre line and nine instantaneous vortex core lines are shown that are blanked out correlating to the time passed. Both vortex centre representations 1 and 3 reveal a distinct pattern that evolves in time. However, for centre 2 no distinct centre formation is visible, instead oscillations or 'jumps' of the centre dominate. In relation to the above discussion, it seems reasonable to

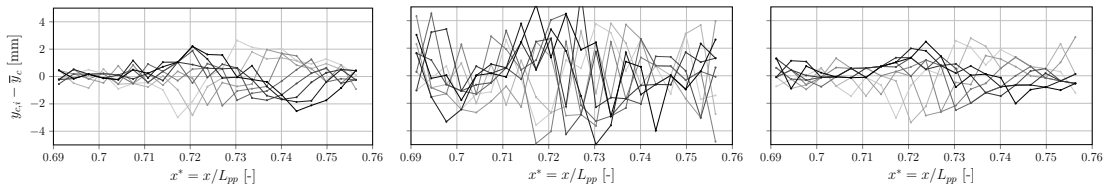

(a) Swirling centre c1. (b) Vorticity centre c2. (c) Pressure centre c3.

Figure 5.14.: Exemplary alignment of FSV centres between X10 and X11 with additional planes. The opacity represents the time passed for the FSV to convect downstream. Remark that the vortex displacement is small compared to e.g. the core radius (see Fig. 5.28a). Every 41th time step was used which corresponds to nearly 0.2 ms.

choose the swirling flow or the pressure as a proper centre representation without low-pass filtering the background velocity field. In contrast, the vorticity maximum reacts more sensitive to small-scale turbulent fluctuations. An explanation is the definition of vorticity with velocity gradients that amplify inhomogeneities of the velocity field. For the future analysis, c1 is taken as default centre representation because this is comparable to the experimental results only as no pressure data is available. For the analysis of the turbulent content, the pressure centre is again considered.

For the analysis of the wandering motion and the wandering-corrected flow many instantaneous centres are analysed statistically. Therefore, it is important to assure the consideration of the same material vortex axis. In opposition, centre 2 reveals points that do not belong to a continuous vortex axis but rather to varying local structures, or in other words: the vortex centre 'jumps'. This renders the analysis questionable, however it will be conducted to show the influence of the 'jumps'.

In terms of a general measure of the wandering motion's amplitude (also termed RMS amplitude[8]) a_w is introduced as the mean of the instantaneous displacements $y_{c,i}$, $z_{c,i}$ from the mean centre $\overline{y}_c$, $\overline{z}_c$ in the $y-z$-plane

$$a_w = \frac{1}{n}\sum_{i=1}^{n}\sqrt{\left(y_{c,i}-\overline{y}_c\right)^2+\left(z_{c,i}-\overline{z}_c\right)^2}. \tag{5.1}$$

For all cases, the wandering motion is analysed inside the $y-z$-plane that is almost perpendicular to the FSV and ABV time-averaged vortex axis, see e.g. Fig.s 5.17 and B.16.

Figure 5.15 reveals the monotonic and approximately linear (see Sec. 2.2.1 or Devenport, Rife et al. (1996)) increase of the FSV wandering amplitude with downstream vortex progression.[9] Centre 1 and 3 differ sparsely. In contrast, the amplitude for centre 2 is larger by about 30 to 50%. This is a statistical representation for the example shown in Fig. 5.14. The dotted curves indicate the standard deviation of the wandering amplitude. This higher statistical moment reveals the same characteristics for the different centres. Scaling the wandering amplitude to the core radius reveals that it is similar to far-field observations and highlights its large influence even in the near field for the present case, see Fig. B.15.

A further analysis of the wandering motion in each $y-z$-plane is based on the covariance matrix of the varying centre $y_{c,i}$ and $z_{c,i}$

$$\boldsymbol{C}_{yz} = \begin{pmatrix} c_{yy} & c_{yz} \\ \cdots & c_{zz} \end{pmatrix} = \frac{1}{n}\begin{pmatrix} \sum_{i=1}^{n}(y_{c,i}-\overline{y}_c)^2 & \sum_{i=1}^{n}(y_{c,i}-\overline{y}_c)\,(z_{c,i}-\overline{z}_c) \\ \cdots & \sum_{i=1}^{n}(z_{c,i}-\overline{z}_c)^2 \end{pmatrix} \tag{5.2}$$

where the diagonal components represent the variance (squared standard deviation) and the off-diagonal components the so-called covariance, and the overline represents the mean value. The matrix $\boldsymbol{C}_{yz}$ is symmetric. Weiss (2019) provides a further analysis of correlation also in relation to POD.

[8] The amplitude is the standard deviation of the in-plane displacement. For consistency with the definition of RMS that is used in the wandering-framework, the denominator is set to the number of samples n and not to $n-1$.

[9] A linear relation is present upstream ob the breakdown location near X13.

The correlation of the vortex displacement in the y- and z-direction is revealed by the correlation coefficient

$$\rho_{yz} = \frac{c_{yz}}{\sqrt{c_{yy}\, c_{zz}}} \tag{5.3}$$

and shown in Fig. 5.15b. Upstream of X5 the wandering motion is very small compared to the grid's cell size (about the same order, so changes by one or two cell spacings only). A coherent wandering motion is assumed further downstream up to about X13 where the vortex breakdown occurs. Herein, the correlation nearly vanishes except at X6 and X10 where the wandering motion is slightly positively correlated.

A further statistical description of the wandering motion in the $y-z$-plane can be obtained by their principal components. The major/ minor one represents the eigenvector of the covariance matrix, Eq. 5.2, with the larger/ smaller eigenvalue. Or in other words, the principal axes characterise the prevalence of the wandering preferences (see e.g. Heyes et al. (2004, p. 14) for a PDF and Devenport, Zsoldos et al. (1997, p. 75) for the principal wandering axes).[10] Weiss (2019) provides a further analysis of correlation also in relation to POD.

Figure 5.15c visualises the principal axes and the standard deviation[11] of the wandering displacement similar to the visualisation of Devenport, Zsoldos et al. (1997, Fig. 2). A nearly isotropic, i.e. uncorrelated (vanishing correlation coefficient), wandering motion is present between X5 and upstream of X13 where the vortex breakdown occurs. Only at X6 and X10 there is a small positive correlation. The probability density function (PDF) of the centre locations would reveal circular isolines. Downstream of the breakdown location, the correlation increases. However, the instantaneous vortex position is driven by turbulent fluctuations and not by wandering.

Figure 5.16 shows the statistics of the wandering motion of the ABV. Like for FSV, a linear trend occurs until X15. Further downstream this trend reverses and the amplitude decreases slightly. The vorticity centre shows the largest scatter from X15 on when the ABV has separated from the hull. The upstream coincidence is triggered by the proximity to the solid hull. Compared to the FSV the amplitude is larger by about a factor two. One possible explanation is the concentration of the strong separation to a shorter region. As the surrounding turbulence is larger (visualised e.g. by more vortical structures in Fig. 5.4c and d), it produces more perturbations that are one driving factor for wandering, see Sec. 2.2.1. Similar to the FSV the correlation inside the x-plane is mostly small, the maximum correlation corresponds to an angle of about 25°. However, the anisotropy represented by the standard deviation along the major and minor axis, is higher. This may also be a consequence of the proximity to the separation that in turn leads to a highly non-uniform distribution of turbulent eddies and so excites an anisotropic wandering motion.

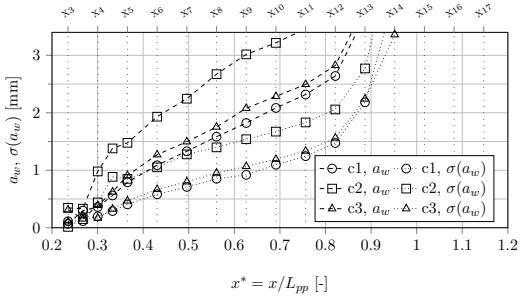

(a) Wandering amplitude a_w, mean and standard deviation.

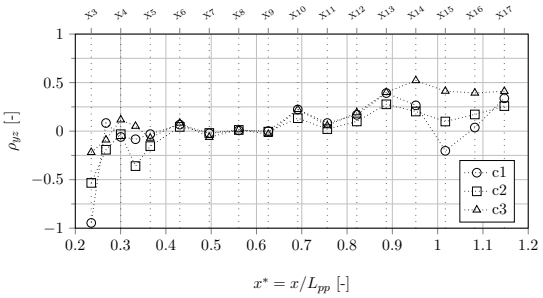

(b) Correlation coefficient of wandering motion in $y-z$-plane.

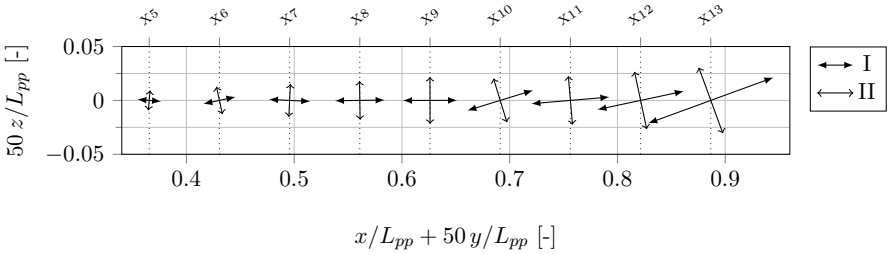

(c) Principal axes and RMS of wandering displacement: major (I) and minor (II) axis (at selected planes only), centre c1. Cartesian axes y and z scaled by factor 50 and equal scaling for ordinate and abscissa.

Figure 5.15.: Wandering characteristics of FSV.

Angle of the Vortices Figure 5.17 depicts the angle between the FSV and ABV axis at the swirling-flow centre ('c1') and the x-axis. For the time-averaged flow, the FSV is well aligned with the x-axis up to plane X13. Considering the instantaneous flow, the FSV deviates on average by a fairly constant angle from the x-axis, about 20°. As shown in Fig. B.16, the average deviation to the y- and z-axis vanishes. However, this observation needs to be further qualified. On the one hand, this angle is influenced by small-scale turbulence, and so may be exaggerated. To better estimate the angle, one could derive it from planes with a very small streamwise distance as intersections between successive swirling centres. And the application of a low-pass filter to the flow would also permit a better analysis of the vortex axis which is explained subsequently. This may be part of future research. On the other hand, some observations support a considerable curvature: Fig. 5.14 shows exemplary that the inclination of the vortex axis may increase 10°. And video analysis reveals that the instantaneous vorticity vectors rotate around the time-averaged vortex axis in a coherent manner.

[10] A well-known scalar measure for the correlation, or anisotropy in other words, is the correlation coefficient which can also be deduced from the mentioned matrix.

[11] According to Eq. 5.1 it corresponds to the RMS of the wandering displacement.

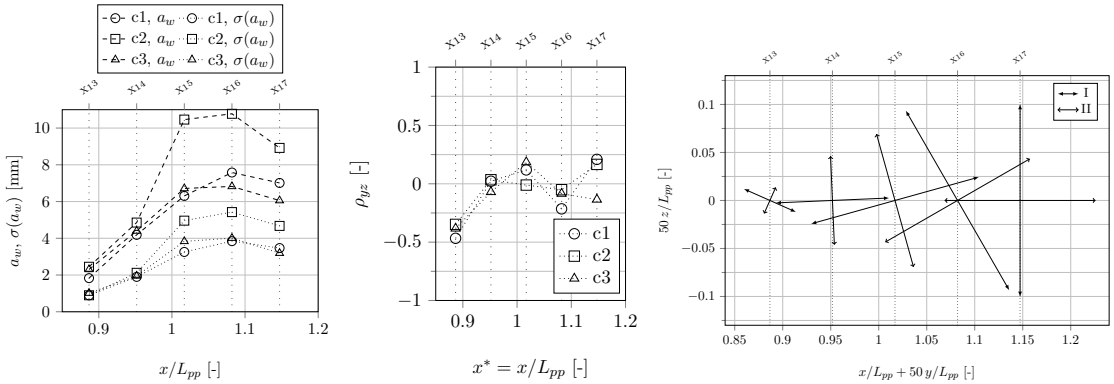

(a) Wandering amplitude. (b) Correlation coef. (c) Principal axes and RMS.

Figure 5.16.: Wandering characteristics of ABV. Subfigure (c) shows the major (I) and minor (II) axis (at selected planes only) in accordance to Fig. 5.15.

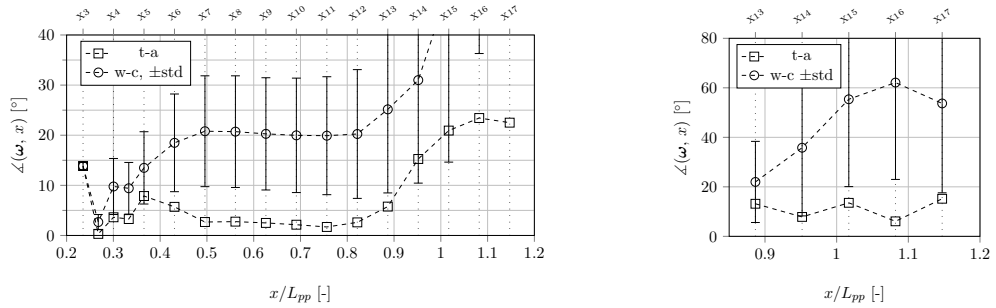

(a) FSV. (b) ABV.

Figure 5.17.: Angle between vortex axis and x-axis for centre c1.

Summarising, the FSV is assumed to follow a rather regular bending around the x-axis between X6 and X12. This indicates a coherent structure that comprises a rotation of the vortex axis.

In contrast, the mean instantaneous angle between the ABV axis and the x-axis linearly increases with progression to a value about three times higher compared to FSV at X12. Taking into account the slight deviation from the x-axis, the ABV axis still tends to vary around the x-axis like the FSV axis does.

And important consequence of the axis variation is related to the evaluation of the instantaneous or wandering-corrected vortex profiles (inside planes normal to the instantaneous vortex axis): This is rendered questionable, because the relation between vortex centre and the radial coordinate becomes ambiguous as the planes would intersect. A consequence for the present work is that only the flow at the vortex centre is corrected for the wandering motion, see Sec. 5.5.

A possible consequence of wandering in terms of a bended axis is the self-induced rotation of the vortex. Bailey et al. (2018, Fig. 11) provides a further analysis and a valuable visualisation.

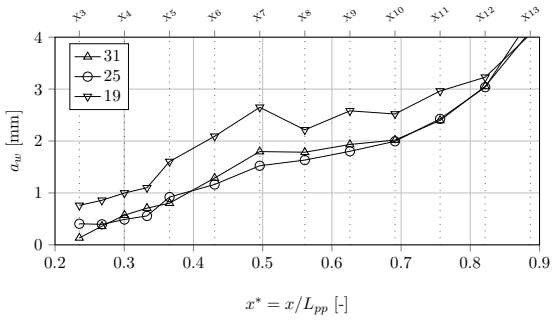

Figure 5.18.: Wandering amplitude for different inflow speed at centre c1.

Influence of Inflow Speed For a varied inflow speed, the wandering amplitude for 25 m/s and 31 m/s nearly coincides. For 19 m/s it is larger by about 70 to 25% between X4 and X10 compared to the default inflow. A correlation to the resolved turbulent content around the FSV is presented in Sec. 5.4. Contrary to the wandering deviation, the vortex axis alignment is almost not affected by a change of the inflow speed, see e.g. Fig. B.17 (this is also valid for the angle to the z- axis).

Influence of Double-Body Model Interactions between the trailing vortex pair usually concerns the far field as Crow or long-wave instability (Crow 1970; Devenport, Zsoldos et al. 1997), see also Sec. 2.2.4. But as the separation between both FSV is short in terms of their core diameter compared to e.g. an airplane it may be present also in the near field here.

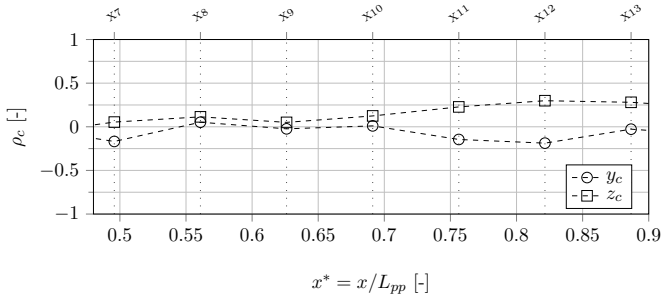

Figure 5.19.: Correlation coefficient of FSV wandering motion for double-body model. It describes the amount of correlation between the vortex displacement of the FSV pair (termed a- and b-vortex from each model side), with respect to the in-plane coordinates y and z.

For the results of the double-body case, Fig. 5.19 shows the interaction between the vortices (FSV) from both sides with respect to the wandering motion. Upstream of X10 the correlation nearly vanishes, downstream the vortices tend to slightly move in the same z-direction and in the opposite y-direction. As the maximum correlation coefficient is around 0.25 only, the wandering motion is mostly independent from the mirror vortex. Its main mechanism is present in the single-body wake field.

Further results on the principal components are provided in Sec. B.6 with the conclusion of a small interaction between the vortices from both sides. For the CFD approach, this supports the simplification of using a single-hull model.

5.4. Vortex Core Flow

The following section discusses the flow in the vortex core region. A qualitative analysis is provided in Sec. 5.1. Herein, two aspects inside the vortex planes are investigated: the stress-strain lag and the first POD mode. In addition, the comparison between different inflow speeds is examined.

Vortex Core Parameters The vortex core parameters of the time-averaged flow[12] are shown in Fig. 5.20. They are evaluated on a line from the swirling centre outward along the y-axis from the analysis of the tangential flow (here: $\overline{U}_z$). It is important to state that these vortex parameters are not unique for both vortices, because of the circumferential variation[13], see Fig.s 5.6a, 5.8, 5.23 and 5.26. However the present line is assumed to be minor influenced by the free-shear layer and other vortices. The vortex circulation is evaluated at twice the core radius r_1 assuming axisymmetric flow $\Gamma = 2\pi\, 2r_1\, \overline{U}_z(2r_1)$. In accordance to Fig. 2.3 this would represent more than 99% of a similar q-vortex.

Another approach to determine the circulation would be of integral character: either from a line integral of the tangential velocity or from a surface integral of the normal vorticity. This entails the problem that the distinction between circulation that is part of the vortex and that is part of the free-shear layer is not trivial. This approach was tested and rejected.

[12] They are evaluated not for the wandering-corrected flow, because vortex planes normal to its axis have a certain degree of ambiguity due to their intersection.

[13] The circulation is independent of the in-plane wandering (Devenport, Rife et al. 1996, p. 75) but depends on the tangential velocity.

Considering the FSV, the core size and the peak swirling flow show a similar pattern: a fast rise, a plateau region with small diffusion influence and a sudden increase/ decrease downstream of the breakdown. The circulation reaches a plateau at about X6 that remains up to about X16, so without influence from the breakdown. The ABV develops on a shorter distance compared to the FSV: the peak tangential velocity develops between X13 and X14. And at the last section, an increase occurs. This is probably due to the interaction with the FSV.

Upstream the FSV breakdown, the wandering amplitude a_w is about 20 to 25% of the core radius r_1. For the ABV the relation it is about a third. In comparison to the results of Devenport, Rife et al. (1996) where it was found to be below 30% this highlights the influence of the wandering motion on the time-averaged flow.

A measure for the stability of a vortex is the swirl parameter q. According to Jacquin, Pantano (2002, p. 162) a vortex with $q > 1.5$ suppresses perturbations with the action of the stabilising swirling flow (see Eq. 2.9).The time-averaged flow would indicate this for both vortices, however the time-averaged flow permits only the determination of an upper limit for the core radius. The peak for the FSV around X13 is due to the vanishing velocity excess. The high q-value is one indication for the relaminarising tendency of the vortex core flow.

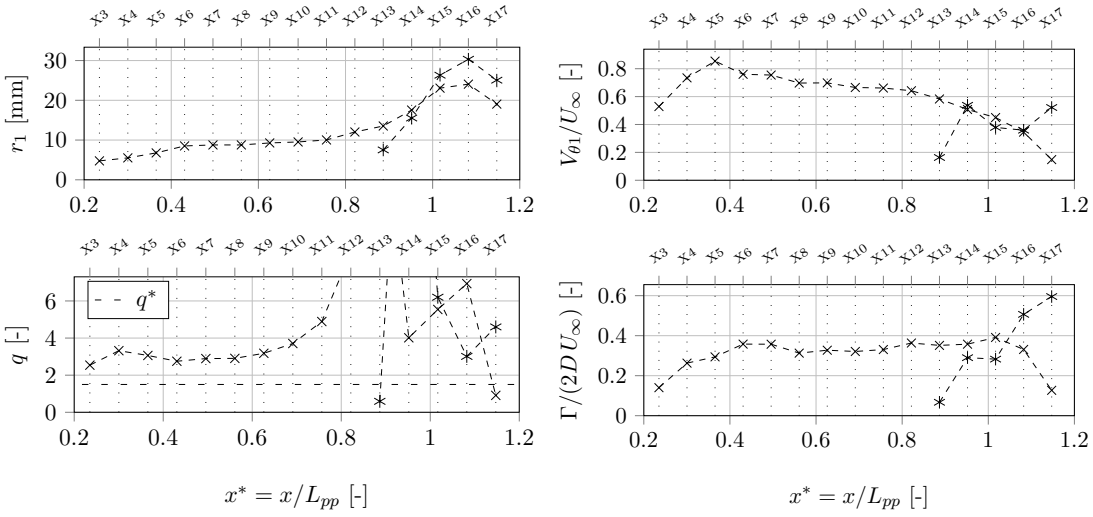

Figure 5.20.: Vortex core parameters r_1, $V_{\theta 1}$ and swirl parameter q as well as vortex circulation Γ for FSV (cross symbol) and ABV (asterisk symbol). Parameters refer to the time-averaged velocity field.

Stress-Strain Patterns In the vicinity of the vortex core, the off-diagonal or shear components of both Reynolds-stress tensor and mean-strain rate tensor, see Eq. 3.12, exhibit a characteristic pattern that has been intensively discussed (Chow et al. 1997b; Jacquin, Fabre, Geffroy et al. 2001). Figures 5.21 and 5.22 visualise these patterns for both FSV and ABV.[14] Besides, the anisotropic normal turbulent stresses are shown. All shear components containing an x-component reveal a so-called two-lobe (2L) pattern and the fields with only in-plane components reveal a so-called four-leaf clover (4LC) pattern. Comparing stress and strain patterns unveils a different angular position of the extrema that is called the 'stress-strain lag' to express that the stress lags the strain.

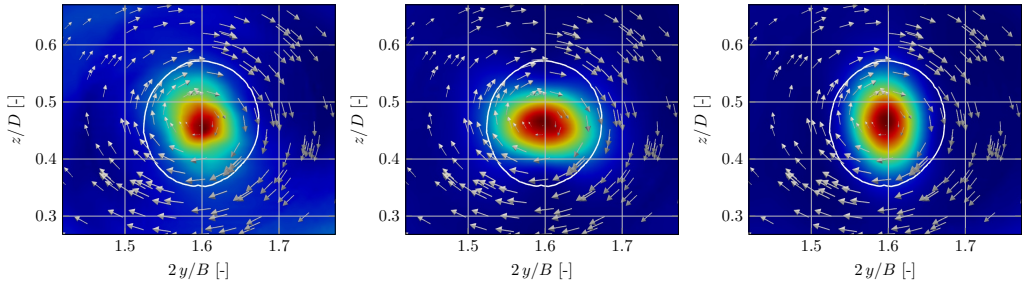

(a) Reynolds normal stresses $\overline{u_x'^2}$, $\overline{u_y'^2}$, $\overline{u_z'^2}$.

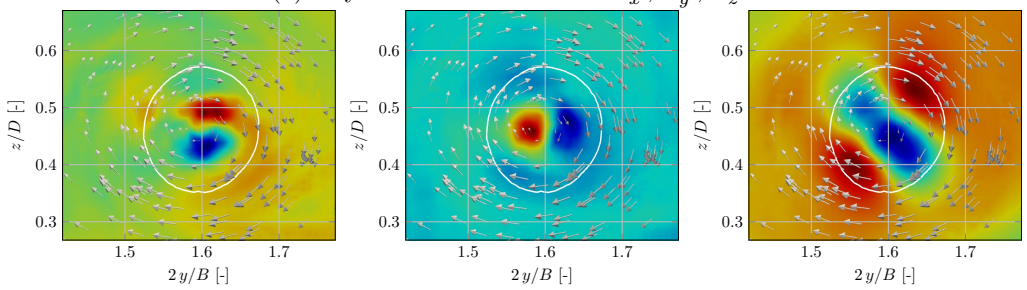

(b) Reynolds shear stresses $\overline{u_x'u_y'}$, $\overline{u_x'u_z'}$, $\overline{u_y'u_z'}$.

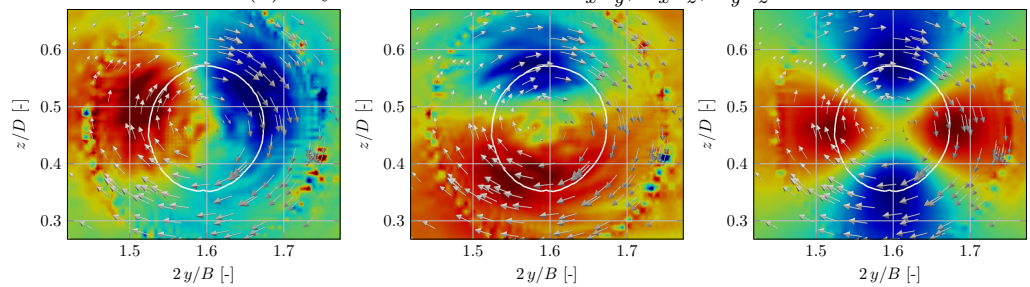

(c) Mean-strain rate $\left(U_{x,y}+U_{y,x}\right)$, $\left(U_{x,z}+U_{z,x}\right)$, $\left(U_{y,z}+U_{z,y}\right)$.

Figure 5.21.: Stress-strain lag around FSV at X12. Arrow length represents in-plane velocity, white isoline represents $\overline{\lambda}_2 = 10^5 \mathrm{s}^{-1}$.

[14] In contrast to Heyes et al. (2004) who compare the time-averaged and wandering-corrected fields, the present analysis is limited to the time-averaged field. According to Sec. 5.3 the unsteadiness of the vortex axis would render the wandering-correction of vortex planes questionable.

Considering the unsteady nature of the core flow, it is important to highlight that the mean strain rate is derived from a time-averaged flow field. In consequence, temporal changes of the vortex - like wandering - cannot be accounted for directly[15]. Or in other words, even a steady q-vortex would reveal a similar pattern. However, the latter example would exhibit the absence of Reynolds stresses. The Reynolds stresses arise from the unsteadiness of the velocity field. A possible contribution may be the wandering motion of a coherent vortex. Figure B.19 provides an example for wandering motion of a q-vortex with the same core parameters and a statistically similar wandering motion (same principal axes and amplitudes) as for the FSV at X12. However, the CFD-predicted 4LC pattern is not ideal which suggests that different influencing factors exist, like a temporal or circumferential variation of the velocity profile. Turbulence inside the vortex core would also contribute to these variations. In relation to the ongoing research on the origin of wandering (Edstrand et al. 2016), a distinct conclusion is out of scope for the present thesis.

For the FSV, the shear strain peaks near the white isoline that represents approximately the vortex core where the swirling velocity peaks too. And the shear stresses peaks inside the vortex core. This observation is in accordance with a wandering q-vortex, see Sec. B.7, and with other experiments (Chow et al. 1997b).

The lag-angle between the stress and strain extrema is 90° for the 2L patterns and 45° for the 4LC pattern. Chow and colleagues compare the Cartesian stress components with cylindrical ones for a r, θ, z-coordinate system at the vortex centre. According to Chow et al. (1997b, pp. 170) the oblique orientation of the 4LC pattern reveals that the in-plane cylindrical stress $\overline{v'_r v'_\theta}$ is much smaller than the in-plane normal cylindrical stress components $\overline{v'^2_r}, \overline{v'^2_\theta}$. The authors provide further detailed conclusions on the core turbulence that follows from the 4LC pattern based on the analysis of turbulence production terms. These findings are also true for the FSV but not further discussed here. They may be important in conjunction with the analysis of turbulence production.

[15] Indirectly, wandering would smear out the gradients.

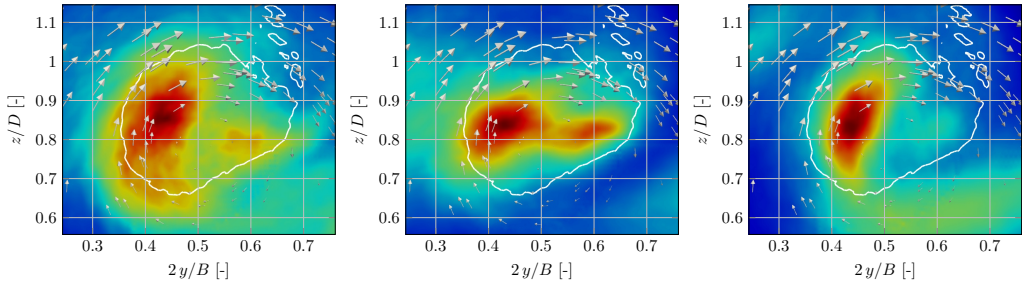

(a) Reynolds normal stresses $\overline{u_x'^2}$, $\overline{u_y'^2}$, $\overline{u_z'^2}$.

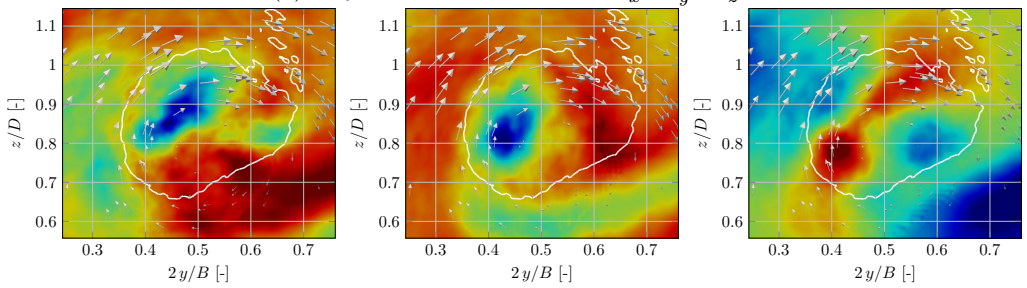

(b) Reynolds shear stresses $\overline{u_x'u_y'}$, $\overline{u_x'u_z'}$, $\overline{u_y'u_z'}$.

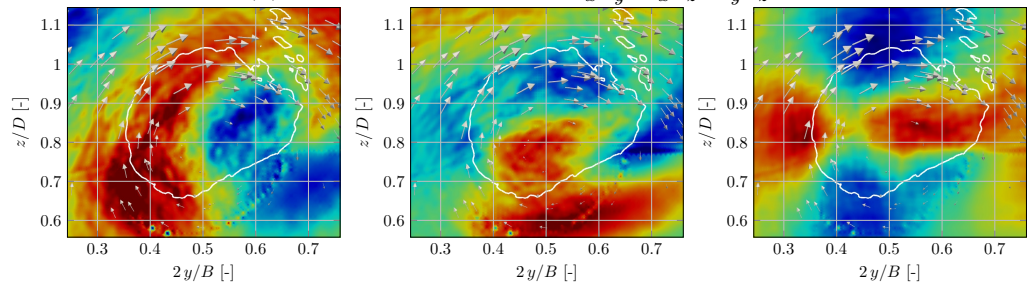

(c) Mean-strain rate $\left(U_{x,y}+U_{y,x}\right)$, $\left(U_{x,z}+U_{z,x}\right)$, $\left(U_{y,z}+U_{z,y}\right)$.

Figure 5.22.: Stress-strain lag around ABV at X15. Arrow length represents in-plane velocity, white isoline represents $\overline{\lambda}_2 = 10^5 \mathrm{s}^{-1}$. Colour scale ('jet') from blue to red.

Figure 5.22 shows the turbulent stress and mean-strain patterns for the ABV at the transom stern plane X15. All contour patterns are less clear compared to the FSV ones. A possible explanation is the proximity to the vortex separation and the resulting strong and close free-shear layer that induces a high degree of anisotropy. Besides, the circumferential variation of the swirling flow is higher and indicates the interaction with the co-rotating FSV, see also Fig. 5.8.

As stated by other authors, e.g. Chow and colleagues, the Reynolds-stress pattern would be equal to the strain pattern for an isotropic eddy-viscosity turbulence model. This includes also curvature-correction extensions that target only on the reduction of turbulent viscosity but still rely on the isotropic Boussinesq approximation. The obvious

difference between both patterns can be accounted for only with anisotropic turbulence modelling or (partly) turbulence resolution.

Chow et al. (1997a, p. 1566) observe the four-leaf clover pattern only downstream of the trailing edge; upstream and close to the wing surface no clear pattern was present but still a variation of the sign. In this case, the CFD results predict it even in the near field. A possible explanation for its clear presence is the distinct separation of the FSV from the hull.

POD Proper orthogonal decomposition (POD) represents a method to extract coherent structures from a set of random fields, an introduction with relation to fluid dynamics can e.g. be found in Berkooz et al. (1993) and Weiss (2019). An application to the separated flow over a wing with detailed explanations can be found in Taira et al. (2017). The resulting "spatial POD modes are a measure of how the velocity is correlated at different points of the flow" (Weiss 2019, p. 17), or in other words reveal regions of interaction that may be linked to coherent structures. The reconstruction of the first most energetic modes corresponds to a low-pass filtering of the velocity field and allows to track possible coherent structures in time. The reconstruction would be a possible application to track the wandering motion free of high-frequency turbulent fluctuations, see e.g. Edstrand et al. (2016), but this is out of scope for the present thesis. Another remark concerns the energy content of different modes that is a measure for their contribution: as there is no distinct spatial region that separates core and shear layer for the FSV and ABV, the mode's energy does not reflect the vortex mode's energy.

Figure 5.23 shows the time-averaged and an exemplary instantaneous formation of the Cartesian velocity components near the FSV core at X12. It reveals the monotonic increase of axial velocity towards the centre and the in-plane swirling flow. The instantaneous axial flow shows a higher degree of inhomogeneity compared to the transverse components that reveal quite well the time-averaged ones and also resemble a typical q-vortex profile.

The last row of the figure shows the first POD mode. Similar to the finding presented in Edstrand et al. (2016, p. 7), the transverse velocity components induce the radial displacement of the vortex - i.e. wandering - as the value at the centre marks a local maximum. The local maximum at the vortex centre indicates that the surrounding free shear layer excites the wandering motion. There is no clear relation between the principal axes of both transverse first POD modes and of the wandering motion shown in Fig. 5.15c. One reason may be the anisotropy of the higher modes.

The downstream evolution of the first POD mode is shown in Fig. 5.24. Similar to previous findings (Edstrand et al. 2016, p. 6) the orientation of the principal axis is nearly constant during vortex evolution and the contour's grow indicates diffusion. So the underlying radial displacement is present in each plane.

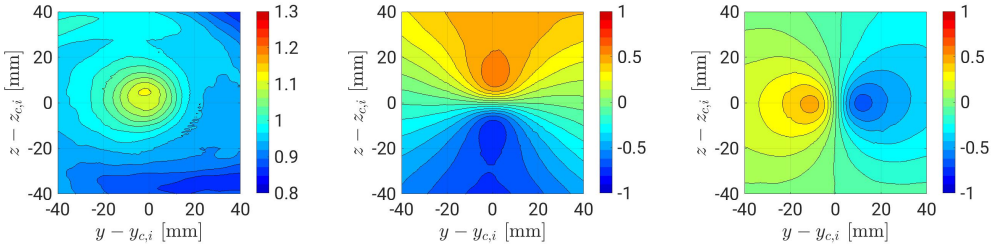

(a) Time-averaged flow: U_x/U_∞, U_y/U_∞, U_z/U_∞.

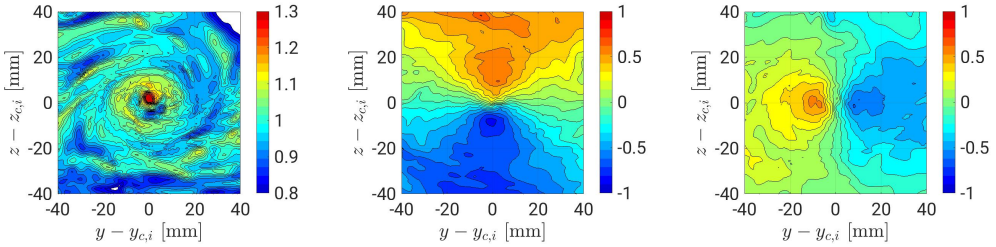

(b) Instantaneous flow: U_x/U_∞, U_y/U_∞, U_z/U_∞.

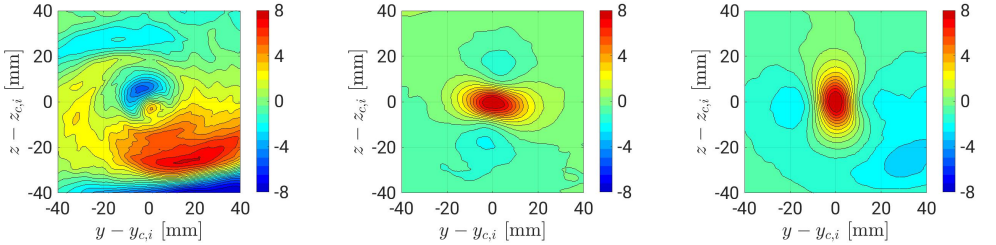

(c) Mode 1: U_x, U_y, U_z in [m/s].

Figure 5.23.: POD analysis of FSV at X12. Colour maps indicate velocity.

Influence of Inflow Speed on Turbulence Evolution For a varied inflow speed only the flow around the FSV is analysed because it reacts more to the change than the ABV, compare Fig.s 5.37 and B.25. Figure 5.25 depicts the vortex system for the varied inflow speed. The shape and location of the vortices is visually unaffected. One consequence is that the core mesh refinement has not to be adapted. However, the number of secondary structures around the FSV, the ABV and the ASV correlates with the inflow. This is a sign for a different level of turbulence. With increasing inflow the relative axial velocity surplus at the upstream FSV increases too, a quantitative analysis follows with Fig. 5.37.

The following qualitative analysis targets to reveal a relation between both the relative axial velocity excess as well as the core turbulence and the inflow speed. Figure 5.26 presents the resolved turbulence and the time-averaged axial velocity[16] for the initial

[16]The axial velocity field is represented by the x-velocity component for simplicity, the difference to the axial velocity is small because the FSV is almost parallel to the x-axis.

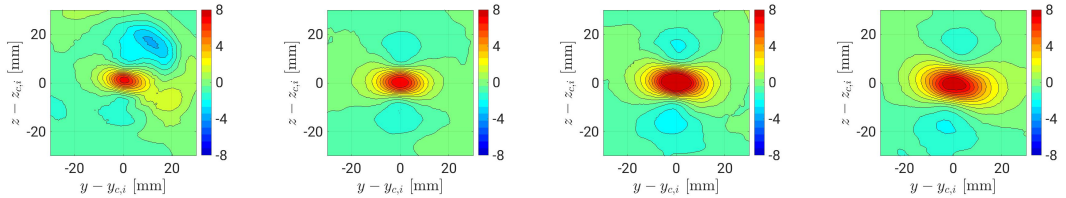

Figure 5.24.: POD analysis of FSV for U_y reveals first mode along vortex progression: X6, X8, X10, X12.

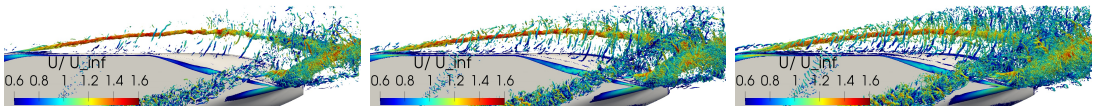

(a) Instantaneous vortices $\overline{\lambda}_2 = 1e5$.

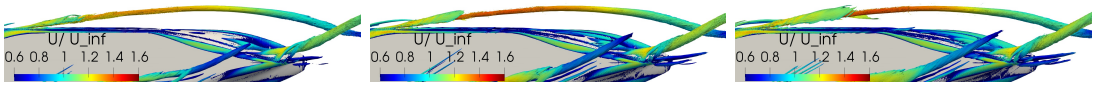

(b) Time-averaged vortices $\lambda_2 = 10^6 \mathrm{s}^{-1}$.

Figure 5.25.: Time-averaged and instantaneous isosurfaces revealing vortical structures for varied inflow speed. Colour map scaled to individual U_∞. From left to right: 19, 25 and 31 m/s inflow speed, medium mesh.

FSV. The resolved TKE is not scaled to U_∞ to show the absolute change, but the axial velocity is scaled to the individual inflow because only the spatial gradients are important in terms of turbulence production. The relative axial velocity and the absolute peak tangential velocity increase with larger inflow.[17] For the latter the circumferential variation also grows. Figure B.6 shows the proper LES resolution for each inflow velocity.

No monotonous behaviour occurs for the resolved core TKE: it minimises for 25 m/s and maximises for 31 m/s. Turbulence seems not to be entrained by the free-shear layer into the vortex but nevertheless grows around the core for 19 and 31 m/s. Hence, TKE arises inside the vortex core. Two production mechanisms - vortex wandering and the spatial gradient of the axial velocity - act against the stabilising effect of the swirling flow:

- The wandering amplitude experiences a small increase from 25 to 31 m/s by maximal 20% around X7, see Fig. 5.18. Comparing 25 and 19 m/s, the amplitude is higher for the smaller inflow between 25 and 70% within X4 and X10. An increasing wandering amplitudes leads to a larger time-averaged TKE in the core (refer to page 83). So wandering is a possible explanation for the high upstream TKE for 31 m/s but not for the difference in TKE between 19 and 25 m/s.

[17] However, the instantaneous axial velocity indicates a similar level of fluctuations, see Fig. B.20. Refer below for a further discussion.

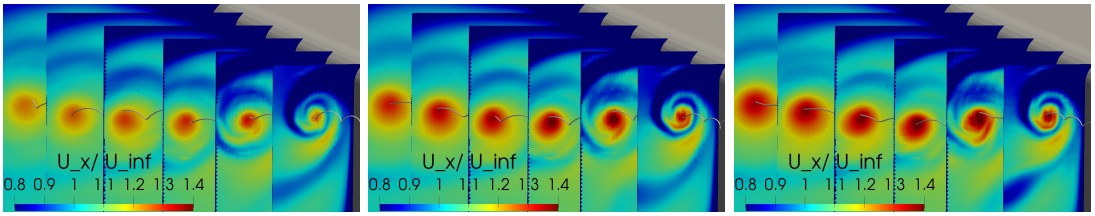

(a) Relative axial velocity U_x/U_∞. The velocity is scaled to the individual inflow speed to reveal the spatial gradient.

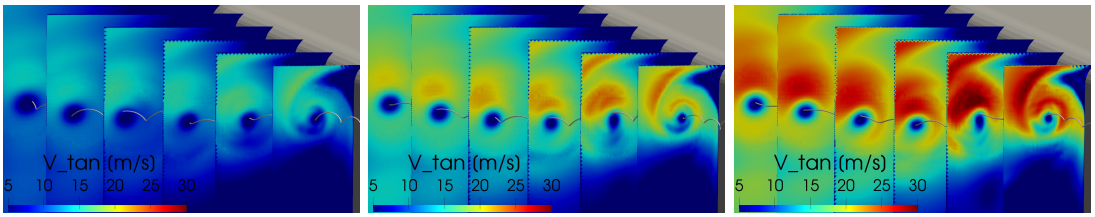

(b) In-plane velocity as absolute values.

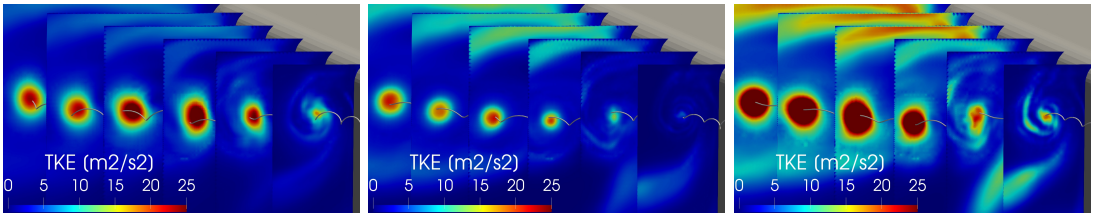

(c) Resolved TKE k_r as absolute values.

Figure 5.26.: Axial and in-plane velocity as well as resolved turbulence around initial FSV with planes X4, X5, ..., X9 for different inflow speeds. From left to right: 19, 25 and 31 m/s inflow speed, the streamlines pass the vortex centre at X4.

- The spatial gradient of the relative axial velocity is smallest for 19 m/s and for 25 and 31 m/s it is comparable. This effect would reduce the turbulence production for the slow inflow.
- The rigid-body like swirling flow imposes a trend towards relaminarisation, see Sec. 2.2.2. Here, both the peak swirling flow and the angular non-uniformity reveal a positive correlation with the inflow speed. This effect would reduce the emergence of core turbulence.

For a further analysis, the turbulence production is shown inside the plane through the FSV in Fig. 5.27. In terms of the TKE budget equation it describes the emergence of turbulence from shear inside the averaged flow field. According to Le et al. (1997) it is the double dot product of the Reynolds-stress and the velocity gradient tensor

$$P^* = -\overline{u_i' u_j'} \frac{\partial \overline{U}_i}{\partial x_j} \frac{1}{U_{25}^3} \tag{5.4}$$

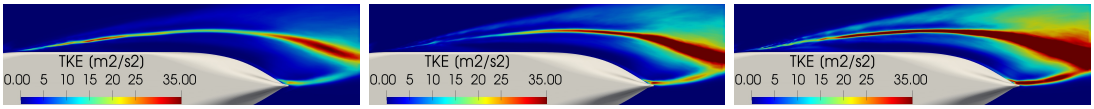

(a) Resolved TKE k_r.

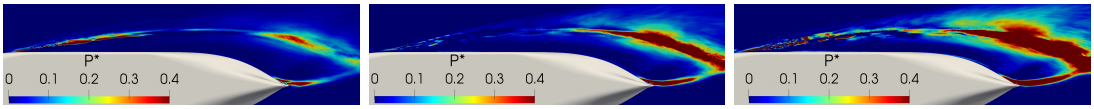

(b) Turbulence production P^*.

Figure 5.27.: Turbulence and its production in a plane through the FSV. From left to right: 19, 25 and 31 m/s inflow speed. The corresponding flow is shown in Fig. B.20.

and here scaled to the third power of the default inflow speed[18]. In each case the turbulence production has a distinct peak downstream of the vortex breakdown that grows with increasing inflow. For the slow inflow, there is a second production region around the initial FSV. This one is not present for 25 m/s and shows a scattered pattern for 31 m/s. This correlates with the low TKE level for 25 m/s.

All in all, the qualitative results presented allow no distinct conclusion on the evolution of upstream TKE which is smallest for 25 m/s and largest for 31 m/s. A further investigation with a quantification of each effect's influence would be necessary to reveal the relation between core TKE and inflow speed. One possible approach would be to apply the analysis of turbulence production inside a Cartesian and cylindrical coordinate system like in Chow et al. (1997b, pp. 169). This would also consider the axial velocity fluctuations that seem to be high for all speeds, see Fig. B.20.

Correlation between Inflow Speed and Vortex Circulation In accordance with Anderson, Lawton (2001) the correlation between the relative axial velocity and the circulation parameter for the FSV is investigated. Anderson et al. found a linear relationship between the inflow and the relative axial centre flow, see Sec. 2.2.3. Speaking generally, taking the vortex circulation as a measure comprises firstly the advantage that its value is insensitive of wandering (Devenport, Rife et al. 1996, p. 75). Secondly it comprises the disadvantage that the vortex separation cannot be clearly distinguished from an influence of the free-shear layer. Considering the latter aspect, the core parameters are determined for different inflow speeds along the $+y$-axis, because the similarity to a q-vortex is highest, compare Fig.s 5.23 and 5.6. However, the angular non-uniformity is not considered. Figure 5.28 shows the absolute core radius r_1, the relative peak tangential velocity and the circulation parameter according to Anderson, Lawton (2001) for the time-averaged flow.

[18] It is not scaled to the changed inflow, because the absolute level should be compared.

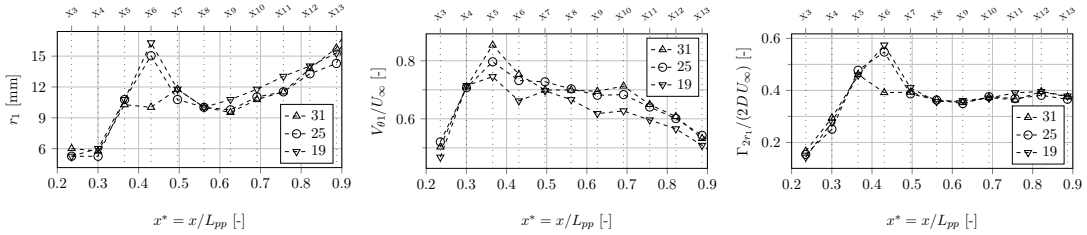

(a) Core radius. (b) Peak tangential velocity. (c) Circulation parameter.

Figure 5.28.: Vortex core parameters for FSV at varied inflow speed. Scaled to individual inflow speed. The data points for 31 m/s at X6 marks an outlier.

The overall influence of the inflow variation on these core parameters is small compared to the inflow change by ± 24%. An inflow of 19 m/s tends to create a larger core radius. This seems plausible as it scales with the thickness of the turbulent boundary[19] that again decreases with increasing speed (see e.g. Wilcox (2006, p. 29) or Schlichting, Gersten (2006, p. 32)). Between the formation of the vortex profile at X7 and the breakdown at about X13 the core size grows linearly with downstream distance. The peak tangential velocity is smallest for 19 m/s and approximately equal for 25 and 31 m/s inflow. With the exception at X6, the difference of the circulation parameter for a varying inflow is negligible (some percent), the absolute estimated vortex circulation scales just with the inflow. And this fact contradicts the findings presented in Anderson, Lawton (2001) where the relative axial centre velocity U_{ax}/U_∞ and the circulation parameter correlate.[20] Refer to page 89 for a final discussion of possible explanations for the present results.

5.5. Vortex Centre Flow

Starting with the analysis of the whole vortex system followed by the vortex core region this section encloses and deals with the flow at the vortex centre from FSV and ABV. Generally, the swirling flow centre representation c1 is chosen, because its progression is more coherent than the vorticity centre and the result is comparable to the experimental data that dismiss the pressure.[21] If the consideration of other representations for the centre reveals important flow details, this is highlighted in the present section, otherwise Sec. B.8 provides further details on the differences between the centre representations.

[19] Arndt (2002, p. 159) reports further information on the specific relation that is not certainly quantified.
[20] Figure 5.37 reveals an increase of the relative velocity excess with increasing inflow speed.
[21] Refer to Sec. 5.3 for a definition.

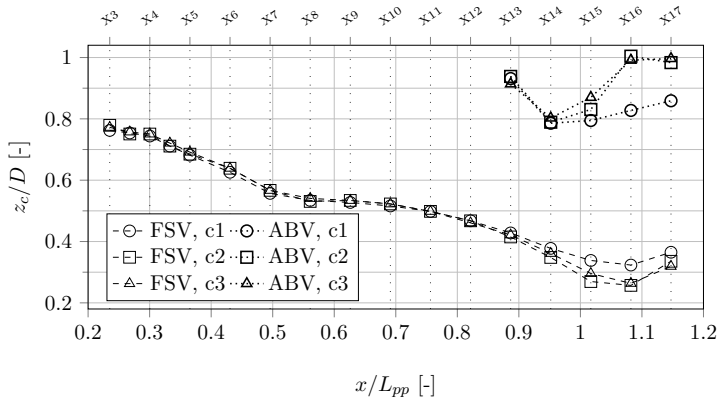

Figure 5.29.: Comparison of FSV and ABV time-averaged centre for different representations along their progression.

Figure 5.29 shows the z-position of the FSV and ABV centre.[22] Up to including plane X14 the different centre representations collapse. Further downstream the swirling flow centre of both FSV and ABV are shifted towards each other in comparison to the vorticity and pressure centre. This can also be observed in Fig. 5.8 and is a consequence of the interaction between the co-rotating vortices. A consequence of the coincidence for the time-averaged centres is that the flow at the different centres is nearly identical too. Consequently, the time-averaged centre flow is shown for the swirling centre only.

Time-averaged and wandering-corrected flow The time-averaged centre flow is evaluated from the corresponding flow field. The wandering-corrected flow is obtained from a statistical analysis of the instantaneous centres, its mean and standard deviation. Previous investigations corrected only for the transverse displacement of the vortex based on a proposition by Heyes et al. (2004). Herein, the instantaneous orientation of the vortex axis is also considered which is represented by the vorticity vector. For scalar variables like the pressure, this is inherently fulfilled. And as the vorticity magnitude and TKE relate to tensor invariants[23] both are invariant to a rotation and need no correction. The only correction applied is for the axial velocity which is parallel to the axis by definition.[24]

At the **FSV** centre the initial increase of axial velocity, vorticity and the decrease of pressure happens within a short distance, between X3 and X4. Both pressure and velocity remain almost constant between the sections X5 and X10. However, the vorticity

[22] Here, the time-averaged flow was used but the mean of the wandering-corrected flow is virtually the same. Slight deviations occur downstream of plane X15 that arise from a very unsteady flow. The mean of the instananeous vortex centre positions can be found in Fig. 5.5.

[23] The magnitude of a 1st order tensor and the trace of a 2nd order tensor respectively.

[24] The main conclusion of the instantaneous axis orientation indeed is the fact that instantaneous vortex planes may intersect and so become ambiguous.

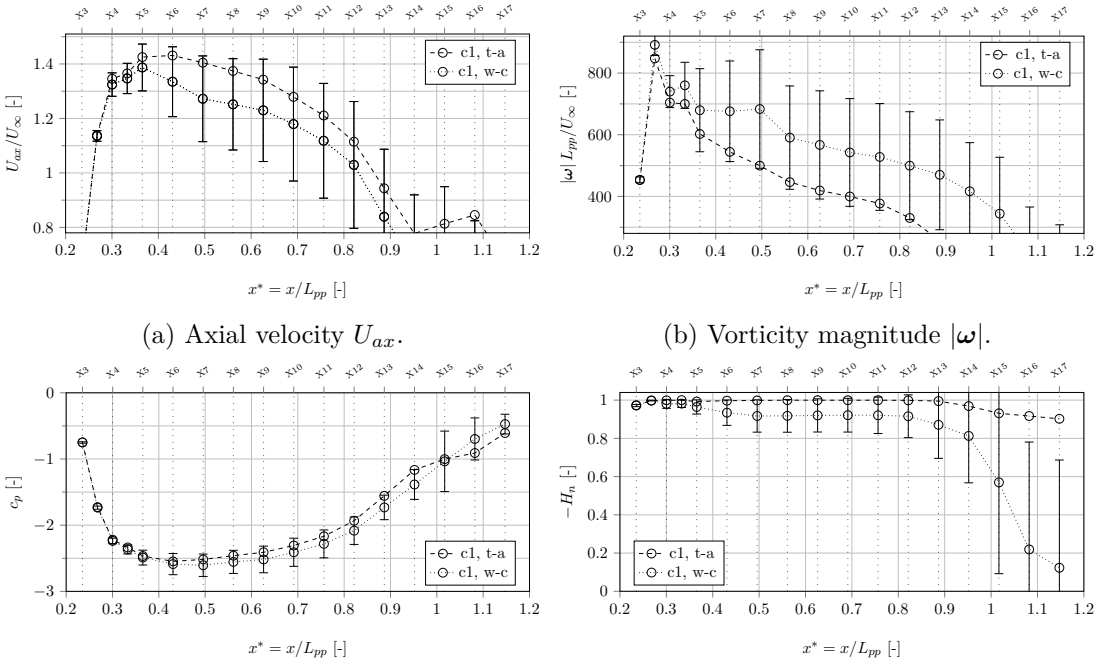

(a) Axial velocity U_{ax}.

(b) Vorticity magnitude $|\boldsymbol{\omega}|$.

(c) Pressure coefficient c_p.

(d) Helicity normalised Hn.

Figure 5.30.: Time-averaged (t-a) and wandering-corrected (w-c) flow at the FSV swirling centre c1.

shows a large peak followed by an abrupt decrease. As the wandering motion smooths out the high core flow gradients (Devenport, Rife et al. 1996, pp. 74), the corrected vorticity is higher by about 15 to 60% between X5 and X13. Upstream the difference is small which correlates with the vanishing wandering amplitude, see Fig. 5.30. The inversion of the smoothing for the pressure is small. This is in accordance with the different spatial extend of the vorticity and pressure peak shown in Fig. B.22.

Applying wandering-correction to the axial velocity U_{ax} leads to a decrease by fewer than 10%. This effect occurs less strong for the x-velocity component U_x and the magnitude $|\boldsymbol{U}|$, see Fig. B.21. An explanation is the unsteady nature of the vortex axis, see Fig.s 5.17 and B.16, that reduces the axial component U_{ax} of a bulk velocity in x-direction.

It seems that the fluctuations of U_x inside the vortex core are generally less homogeneous compared to the transverse or swirling velocity, see Fig.s 5.23 and B.20. These fluctuations seem chaotic and so would not follow the wandering motion of the swirling flow centre. Hence wandering-correction cannot reveal a coherent pattern that is absent. All in all, there are more random fluctuations of the axial flow compared to the transverse flow but these are not related to wandering and not tracked explicitly (instead the vortex centre is tracked). In this case, the temporal average leads to a slight increase of the axial flow.

The helicity in subfigure 5.30d reveals the alignment of velocity and vorticity upstream of X13. For the wandering-corrected flow, there is a small constant mean deviation. At vortex breakdown, the helicity experiences a sudden decrease: by about 10% for the time-averaged flow and far more for the wandering-corrected flow. This is the best indication for the breakdown. It represents the emergence of a highly mixed core flow.

Turbulence at the vortex centre is a delicate topic, because it is hard to distinguish from a coherent wandering motion. Considering wandering-correction and the Reynolds-stress components it is important to state the following relation: at the swirling flow centre (c1), the transverse velocity components become zero.[25] Thus the fluctuations u_i' and the corresponding Reynolds-stress components vanish. Hence, it follows from the centre definition that the wandering-corrected stress components containing at least one transverse velocity vanish. Only the normal axial stress component $\overline{u_x'^2}$ remains. This leads to a strong reduction of the TKE level compared to the time-averaged analysis.[26] In contrast to the swirling flow centre, the other centres would reveal larger fluctuations. This trivial relation is visualised in Fig. B.29. It is important to highlight that the stress components are corrected only for the in-plane displacement and not for the bending of the axis. However, as TKE is a tensor invariant, it is independent of the axes alignment.

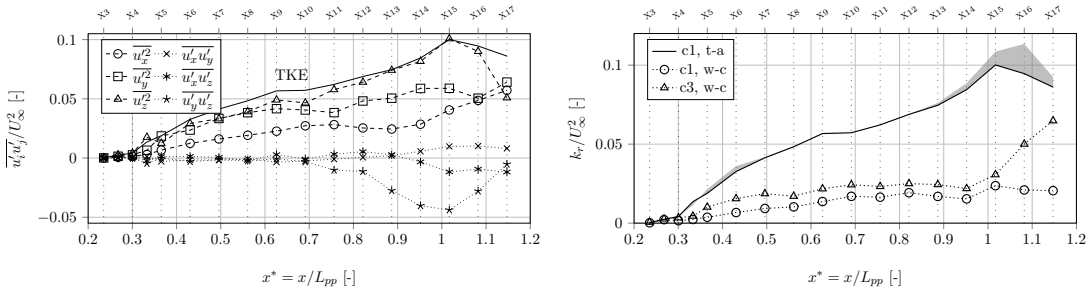

(a) All Reynolds-stress components at time-averaged swirling centre c1.

(b) Time-averaged and wandering-corrected TKE (grey region represents variation of t-a value at c1 and c3) at swirling (c1) and pressure (c3) centre.

Figure 5.31.: Turbulence at the FSV centre.

Figure 5.31a reveals all time-averaged Reynolds stress components and the wandering-corrected TKE at the **FSV** centre. Basically, the turbulent shear stresses (nearly) vanish, except the in-plane component $\overline{u_y'u_z'}$ downstream of the breakdown location. A mostly monotonic increase can be observed for the normal components. The transverse y- and z-components of the normal stresses contribute more to TKE than the axial x-component.

[25] To be precise, the components slightly differ from zero because of the discrete grid representation. But this is negligible as can be seen in Fig. B.29 for c1.

[26] If small-scale turbulent velocity fluctuations exist next to the wandering motion, these will also vanish. An improvement of the present approach would be the application of the wandering correction to a low-pass filtered velocity field.

So the velocity fluctuations inside the vortex plane (normal to its axis) are larger than the ones along the axis. Wandering is a possible explanation: as the mean-flow gradient of the transverse velocities is higher compared to the axial one, it would generate higher velocity fluctuations. In addition, the swirling flow may tend to suppress transverse velocity fluctuations stronger than axial ones.

At the wandering-corrected centre, there is much less turbulence, which is visualised in Fig. 5.31b. As the correction for the swirling centre eliminates not only wandering but also turbulent fluctuations[27], it marks the minimum. At the corrected pressure centre c3, TKE is little larger than at c1 by approximately a constant amount. This supports the observation that the majority of TKE originates from wandering, because the pressure centre does not inherently require vanishing transverse velocity components. The flow at the vortex centre is less turbulent. Due to the evaluation at the centre only, no conclusion about the vicinity is possible, e.g. whether the wandering-corrected TKE marks a maximum or a minimum at the centre in the vortex plane. As it is mostly driven by the axial normal stress component $\overline{u_x'^2}$, this part deserves attention for future investigations.

Referring to the FSV centre flow, Fig. 5.32 shows the same fields for the **ABV**:[28]

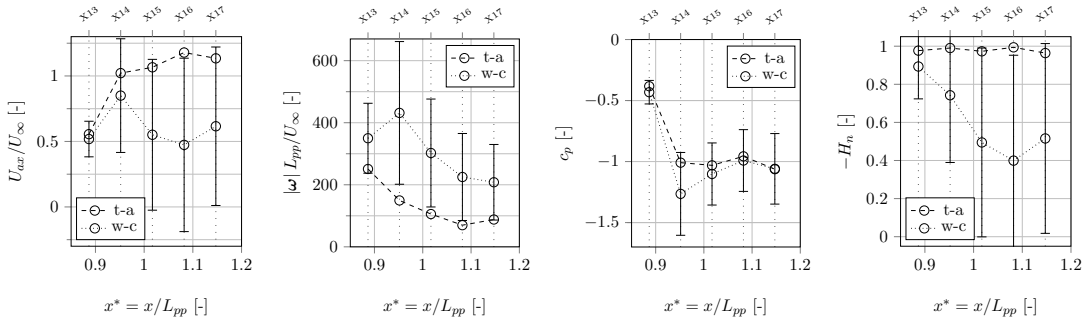

(a) Axial velocity. (b) Vorticity. (c) Pressure. (d) Helicity.

Figure 5.32.: Time-averaged (t-a) and wandering-corrected (w-c) flow at the ABV swirling centre c1.

- The axial velocity differs by a factor of two between its time-averaged and wandering-corrected value: a slight overshoot up to 15% in contrast to a significant velocity deficit of about 50% with a high standard deviation in the order of the mean value. The latter is a consequence of the proximity to the strong separation.

[27] The transverse velocity components are inherently zeroed which follows from the definition of the swirling centre: vanishing in-plane velocity.

[28] The consideration of the other centres is shown in Fig. B.24.

- Wandering smooths the vorticity magnitude up to about a third. Both the mean wandering amplitude a_w, compare Fig.s 5.15a and 5.16b, and the core radius r_1, see Fig. 5.20, are about three times larger compared to the FSV upstream of the breakdown at X13. On the one side, this correlation would reduce the influence of the high wandering amplitude, on the other hand, the instantaneous velocity field inside this mixing zone is highly non-uniform and anisotropic. This renders simple estimations questionable. A reference to the ideal vortex already indicates the influence of e.g. the axial velocity component on the vorticity magnitude, see Eq.s 2.6 and 2.6.
- After a sharp decrease, the pressure keeps a more or less constant level. Like for the FSV, wandering-correction reveals a lower minimum value or in other words: wandering smooths the pressure gradient.
- A nearly parallel alignment between vorticity and velocity is present in the time-averaged flow. But the instantaneous vortex centre shows a sharp decrease of the initial alignment towards $|Hn| \approx 0.5$ which represents an angle of 60°. This is another indication for the complex nature of the ABV core flow. The occurrence of a breakdown is hard to evaluate, because there is no longer upstream region of ordered alignment. Instead, the initial core turbulence is quite high.

Figure 5.33 shows the evolution of **turbulence** at the **ABV** centre. Similar to the FSV

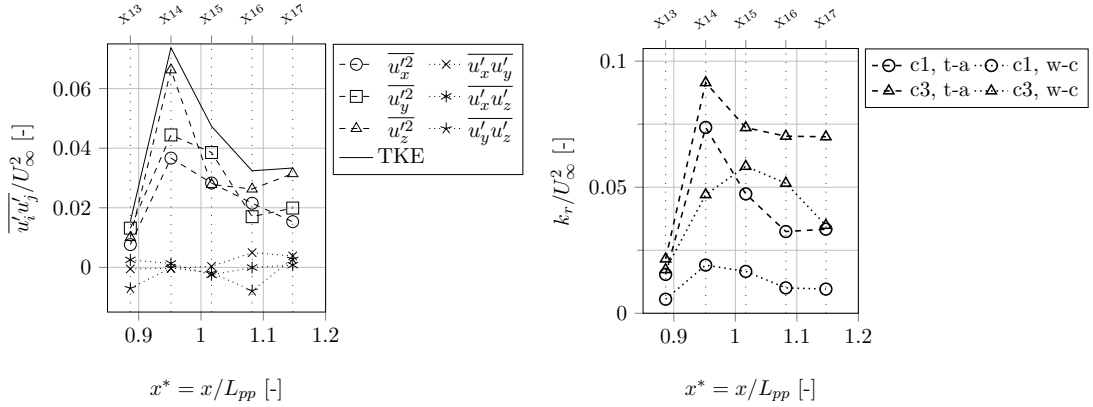

(a) All Reynolds-stress components at time-averaged swirling centre c1.

(b) Time-averaged and wandering-corrected TKE at swirling (c1) and pressure (c3) centre.

Figure 5.33.: Turbulence at the ABV centre.

centre, the shear stresses are very small compared to the normal components. Depending on the downstream distance, the normal components contribute different to the resolved TKE. The latter peaks at X14 with a sharp increase and decrease up- and downstream and the level is comparable to the FSV upstream of the breakdown.

Both the swirling c1 and the pressure centre c3 unveil a reduced wandering-corrected TKE value. This is in accordance with the observations for the FSV. However, the reduction for the pressure centre is small which is an indication for the complex flow.

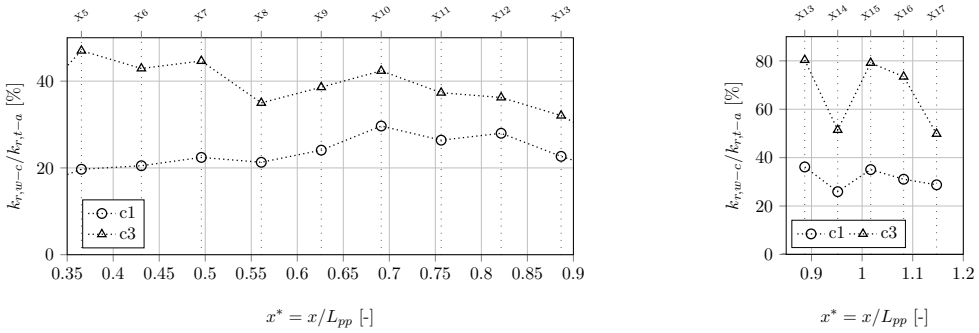

(a) FSV. (b) ABV.

Figure 5.34.: Resolved turbulence at wandering-corrected centre scaled to corresponding value at time-averaged centre.

As a summary, Fig. 5.34 presents the relative portion of (resolved[29]) TKE that stems **not** from wandering. For the **FSV**, this is between 20 and 40%, conversely **about two thirds of TKE originate from wandering**. And this part represents no random[30] velocity fluctuation, but a coherent one: wandering, so it is no turbulence in the proper sense.

For the ABV, the contribution from wandering is smaller: between 20 and 70% compared to two thirds for the FSV. And the difference between the swirling and pressure centre is higher. This correlates with the complexity of the aft wake field where the ABV originates. A further investigation of the turbulent content at the vortex centre is based on the frequency domain.

Power Spectral Density The power spectral density (PSD) is shown in Fig. 5.35. For clear representations at low and high frequencies a moving mean with a small and large range respectively is applied. The spectrum reveals a plateau region up to about $f = 300$ Hz where the inertial sub-range begins and the decrease follows the Kolmogorov spectrum law of $-5/3$. Around 1000 Hz the dissipation regime starts. The difference between the different x-positions is small. Even the FSV breakdown has a negligible influence.

[29]The resolved part covers nearly 100% of total TKE at the centre, compare Sec. 5.2.
[30]Pope (2000, p. 34) discusses the *random* nature of turbulence.

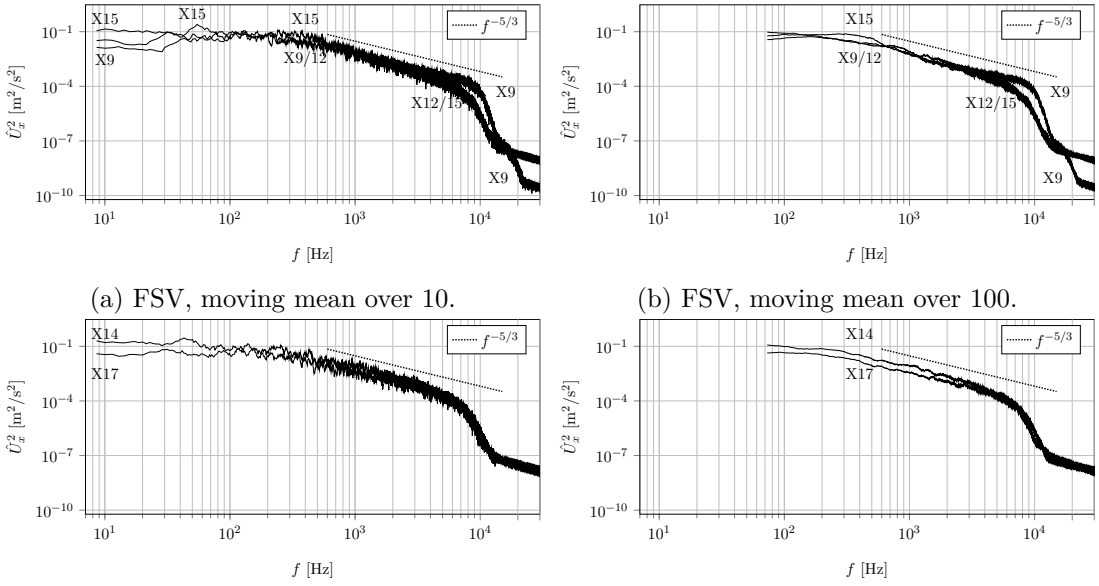

(a) FSV, moving mean over 10.

(b) FSV, moving mean over 100.

(c) ABV, moving mean over 10.

(d) ABV, moving mean over 100.

Figure 5.35.: Power spectral density of U_x at time-averaged centre c1 at different downstream locations indicated by plane number: FSV - X9, X12, X15 and ABV - X14, X17. The spectral lines are smoothed using 10 and 100 samples.

No distinct peaks or an accumulation is present that would indicate wandering. This is consistent with previous experiments (Devenport, Rife et al. 1996; Jacquin, Fabre, Geffroy et al. 2001): the wandering motion covers a broader bandwidth. Additionally, the occurrence of the broad sub-range reveals that the vortex core flow contains turbulence that differs from wandering. And it reveals the proper resolution of the LES model in the core. This is also valid for the varied inflow, see Fig. 5.36b.

Another remark concerns the velocity component used to derive the PSD: differences between the Cartesian ones and the velocity magnitude occur only within the energy-containing range and indicate the existence of the wandering motion occurring at frequencies below about 200 Hz. This is illustrated in Fig. B.32.

Influence of Inflow Speed on Turbulence Evolution The influence of the variation in inflow speed on the resolved TKE is shown in Fig. 5.36. Subfigures a and b depict that for 19 and 25 m/s inflow the TKE level upstream of X10 is comparable, downstream is grows for 25 m/s. For 31 m/s the level is about twice as large. However, upstream of X6 the minimum is observed for 25 m/s. This is in accordance with the observations at the vortex core shown in Fig. 5.26.

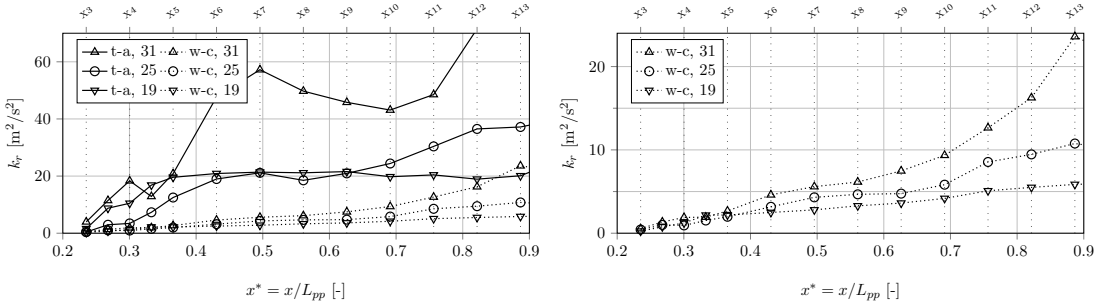

(a) Time-averaged and wandering-corrected streamwise evolution at swirling centre c1.

(b) Wandering-corrected evolution at swirling centre c1.

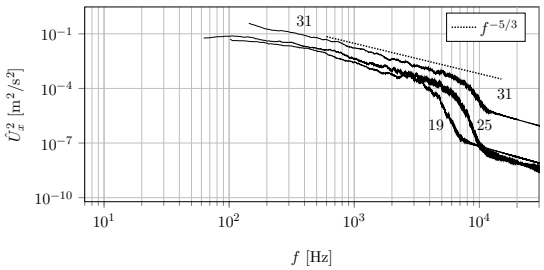

(c) PSD with moving mean over 100 samples at X12.

Figure 5.36.: TKE at the swirling centre c1 for varied inflow speed 19, 25, 31 m/s.

The wandering-corrected TKE reveals a significantly smaller level, a strictly monotonically increasing progression and its order corresponds to the increase of the inflow. The huge reduction for 31 m/s due to wandering correction is in agreement with the large wandering amplitude (Fig. 5.18). Vortex core turbulence evolves within the following counteracting mechanisms: axial velocity gradient and wandering amplitude on the one hand and stabilising swirling flow on the other hand, refer also to page 77. The present results allow no distinct conclusion on the actual manifestation. A further analysis of the TKE budget may clarify this.

The influence of varying inflow speed on the turbulence **spectrum** is shown in Fig. 5.36c. The extent of the intertial sub-range correlates with the inflow speed. And the amplitude shows a little increase from 19 to 25 m/s and a larger one from 25 to 31 m/s within the inertial sub-range. Both effects represent the increase of resolved turbulence for increasing inflow speed after the initial FSV rollup at X12 which is in accordance with the TKE level at X12 shown in subfigures a and b.

Correlation between Inflow Speed and Vortex Circulation Anderson, Lawton (2001) observed a linear relation between the axial velocity and the vortex circulation for different wingtip experiments, see Sec. 2.2.3. For a detailed examination whether this occurs

also for the FSV, Fig. 5.37 depicts the velocity along its progression.[31][32] As the vortex

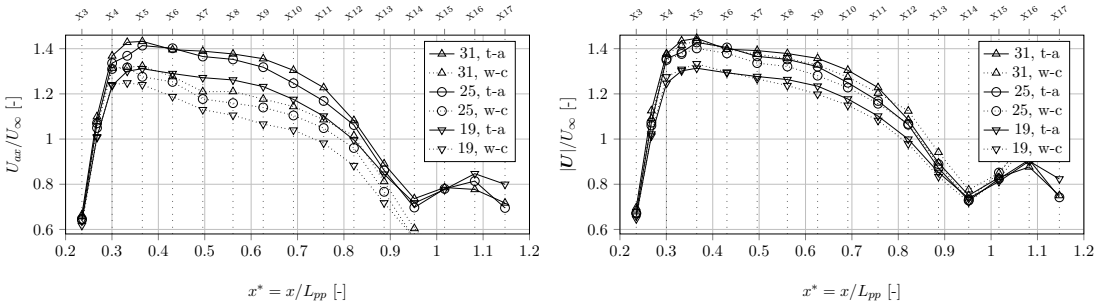

(a) Axial velocity.

(b) Velocity magnitude.

Figure 5.37.: Velocity at FSV's centre (c1) for different inflow speed. All curves are normalised with the individual associated value, e.g. $U_\infty = 19$ m/s for the slow inflow.

axis is susceptible to turbulent fluctuations the velocity magnitude is also shown next to the axial velocity. With increasing inflow both time-averaged and wandering-corrected axial velocities increase, however the difference between 25 and 31 m/s is smaller. In all three cases, the time-average level is higher than the corrected one but the curves' pattern are similar: initially a high gradient followed by a plateau region that tends to decrease further downstream. In relation with Fig. 5.28 it becomes clear that the relative axial velocity excess correlates with the inflow but the circulation parameter does not. Hence, the linear relation observed by Anderson and colleagues is not present here as depicted in Fig. B.27. In the following, possible explanations are discussed.

It is important to highlight the differences between the experiments considered by Anderson, Lawton (2001) and the present case which indicate that the FSV flow is more complex. These can be classified as follows:

- **Aspect ratio:** Anderson analysed lifting wings with aspect ratios between about one and four; the aspect ratio of the double-body KVLCC2 is about 0.13.[33]
- **Distance:** Anderson considered the extended near-field after about one chord downstream of the trailing edge, but the FSV is still next to the body.

[31] As opposed to the FSV that reacts by about 10% of relative velocity excess to the changing inflow speed, the ABV is nearly not altered, see Fig. B.25. So the ABV is not analysed for the inflow-speed variation.

[32] The helicity is affected very little by the change of the inflow, see Fig. B.26. The important consequence is that the variation of the inflow speed has no influence on the position of the FSV breakdown near X13.

[33] The tip shape seems to be not relevant as Anderson also considered blunt wing tips which resemble the full-block hull KVLCC2.

- **Vortex:** the vortex strength differs. Anderson observed 20% wake-like and 80% jet-like axial velocity for a circulation parameter between 0.04 and 0.22, which is around 0.4 for the FSV. Besides, the wingtip vortices have mostly completed the roll-up of the free-shear layer whereas the FSV resembles more a leading-edge vortex: this indicates a difference in terms of accumulated circulation due to vortex filaments.

One consequence from the first and second point is that the wingtip vortices can be roughly classified as axisymmetric flows but the can FSV not, indeed it is an unsteady and inhomogeneous flow. Biot-Savart is a straight explanation for the linear correlation[34] and this effect occurs also for the FSV but in a different setting: possibly the pitch of the helix depends on the inflow. In addition, all three points above indicate that the manifestation of the mechanisms that drive the jet-like flow (momentum deficit, pressure based acceleration) may differ between the wingtip vortices and the FSV. Anderson, Lawton (2001, p. 5) suggested their explanation to be appropriate for the near field which is not the case for the present case.

Influence of Double-Body Model A long-wave or Crow instability occurs for opposite wingtip vortices in the far field. As the aspect ratio is very small, both counter-rotating FSV are quite close: the difference between the centres reduces to five times the core diameter $2\,r_1$ (evaluated perpendicular to the connecting line) upstream of the breakdown and about the core size near X15 and X16. But, similar to the FSV wandering motion, the use of a double-body model has a negligible influence on the single-body FSV centre flow, see Fig. B.28: both the mean values and standard deviations for vortex strength and the helicity coincide. The helicity predicts the same breakdown location, so the interaction between both FSV in terms of long-wave instabilities can be excluded. So the present section is restricted to the single-hull flow.

5.6. Summary of Major Findings

The present section ends with a detailed summary of the major findings. The paragraphs relate to the previous subsections. A comparison between CFD results and wind-tunnel experiments was not possible because the latter were not finally processed at the time of writing. This is essential for validating the observations and conclusions and may be part of future research.

[34] A part of the induced velocities from vortex filaments wrapped on a helix around the vortex is directed along the vortex, see Sec. 2.2.3

Resolution of Turbulence A strong separation and a fine wake mesh is the basis for the fast emergence and resolution of inherent flow instabilities and so a small grey area.[35] However, a fully turbulent stern wake occurs only for 30° inclination (see Fig.s 5.1 and B.2 for both findings). Comparing the initial FSV separation at 12 and 30°, a fast resolution of most of the bulk TKE occurs only for the large drift angle and is significantly improved on the fine mesh. Refining only the core region by a factor of two including its initial separation reveals only a minor improvement (see Fig.s 5.1 and 5.11 for both findings). This motivates the choice of the large drift angle from the modelling perspective.

Wandering Characteristics The swirling and pressure centre reveal a continuous spatial and temporal variation of the vortex displacement, so a 'coherent' pattern (Fig. 5.14). Instead, the vorticity centre is dominated by small-scale fluctuations. Therefore and due to a possible comparison to TPIV data the swirling centre is set as the default one. The amplitude grows linearly until the breakdown for the FSV (Fig. 5.15) and for the ABV there is a linear increase up to a constant level (Fig. 5.16). It is between 20 and 30% of the core radius (compare Fig.s 5.15a and 5.16a with 5.20). This highlights the impact of wandering even in the near field which is usually not the case for wingtip vortices, refer to discussion on page 71. However, Gursul (2005) observed wandering for a leading-edge vortex which has similarities to the FSV.

A nearly isotropic PDF of the FSV in-plane position is present (Fig. 5.15b/c) whereas the ABV reveals a small anisotropy with a small correlation (Fig. 5.16b/c). This seems to be consistent with Devenport's observations, refer to page 20. The vortex angle represented by the vorticity vector deviates by some degree only from the x-axis for the time-averaged flow of both vortices. However, the mean angle of the instantaneous formation is constant by about 20° upstream of the FSV breakdown and increases up to 60° for the ABV (both Fig. 5.17). This represents that wandering consists both of a spatial and angular variation. The latter renders the correction method by Heyes et al. (2004), that considers only the in-plane displacement, questionable. And a curved vortex would be subjected to self-induced rotation (Bailey et al. 2018).

However, this observation needs to be further qualified. On the one hand, the angle of the coherent vortex may be smaller than observed, because the vorticity is influenced by small-scale turbulence. To better estimate the angle, two approaches are presented on page 67 that may be part of future research. On the other hand, some observations support a considerable curvature: Fig. 5.14 shows exemplary that the inclination of the vortex axis may increase 10°. And video analysis reveals that the instantaneous vorticity vectors rotate around the time-averaged vortex axis in a coherent manner.

Summarising, both vortices are assumed to rotate in a coherent way around the mean vortex axis.

[35] For the large drift angle this is also fulfilled on the coarse mesh downstream of the stern region, see Fig. 5.11d, or for the straight inflow around the stern bulb, see e.g. Fig. B.2b.

The application of a low-pass filter on the flow enables not only an improved estimation of the vortex axis but also the separation of the coherent centre from the instantaneous flow centre.The latter is also influenced by small-scale turbulent fluctuations. A low-pass filtering approach, e.g. realised by a reconstruction of the lowest POD modes, would permit the revelation of the coherent centre. An example for a wingtip vortex between one and seven chords downstream can be found in Miloud et al. (2020) with a centre-algorithm based on Graftieaux et al. (2001) and the wandering-correction according to Heyes et al. (2004). This should be applied to both the spatial and angular variation of the vortex axis as the vorticity vector is sensitive to small-scale fluctuations.

Wandering-Corrected Centre Flow As mentioned on page 20 the the correction for the in-plane displacement (Heyes et al. 2004) was frequently used for applications of the far field where a smaller bending would be of negligible influence. Here, vortex planes undergo both translation and rotation due to wandering. This raises the question whether it is possible to correct properly the flow inside the planes for wandering? If axial symmetry of the vortex flow was assumed, this would be possible: the transverse shift of the vortex centre and the alignment of the current axis provide the necessary information to merge instantaneous vortex planes at the same streamwise position. However, if the vortex flow is not axisymmetric and unsteady, this may become questionable: the assignment of the planes would be no longer unique. Therefore only the flow at the vortex centre was corrected for the transverse and angular wandering motion.

The consideration of the individual wandering motion reverses the smoothing of the time-averaged vorticity (between 10 and 100%) and pressure (mostly around 5%) field for both FSV and ABV (Fig.s 5.30 and 5.32). The different representations for the axial velocity of the FSV (U_{ax}, U_x, $|\boldsymbol{U}|$) decrease however and therefore show a higher value for the time-averaged field (Fig. B.21). The extreme decrease for U_{ax} originates probably from the overprediction of the instantaneous vortex axis so that the bulk velocity is projected onto an axis with an exaggerated inclination. The decrease for U_x and $|\boldsymbol{U}|$ is less than 10%; one reason may be that the axial velocity field seems to move not in accordance with the vortex. On average, there exists a maximum at the vortex centre inside the vortex plane but there is no maximum at the instantaneous centre.

Core Flow The vortex flow is highly unsteady and inhomogeneous due to the proximity to the separation. Thus, the FSV and ABV have only very little similarity with an idealised q-vortex, especially the instantaneous but even the time-averaged flow.

Both vortices evolve in a different regime. The FSV separates at the forward shoulder, extends along the parallel midship section and reveals a breakdown-like transition at the after shoulder. Speaking in terms of the hull as a wing, the FSV would be similar to a leading-edge vortex. Near the aft stagnation point where the pressure increases the ABV emerges and immediately leaves the hull but develops surrounded by other vortices and within a strong mixing zone.

The FSV core radius and peak tangential velocity show a low diffusion until the breakdown (Fig. 5.28). Both FSV and ABV consist of a single concentrated core each; however, the flow is unsteady and inhomogeneous. This manifests e.g. in the axial velocity field around the vortex that seems to be uncorrelated with the vortex centre or wandering motion (e.g. Fig. 5.23b).

Similar to previous findings (Edstrand et al. 2016) the first **POD** mode reveals a local maximum of in-plane velocity at the vortex centre (Fig.s 5.23c) that generates a radial vortex displacement appearing as wandering. Thus, there is an interaction (POD visualises spatial correlations) between wandering and the vortex surrounding free shear layer.

Besides, the normal **Reynolds-stresses** are anisotropic and the shear stresses reveal the characteristic two-lobe and four-leaf clover patterns in accordance with the mean-strain rate for both FSV and ABV (Fig.s 5.21 and 5.22). The four-leaf clover pattern can be obtained with a statistically similar wandering motion of an ideal q-vortex. This indicates the contribution of coherent motions to Reynolds-stress components and was shown already in previous studies (Jacquin, Fabre, Geffroy et al. 2001; Zeman 1995).

Centre Turbulence The coexistence of high TKE and vorticity (e.g. Fig. 5.6) at the FSV and ABV core is not a consequence of small-scale vortical structures entrained into the vortex core like for the DTMB/ ONRT case, see Sec. 2.3.2. Instead, both FSV and ABV are coherent vortices subjected to a wandering motion. And this influences the turbulence analysis.

The Reynolds stress tensor components at the wandering-corrected swirling centre vanish if they contain at least one transverse velocity component (Fig. B.29a). This follows inherently from the definition as these components vanish. Only the axial normal Reynolds stress component remains at the wandering-corrected centre and hence TKE is smaller than its time-averaged counterpart.[36] It is important to state that the correction for the swirling centre would inherently correct also for turbulent velocity fluctuations (refer to discussion on page 83).

[36] However, wandering correction shows a small increase of the axial normal stress (compare Fig.s 5.31a and B.29a). This represents the unsteadiness of the axial velocity component where its distribution seems to be not correlated with the swirling flow field.

The correction for the pressure centre (c3) does not cause to vanish turbulent velocity fluctuations inherently like for the swirling centre (c1).[37] Which would be wrong, as there is turbulence: the frequency domain (PSD in Fig.s 5.35 and B.32) reveals nearly isotropic turbulent velocity fluctuations in the inertial sub-range. For the FSV the wandering-corrected TKE for c1 and c3 follows the same trend with a small constant offset only. So the swirling centre prediction for TKE is not a wrong indication (Fig. 5.31). For the ABV, c1 and c3 differ which represents the complex flow separation at the ship stern (Fig. 5.33). Combining these observations, **about two thirds of TKE originate from wandering for the FSV**; for the ABV, the amount is considerably smaller (Fig. 5.34) which represents the flow separation at the ship stern.

There is a strong interaction between the wandering motion (possibly excited by turbulence), the TKE (its time-averaged value contains a significant portion due to wandering), the swirling flow (suppresses disturbances) and the axial flow (spatial gradients produce turbulence) as explained below. The relative axial velocity excess and the peak tangential velocity correlate with the inflow speed. Both counteract in terms of turbulence production. The wandering amplitude peaks for the slow inflow and the wandering-corrected TKE correlates with the inflow. A possible conclusion is that the high wandering amplitude drives the high TKE up to X5 for 19 m/s. But the origin of the high wandering amplitude remains unknown. The evaluation of the complex interactions requires a further analysis that is out of the scope of the present thesis. One approach is the comparison with experiments, and the consideration of the TKE budget terms.

Influence of Inflow Speed on Turbulence Evolution Vortex core turbulence evolves within the following counteracting mechanisms: axial velocity gradient and wandering amplitude on the one hand and stabilising swirling flow on the other hand, refer also to page 77. The present results allow no distinct conclusion on the dominant driving factors and the actual manifestation. A further analysis of the TKE budget may clarify this.

Correlation between Inflow Speed and Vortex Circulation The inflow speed is varied to review whether the linear relation between the circulation parameter (circulation divided by the individual inflow speed) and the axial velocity (deficit or overshoot) presented in Anderson, Lawton (2001) occurs. This is not the case, see also Fig. B.27. Instead, the FSV circulation parameter is nearly insensitive to the variation of the inflow (Fig. 5.28).[38] But the relative axial velocity correlates with the inflow speed (Fig. 5.37). This mismatch indicates that the 'streamwise directed component of downwash' Anderson, Lawton (2001, p. 6) is not visible.

[37] Refer to page 84.

[38] It is assumed that there is no error due to in-plane wandering (Devenport, Rife et al. 1996, p. 75). But the circulation is determined from the tangential velocity along a single line and it is clear that this is not axisymmetric. Refer to page 70 for further details.

One consequence from the first and second point is that the wingtip vortices can be roughly classified as axisymmetric flows but the can FSV not, indeed it is an unsteady and inhomogeneous flow. Biot-Savart is a straight explanation for the linear correlation[39] and this effect occurs also for the FSV but in a different setting: possibly the pitch of the helix depends on the inflow. In addition, all three points above indicate that the manifestation of the mechanisms that drive the jet-like flow (momentum deficit, pressure based acceleration) may differ between the wingtip vortices and the FSV. Anderson, Lawton (2001, p. 5) suggested their explanation to be appropriate for the near field which is not the case for the present case.

A possible conclusion is that the linear relation between circulation and axial velocity manifests only for cases with less flow unsteadiness and inhomogeneity, e.g. wingtip vortices in the far field. Here, the flow is more complex driven by the extremely small aspect ratio, the proximity to the hull; besides the vortex is stronger by at least a factor two compared to the cases Anderson et al. considered. Possibly the pitch of the vortex filaments aligned on a helix changes. However, the difficulties in determining unique vortex circulation for the present case do not allow a distinct conclusion.

Referring to both counteracting mechanisms that drive the manifestation of axial velocity (see Sec. 2.2.3), the relation of the strong FSV swirling and the thin boundary layer (the Reynolds number is smaller than for the wings Anderson considered) are assumed to dominate the jet-like flow.

Instability: Vortex Breakdown? Downstream of the rear shoulder the FSV core flow reveals a transformation to a disordered pattern that is termed breakdown here. The presence and location of this breakdown was insensitive to mesh changes, inflow speed variation (Fig. 5.37) and single- or double-body configuration (Fig. B.28). Although several criteria are fulfilled no typical backflow was observed (refer also page 58). The present results indicate a spiral-type breakdown according to the temporal evolution of the flow pattern. Further studies need to verify the occurrence of this breakdown. This may include its proper classification.

In addition the FSV core is predicted to be stable with respect to disturbances because $q > 1.5$, see Fig. 5.20. Probably the application of this criterion inside the near field for a highly inhomogeneous vortex flow is questionable. This considers also the determination of a representative peak tangential velocity $V_{\theta 1}$.

[39] A part of the induced velocities from vortex filaments wrapped on a helix around the vortex is directed along the vortex, see Sec. 2.2.3

Interaction: Limited Double-body Influence Due to the small aspect ratio of the double-body model both FSV are quite close. However, the interaction between both vortices was found to be minor (in the order of the evaluation accuracy): neither the wandering characteristics (Fig.s 5.19 and B.18) nor the core or centre flow (Fig. B.28) between the single- and double-body FSV shows a difference. So the interaction between the vortex pair is not the dominant mechanism of wandering which may be the case for wingtip vortices in the far field subjected to cooperative instabilities (refer Sec. 2.2.4). Considering CFD approaches, these findings permit the use of a single-hull model for comparisons with double-body model experiments.

Comparison of FSV and ABV The FSV extends next to the model, partly along a constant hull cross section with a small pressure gradient, whereas the ABV separates at the stern where the pressure increases. This may be one explanation for the different velocity excess. Initially the FSV develops independently from another vortex. Around the initial ASV there are existing (FSV, ASV) and emerging (SV) vortices and the TKE level is higher due to the strong stern separation. This is an explanation for the following ABV properties: higher core turbulence, larger wandering amplitude and larger core radius (correlates with the thickness of the separated boundary layer), mismatch between different centre representations (Fig.s 5.8 and 5.29).

6. Conclusions

A detailed summary of the numerical results is presented within the preceding section 5.6. The following summary is of global focus; for references to the results refer to preceding section. At the end, possible approaches for future research are proposed.

6.1. Summary and Discussion

Within aerodynamic investigations of trailing vortices, their dynamic evolution was and is still intensively treated. Compared to a typical wing the very low aspect ratio and the blunt hull shape with multiple separations are the driving factors for the unsteady and inhomogeneous wake field of the present case. Concerning modelling, this enables the proper resolution of turbulence within the separated flow region and so enables the DES approach. The following summary deals firstly with the motion of the vortex itself and secondly with the flow at the vortex centre.

Both FSV and ABV mark coherent vortices subjected to transverse motions. The analysis of spatial flow correlations with POD indicates that wandering is excited by the surrounding free-shear layer. Usually this wandering motion is assumed to be negligible upstream of wings' trailing edges. Here, wandering occurs within the immediate vicinity of the hull and reveals a similar level for the amplitude scaled to the vortex core radius (about a third) similar to the popular far-field testcase presented in Devenport, Rife et al. (1996).

A novelty was the comparison of different vortex centre representations: in-plane swirling flow (c1), vorticity magnitude (c2) and pressure minimum (c3). The first (set as default) and third one reveal a coherent variation whereas the second one is sensitive to small-scale turbulent fluctuations.

Next to the spatial displacement of the instantaneous vortex axis its orientation was considered for the first time. The existence of a high deviation from the time-averaged axis (between about 20 and 40° for FSV and ABV respectively) was observed: there is a significant vortex bending or curvature. As the axis is represented by the vorticity vector here, a part of this deviation may be attributed to its sensitivity which is discussed above, together with improved approaches for future research. Summarising, FSV and ABV are assumed to rotate in a coherent way around the mean vortex axis. And a curved vortex would be subjected to self-induced rotation (Bailey et al. 2018).

Vortex planes normal to the instantaneous axis would intersect which introduces a certain degree of ambiguity to the relation between a vortex centre and its unique plane which raises questions. Existing investigations (Edstrand et al. 2016; Miloud et al. 2020) based on the correction for the in-plane displacement only (Heyes et al. 2004) focus on the analysis of the far field where a smaller bending would be of negligible influence. Here, vortex planes undergo both translation and rotation due to wandering. This raises the following question: Is it possible to correct the flow at the planes for wandering properly? If axial symmetry of the vortex flow was assumed, this would be possible: the transverse shift of the vortex centre and the alignment of the current axis provide the necessary information to merge instantaneous vortex planes at the same streamwise position. However, if the vortex flow is not axisymmetric and unsteady, this may become questionable: the assignment of the planes would be no longer unique. Therefore, only the flow at the vortex centre was corrected for the transverse and rotational wandering motion.

As expected, the time-averaged vorticity and pressure extrema are smoothed out due to wandering. This is different for the axial velocity; one reason may be the independence between the vortex centre's wandering motion and the current axial velocity field's pattern which seems to be highly turbulent indeed.

The reduction of TKE at the wandering-corrected swirling centre (c1) can easily be explained with vanishing transverse velocities following from the definition of c1. This relation marks a simple indication for the trend towards laminar flow at the vortex centre; only the axial normal stresses remain for wandering-corrected TKE. As a restriction, it must be noted that part of the derived wandering motion is attributed to turbulence, because the vortex centre algorithm used the pure flow field that contains turbulence. This manifests e.g. in the distinct inertial sub-range at the FSV and ABV centre that represents nearly isotropic turbulent velocity fluctuations. However, the correction for the pressure centre (c3) does not cancel out all transverse velocity components. And the wandering-corrected TKE evolution confirms the tendency: about two thirds of TKE originate from wandering for the FSV. For the ABV the contribution is less which is an indication for the proximity to the stern separation. Summarising this, the proximity of FSV and ABV to their onset is a plausible reason for the distinct amount of turbulence at the centre. And it is assumed that the strong free-shear layers excite the wandering motion of FSV and ABV.

Considering the varied inflow speed, the present results allow no distinct conclusion on the dominant driving factors and the actual manifestation of the development of turbulence. A further analysis of the TKE budget may clarify this.

Due to the small aspect ratio of the double-body model the FSV pair approaches up to five times its core diameter which is small compared to airplane cases. However, the interaction between both vortices is negligible. And so the interaction between the vortex pair is not the dominant mechanism of wandering which may be the case for wingtip

vortices in the far field. In addition, considering CFD approaches, these findings permit the use of a single-hull model for comparisons with double-body model experiments.

Downstream of the rear shoulder the FSV core flow reveals a transformation to a disordered pattern very similar to a vortex breakdown. Further studies need to verify the occurrence of this breakdown. This may also include its proper classification.

Anderson, Lawton (2001) found a linear relation between the vortex circulation and the axial velocity for wingtip vortices beyond the trailing edge. They mentioned the explanation that vortex filaments wrapped on a helix around the vortex induce axial flow. For the present case the linear relation is not present: although the axial velocity of the FSV changes with the inflow, the circulation does not. However, the difficulties in determining the unique vortex circulation for the present case allow no distinct conclusion. A possible explanation is that the linear relation manifests only for cases with less flow unsteadiness and inhomogeneity. This highlights also the differences between wingtip vortices in the far field, which are often assumed to be axisymmetric, and the present complex FSV flow.

Putting the focus on the vortex as a flow structure highlights the variety of complex effects that can occur with the vortex which dominate the surrounding flow: tracking the vortex in time reveals the coherent wandering motion with a distinct bending and the emergence of a breakdown. As the Reynolds stresses just mark a temporal change at a fixed position, a considerable amount may be attributed to the coherent wandering motion and not to turbulence.

6.2. Outlook

Possible approaches for future investigations are summarised in the following. A short classification is put in front of every point.

- Turbulence modelling: in the framework of hybrid RANS-LES approaches an increased refinement of the upstream wake compared to further downstream may be an efficient approach to focus the initial resolution of turbulence. Downstream the level of resolved TKE is higher which may sustain a coarser grid without a significant decrease in quality.
  Besides, a hybrid model that leads to a faster generation of turbulent structures, i.e. a smaller grey area, would be inherently beneficial. Promising results for a similar case were presented e.g. by Shevchuk et al. (2020) using the dynamic DDES model (Yin et al. 2015).
- Analytical derivations: it may be interesting to derive the Reynolds-stress components for a wandering q-vortex with distinct wandering characteristics, i.e. its principal axes or the consideration of the vortex axis bending. This may provide an intuitive access towards the complex flow. Zeman (1995) conducted pioneering work with the assumption of isotropic Gaussian wandering.

- Wandering analysis: several authors used a low-pass filtered flow field to track vortex wandering (Edstrand et al. 2016; Miloud et al. 2020) free of small-scale turbulent fluctuations, or in other words to separate wandering from turbulence. The reconstruction of the lowest POD modes is one approach. It would also enable the analysis of the vortex axis bending which is influenced by small-scale fluctuations here. It is important to reveal the bending of the coherent vortex axis in order to assess wandering correction of vortex planes.
- Wandering correction: future investigations may reveal whether the bending of the vortex axis is so large that it limits the correction of vortex planes. And maybe there is a consistent approach to correct vortex planes even in case of large axial inclination. A correction of vortex planes would reveal more information about the spatial distribution of Reynolds stresses and the axial velocity within the vortex core region.
- POD analysis: POD offers a large potential for the analysis of coherent vortex features. The application in the near field with respect to other fields like the vorticity may reveal further insight into the interaction between turbulence, vortex instabilities and wandering. Ma et al. (2017) conducted POD on the vorticity field to analyse different kinds of flow instabilities (e.g. shear layer, Kelvin-Helmholtz), Chen et al. (2018) followed a similar approach. Besides, CFD offers the possibility to apply a 3D-POD that would provide a global view on the elongated vortex structure.
- Vortex breakdown: although the breakdown occurs for similar leading-edge vortices above delta wings and it was predicted with all meshes at the same position, its formation may be dominated by numerical or modelling details. A verification by other investigations is recommended.
- Variation of inflow speed: It would be interesting to vary the inflow for future experiments or investigations for other hulls and compare the relation between wake- or jet-like core flow to the vortex circulation referring to Anderson, Lawton (2001). Besides, the analysis of the TKE budget may clarify the driving factors for different manifestations of the core turbulence depending on the inflow.

Bibliography

Abbas, N., Kornev, N. (2016a). 'Study of unsteady loadings on the propeller under steady drift and yaw motion using URANS, hybrid (URANS-LES) and LES methods'. In: *Ship Technology Research* 63.2, pp. 121–131.

Abbas, N., Kornev, N. (2016b). 'Validation of hybrid URANS/LES methods for determination of forces and wake parameters of KVLCC2 tanker at manoeuvring conditions'. In: *Ship technology research* 63.2, pp. 96–109.

Abbas, N., Kornev, N., Shevchuk, I., Anschau, P. (2015). 'CFD prediction of unsteady forces on marine propellers caused by the wake nonuniformity and nonstationarity'. In: *Ocean Engineering* 104, pp. 659–672.

Abdel-Maksoud, M., Müller, V., Xing, T., Toxopeus, S., Stern, F., Petterson, K., Tormalm, M., Kim, S., Aram, S., Gietz, U. et al. (2015). 'Experimental and Numerical Investigations on Flow Characteristics of the KVLCC2 at 30 Drift Angle'. In: *5th World Maritime Technology Conference*.

Alekseenko, S. V., Kuibin, P. A., Okulov, V. L. (2007). *Theory of concentrated vortices: an introduction*. Springer Science & Business Media.

Althaus, W., Bruecker, C., Weimer, M. (1995). 'Breakdown of slender vortices'. In: *Fluid Vortices*. Springer, pp. 373–426.

Anderson, E., Lawton, T. (2001). 'Effect of wing loading on axial velocity in a wingtip vortex'. In: *39th Aerospace Sciences Meeting and Exhibit*, p. 578.

Arndt, R. E. (2002). 'Cavitation in vortical flows'. In: *Annual review of fluid mechanics* 34.1, pp. 143–175.

Arolla, S. K., Durbin, P. A. (2014). 'A rotation/curvature correction for turbulence models for applied CFD'. In: *Progress in Computational Fluid Dynamics, an International Journal* 14.6, pp. 341–351.

Bailey, S. C., Pentelow, S., Ghimire, H. C., Estejab, B., Green, M. A., Tavoularis, S. (2018). 'Experimental investigation of the scaling of vortex wandering in turbulent surroundings'. In: *Journal of Fluid Mechanics* 843, p. 722.

Baker, G., Barker, S., Bofah, K., Saffman, P. (1974). 'Laser anemometer measurements of trailing vortices in water'. In: *Journal of Fluid Mechanics* 65.2, pp. 325–336.

Bandyopadhyay, P. R., Stead, D. J., Ash, R. L. (1991). 'Organized nature of a turbulent trailing vortex'. In: *AIAA journal* 29.10, pp. 1627–1633.

Batchelor, G. K. (1967). 'An Introduction to Fluid Dynamics,(1967)'. In: *Cambridge,: UP xviii* 615.

Batchelor, G. (1964). 'Axial flow in trailing line vortices'. In: *Journal of Fluid Mechanics* 20.4, pp. 645–658.

Berkooz, G., Holmes, P., Lumley, J. L. (1993). 'The proper orthogonal decomposition in the analysis of turbulent flows'. In: *Annual review of fluid mechanics* 25.1, pp. 539–575.

Bhushan, S., Yoon, H., Stern, F., Guilmineau, E., Visonneau, M., Toxopeus, S., Simonsen, C., Aram, S., Kim, S., Grigoropoulos, G. (2019). 'Assessment of computational fluid dynamic for surface combatant 5415 at straight ahead and atatic drift β= 20 deg'. In: *Journal of Fluids Engineering* 141.5.

Bhushan, S., Yoon, H., Stern, F. (2016). 'Large grid simulations of surface combatant flow at straight-ahead and static drift conditions'. In: *International Journal of Computational Fluid Dynamics* 30.5, pp. 356–362.

Birch, D., Lee, T., Mokhtarian, F., Kafyeke, F. (2003). 'Rollup and near-field behavior of a tip vortex'. In: *Journal of aircraft* 40.3, pp. 603–607.

Birch, D., Lee, T., Mokhtarian, F., Kafyeke, F. (2004). 'Structure and induced drag of a tip vortex'. In: *Journal of Aircraft* 41.5, pp. 1138–1145.

Bomphrey, R. J., Henningsson, P., Michaelis, D., Hollis, D. (2012). 'Tomographic particle image velocimetry of desert locust wakes: instantaneous volumes combine to reveal hidden vortex elements and rapid wake deformation'. In: *Journal of The Royal Society Interface* 9.77, pp. 3378–3386.

Bosschers, J. (2018). 'Propeller tip-vortex cavitation and its broadband noise'. PhD thesis. University of Twente, the Netherlands.

Boussinesq, J. (1877). *Essai sur la théorie des eaux courantes*. Impr. nationale.

Broglia, R., Posa, A., Bettle, M. C. (2020). 'Analysis of vortices shed by a notional submarine model in steady drift and pitch advancement'. In: *Ocean Engineering* 218, p. 108236.

Brücker, C. (1993). 'Study of vortex breakdown by particle tracking velocimetry (PTV), Part 2: Spiral-type vortex breakdown'. In: *Experiments in fluids* 14.1-2, pp. 133–139.

Brücker, C., Althaus, W. (1992). 'Study of vortex breakdown by particle tracking velocimetry (PTV), Part 1: Bubble-type vortex breakdown'. In: *Experiments in fluids* 13.5, pp. 339–349.

Burgers, J. M. (1948). 'A mathematical model illustrating the theory of turbulence'. In: *Advances in applied mechanics*. Vol. 1. Elsevier, pp. 171–199.

Chakraborty, P., Balachandar, S., Adrian, R. J. (2005). 'On the relationships between local vortex identification schemes'. In: *Journal of Fluid Mechanics* 535, pp. 189–214.

Chen, C., Wang, Z., Gursul, I. (2018). 'Experiments on tip vortices interacting with downstream wings'. In: *Experiments in Fluids* 59.5, p. 82.

Chong, M., Perry, A. E., Cantwell, B. J. (1990). 'A general classification of three-dimensional flow fields'. In: *Physics of Fluids A: Fluid Dynamics (1989-1993)* 2.5, pp. 765–777.

Chow, J. S., Zilliac, G., Bradshaw, P. (1997a). 'Mean and turbulence measurements in the near field of a wingtip vortex'. In: *AIAA journal* 35.10, pp. 1561–1567.

Chow, J. S., Zilliac, G., Bradshaw, P. (1997b). 'Turbulence Measurements in the Near Field of a Wingtip Vortex'. In: *AGARD, France*.

Chow, J. S., Zilliac, G., Bradshaw, P. (1994). 'Turbulence measurements in the near-field of a wingtip vortex'. In: *ASME-PUBLICATIONS-FED* 203, pp. 61–61.

Churchfield, M. J., Blaisdell, G. A. (2013). 'Reynolds stress relaxation turbulence modeling applied to a wingtip vortex flow'. In: *AIAA journal* 51.11, pp. 2643–2655.

Cisneros, P. S., Voss, S., Werner, H. (2016). 'Efficient nonlinear model predictive control via quasi-lpv representation'. In: *2016 IEEE 55th Conference on Decision and Control (CDC)*. IEEE, pp. 3216–3221.

Corsiglia, V., Schwind, R., Chigier, N. (1973). 'Rapid Scanning, Three-Dimensional Hot-Wire AnemometerSurveys of Wing-Tip Vortices'. In: *Journal of Aircraft* 10.12, pp. 752–757.

Crow, S. C. (1970). 'Stability theory for a pair of trailing vortices'. In: *AIAA journal* 8.12, pp. 2172–2179.

De Visscher, I., Bricteux, L., Winckelmans, G. (2013). 'Aircraft vortices in stably stratified and weakly turbulent atmospheres: simulation and modeling'. In: *AIAA journal* 51.3, pp. 551–566.

Del Pino, C., Parras, L., Felli, M., Fernandez-Feria, R. (2011). 'Structure of trailing vortices: Comparison between particle image velocimetry measurements and theoretical models'. In: *Physics of Fluids* 23.1, p. 013602.

Devenport, W. J., Rife, M. C., Liapis, S. I., Follin, G. J. (1996). 'The structure and development of a wing-tip vortex'. In: *Journal of Fluid Mechanics* 312, pp. 67–106.

Devenport, W. J., Vogel, C. M., Zsoldos, J. S. (1999). 'Flow structure produced by the interaction and merger of a pair of co-rotating wing-tip vortices'. In: *Journal of Fluid Mechanics* 394, pp. 357–377.

Devenport, W. J., Zsoldos, J. S., Vogel, C. M. (1997). 'The structure and development of a counter-rotating wing-tip vortex pair'. In: *Journal of Fluid Mechanics* 332, pp. 71–104.

Dogan, T. K. (2013). 'URANS and DES for Delft catamaran for static drift conditions in deep water'. MA thesis. University of Iowa.

Edstrand, A. M., Davis, T. B., Schmid, P. J., Taira, K., Cattafesta, L. N. (2016). 'On the mechanism of trailing vortex wandering'. In: *Journal of Fluid Mechanics* 801.

Feder, D.-F., Shevchuk, I., Sahab, A., Gerwers, L., Abdel-Maksoud, M. (2019). 'Fore-Body Side Vortex of KVLCC2 at 30° Drift: A Trailing Vortex Resolved with DES and Compared to PIV Data'. In: *Open Journal of Fluid Dynamics* 9.4, pp. 303–325.

Franc, J.-P., Michel, J.-M. (2006). *Fundamentals of cavitation*. Vol. 76. Springer science & Business media.

Fröhlich, J., Von Terzi, D. (2008). 'Hybrid LES/RANS methods for the simulation of turbulent flows'. In: *Progress in Aerospace Sciences* 44.5, pp. 349–377.

Fureby, C., Toxopeus, S., Johansson, M., Tormalm, M., Petterson, K. (2016). 'A computational study of the flow around the KVLCC2 model hull at straight ahead conditions and at drift'. In: *Ocean engineering* 118, pp. 1–16.

Graftieaux, L., Michard, M., Grosjean, N. (2001). 'Combining PIV, POD and vortex identification algorithms for the study of unsteady turbulent swirling flows'. In: *Measurement Science and technology* 12.9, p. 1422.

Green, S. I. (1995). *Fluid Vortices*. Ed. by S. Moreau. Springer Science.

Gritskevich, M. S., Garbaruk, A. V., Schütze, J., Menter, F. R. (2012). 'Development of DDES and IDDES Formulations for the k-ω Shear Stress Transport Model'. In: *Flow, turbulence and combustion* 88.3, pp. 431–449.

Gursul, I. (2005). 'Review of unsteady vortex flows over slender delta wings'. In: *Journal of Aircraft* 42.2, pp. 299–319.

Haller, G. (2005). 'An objective definition of a vortex'. In: *Journal of fluid mechanics* 525, p. 1.

Hellsten, A., Wallin, S. (2009). 'Explicit algebraic Reynolds stress and non-linear eddy-viscosity models'. In: *International Journal of Computational Fluid Dynamics* 23.4, pp. 349–361.

Heyes, A., Jones, R., Smith, D. (2004). 'Wandering of wing-tip vortices'. In: *Proceedings of the 12th international symposium on applications of laser techniques to fluid mechanics*, pp. 35–3.

Hino, T., Stern, F., Larsson, L., Visonneau, M., Hirata, N., Kim, J. (2021). 'Numerical Ship Hydrodynamics, An Assessment of the Tokyo 2015 Workshop'. In: *National Maritime Research Institute, Japan*.

Hommes, T., Bosschers, J., Hoeijmakers, H. (2015). 'Evaluation of the radial pressure distribution of vortex models and comparison with experimental data'. In: *Journal of Physics: Conference Series*. Vol. 656. 1. IOP Publishing, p. 012182.

Issa, R. I. (1986). 'Solution of the implicitly discretised fluid flow equations by operator-splitting'. In: *Journal of computational physics* 62.1, pp. 40–65.

Jacquin, L., Fabre, D., Geffroy, P., Coustols, E. (2001). 'The properties of a transport aircraft wake in the extended near field-An experimental study'. In: *39th Aerospace Sciences Meeting and Exhibit*, p. 1038.

Jacquin, L., Fabre, D., Sipp, D., Coustols, E. (2005). 'Unsteadiness, instability and turbulence in trailing vortices'. In: *Comptes Rendus Physique* 6.4-5, pp. 399–414.

Jacquin, L., Pantano, C. (2002). 'On the persistence of trailing vortices'. In: *Journal of Fluid Mechanics* 471, p. 159.

Jeong, J., Hussain, F. (1995). 'On the identification of a vortex'. In: *Journal of fluid mechanics* 285, pp. 69–94.

Jin, Y., Duffy, J., Chai, S., Chin, C., Bose, N. (2016). 'URANS study of scale effects on hydrodynamic manoeuvring coefficients of KVLCC2'. In: *Ocean engineering* 118, pp. 93–106.

Kornev, N., Abbas, N. (2018). 'Vorticity structures and turbulence in the wake of full block ships'. In: *Journal of Marine Science and Technology* 23.3, pp. 567–579.

Kornev, N., Shevchuk, I., Abbas, N., Anschau, P., Samarbakhsh, S. (2019). 'Potential and limitations of scale resolved simulations for ship hydrodynamics applications'. In: *Ship Technology Research* 66.2, pp. 83–96.

Kume, K., Hasegawa, J., Tsukada, Y., Fujisawa, J., Fukasawa, R., Hinatsu, M. (2006). 'Measurements of hydrodynamic forces, surface pressure, and wake for obliquely towed tanker model and uncertainty analysis for CFD validation'. In: *Journal of marine science and technology* 11.2, pp. 65–75.

Lamb, H. (1932). 'Hydrodynamics'. In: *Cambridge: Univ. Press1879–1932* 427.

Lambourne, N., Bryer, D. (1961). 'The bursting of leading-edge vortices-some observations and discussion of the phenomenon, no. 3282'. In: *Aeronautical Research Council* 3832.

Larsson, L., Stern, F., Bertram, V. (2003). 'Benchmarking of computational fluid dynamics for ship flows: the Gothenburg 2000 workshop'. In: *Journal of Ship Research* 47.1, pp. 63–81.

Larsson, L., Stern, F., Visonneau, M. (2014). *Numerical ship hydrodynamics: an assessment of the Gothenburg 2010 workshop*. Springer.

Le, H., Moin, P., Kim, J. (1997). 'Direct numerical simulation of turbulent flow over a backward-facing step'. In: *Journal of fluid mechanics* 330, pp. 349–374.

Lee, S.-J., Kim, H.-R., Kim, W.-J., Van, S.-H. (2003). 'Wind tunnel tests on flow characteristics of the KRISO 3,600 TEU containership and 300K VLCC double-deck ship models'. In: *Journal of Ship Research* 47.1, pp. 24–38.

Lee, T., Pereira, J. (2010). 'Nature of wakelike and jetlike axial tip vortex flows'. In: *Journal of Aircraft* 47.6, pp. 1946–1954.

Liefendahl, M., Revstedt, J., Fureby, C. (2020). 'A Critical Survey on Turbulence Modeling Methods for Ship Aero- and Hydrodynamics'. In: *Proceedings of 33rd Symposium on Naval Hydrodynamics, Osaka, Japan*.

Liew, R., Zeegers, J., Kuerten, J. G., Michałek, W. (2013). '3D Velocimetry and droplet sizing in the Ranque–Hilsch vortex tube'. In: *Experiments in fluids* 54.1, p. 1416.

Longo, J., Stern, F. (2002). 'Effects of drift angle on model ship flow'. In: *Experiments in fluids* 32.5, pp. 558–569.

Lucca-Negro, O., O'Doherty, T. (2001). 'Vortex breakdown: a review'. In: *Progress in energy and combustion science* 27.4, pp. 431–481.

Ma, B.-F., Wang, Z., Gursul, I. (2017). 'Symmetry breaking and instabilities of conical vortex pairs over slender delta wings'. In: *Journal of Fluid Mechanics* 832, pp. 41–72.

Menter, F., Esch, T. (2001). 'Elements of industrial heat transfer predictions'. In: *16th Brazilian Congress of Mechanical Engineering (COBEM)*, pp. 26–30.

Menter, F., Kuntz, M., Langtry, R. (2003). 'Ten years of industrial experience with the SST turbulence model'. In: *Turbulence, heat and mass transfer* 4.1, pp. 625–632.

Merziger, G., Mühlbach, G., Wille, D., Wirth, T. (2007). *Formeln + Hilfen zur Höheren Mathematik*. Binomi Verlag.

Miloud, K. B., Dghim, M., Fellouah, H., Ferchichi, M. (2020). 'Free-stream turbulence interaction with a wing-tip vortex'. In: *Journal of Wind Engineering and Industrial Aerodynamics* 206, p. 104211.

Misaka, T., Holzäpfel, F., Hennemann, I., Gerz, T., Manhart, M., Schwertfirm, F. (2012). 'Vortex bursting and tracer transport of a counter-rotating vortex pair'. In: *Physics of Fluids* 24.2, p. 025104.

Mockett, C. (2009). 'A Comprehensive Study of Detached Eddy Simulation'. PhD thesis. Technische Universität Berlin.

Moore, D. W., Saffman, P. G. (1973). 'Axial flow in laminar trailing vortices'. In: *Proceedings of the Royal Society of London. A. Mathematical and Physical Sciences* 333.1595, pp. 491–508.

Morton, S. (2009). 'Detached-eddy simulations of vortex breakdown over a 70-degree delta wing'. In: *Journal of aircraft* 46.3, pp. 746–755.

Page, R., Clawson, K. (1991). 'Garodz. LJ and Rudis, RP,"Report on Tower Fly-by testing,"' in: *Proceedings of the FAA Wake Vortices Conference, Washington, DC*.

Patankar, S. (2018). *Numerical heat transfer and fluid flow*. 1st. Taylor & Francis.

Pereira, F. S., Eça, L., Vaz, G., Kerkvliet, M. (2019). 'Application of second-moment closure to statistically steady flows of practical interest'. In: *Ocean Engineering* 189, p. 106372.

Phillips, W. (1981). 'The turbulent trailing vortex during roll-up'. In: *Journal of Fluid Mechanics* 105.451.

Pope, S. B. (2000). *Turbulent flows*. 1st ed. Cambridge University Press.

Qiu, S., Xiang, Y., Liu, H. (2020). 'The evolution of wingtip vortex wandering: a stability analysis based on stereo-PIV experiment'. In: *Aerospace Systems* 3.1, pp. 71–77.

Queutey, P., Guilmineau, E., Visonneau, M., Wackers, J., Deng, G. (2016). 'RANS and Hybrid RANS-LES simulations around the Japan Bulk Carrier of the Tokyo 2015 CFD Workshop'. In:

Raffel, M., Willert, C. E., Scarano, F., Kähler, C. J., Wereley, S. T., Kompenhans, J. (2018). *Particle image velocimetry: a practical guide*. Springer.

Ramaprian, B., Zheng, Y. (1997). 'Measurements in rollup region of the tip vortex from a rectangular wing'. In: *AIAA journal* 35.12, pp. 1837–1843.

Revell, A. J., Craft, T. J., Laurence, D. R. (2011). 'Turbulence modelling of unsteady turbulent flows using the stress strain lag model'. In: *Flow, turbulence and combustion* 86.1, pp. 129–151.

Reynolds, O. (1895). 'On the dynamical theory of incompressible viscous fluids and the determination of the criterion'. In: *Philosophical transactions of the royal society of london.(a.)* 186, pp. 123–164.

Saffman, P. G. (1992). *Vortex dynamics*. Cambridge university press.

Sagaut, P., Deck, S., Terracol, M. (2013). *Multiscale and multiresolution approaches in turbulence: LES, DES and hybrid RANS/LES methods: applications and guidelines*. Vol. 2. London: Imperial College Press.

Schade, H., Kunz, E., Kameier, F., Paschereit, C. O. (2013). *Strömungslehre*. Walter de Gruyter.

Schauerhamer, D. G., Robinson, S. K. (2017). 'Computational-Fluid-Dynamics Best Practices for Aircraft Wing-Tip Vortex Roll-Up'. In: *Journal of Aircraft* 54.4, pp. 1552–1565.

Schiller, P., Weitendorf, E.-A., Lücke, T. (2013). 'Kavitationskeime und propellerinduzierte Druckschwankungen an der Schiffsaussenhaut'. In: *Kavitation in Technik und Medizin, 5. Workshop*.

Schlichting, H., Gersten, K. (2006). *Grenzschichttheorie*. Vol. 10. Springer-Verlag.

Shekarriz, A., Fu, T., Katz, J., Huang, T. (1993). 'Near-field behavior of a tip vortex'. In: *AIAA journal* 31.1, pp. 112–118.

Shevchuk, I., Sahab, A., Abdel-Maksoud, M. (June 2020). 'Experimental and numerical studies of the flow around the JBC hull form at straight ahead condition and 8° drift angle'. In: *Proceedings of the 33rd Symposium on Naval Hydrodynamics*. Osaka, Japan.

Shevchuk, I. (2016). 'Study of Unsteady Hydrodynamic Effects in the Ship Stern Area Under Shallow Water Conditions'. PhD thesis. University of Rostock.

Shima, E., Kitamura, K., Haga, T. (2013). 'Green–gauss/weighted-least-squares hybrid gradient reconstruction for arbitrary polyhedra unstructured grids'. In: *AIAA journal* 51.11, pp. 2740–2747.

Shur, M. L., Strelets, M. K., Travin, A. K., Spalart, P. R. (2000). 'Turbulence Modeling in Rotating and Curved Channels: Assessing the Spalart-Shur Correction'. In: *AIAA Journal* 38.5, pp. 784–792.

Shur, M. L., Spalart, P. R., Strelets, M. K., Travin, A. K. (2008). 'A hybrid RANS-LES approach with delayed-DES and wall-modelled LES capabilities'. In: *International Journal of Heat and Fluid Flow* 29.6, pp. 1638–1649.

SIMMAN (2008). Copenhagen. URL: `http://www.simman2008.dk/KVLCC/KVLCC2/tanker2.html`.

Simonsen, C., Stern, F. (2014). 'SIMMAN 2014 workshop on verification and validation of ship maneuvering simulation methods'. In: *Draft Workshop Proceedings*.

Smirnov, P. E., Menter, F. R. (2009). 'Sensitization of the SST turbulence model to rotation and curvature by applying the Spalart–Shur correction term'. In: *Journal of Turbomachinery* 131.4.

Son, M. S., Sa, J. H., Park, S. H., Byun, Y. H., Cho, K. W. (2015). 'Delayed detached-eddy simulation of vortex breakdown over a 70° delta wing'. In: *Journal of Mechanical Science and Technology* 29.8, pp. 3205–3213.

Spalart, P. R., Deck, S., Shur, M., Squires, K., Strelets, M. K., Travin, A. (2006). 'A new version of detached-eddy simulation, resistant to ambiguous grid densities'. In: *Theoretical and computational fluid dynamics* 20.3, pp. 181–195.

Spalart, P. R., Shur, M. (1997). 'On the Sensitization of Turbulence Models to Rotation and Curvature'. In: *Aerospace Science and Technology* 1.5, pp. 297–302.

Spalart, P. R. (1998). 'Airplane trailing vortices'. In: *Annual Review of Fluid Mechanics* 30.1, pp. 107–138.

Spalart, P. R., Garbaruk, A. V. (2019). 'The Predictions of Common Turbulence Models in a Mature Vortex'. In: *Flow, Turbulence and Combustion* 102.3, pp. 667–677.

Spalart, P. R., Jou, W.-H., Strelets, M., Allmaras, S. R. (1997). 'Comments on the feasibility of LES for wings, and on a hybrid RANS/LES approach'. In: *Proceedings of first AFOSR international conference on DNS/LES*. Greyden Press.

Spalart, P. (2000). 'Trends in turbulence treatments. AIAA Paper 2000–2306'. In: *38th AIAA Aerospace Sciences Meeting and Exhibit, Reno, Nev.*

Stern, F., Agdrup, K. (2008). 'SIMMAN 2008 workshop on verification and validation of ship maneuvering simulation methods'. In: *Draft Workshop Proceedings*.

Stern, F., Ismail, F., Xing, T., Carrica, P. (2008). 'Vortical and turbulent structures using various convection schemes with algebraic reynolds stress-DES model for the KVLCC2 at large drift angles'. In: *Proceedings 27th Symposium Naval Hydrodynamics, Seoul, Korea*.

Stern, F., Yang, J., Wang, Z., Sadat-Hosseini, H., Mousaviraad, M., Bhushan, S., Xing, T. (2013). 'Computational ship hydrodynamics: Nowadays and way forward'. In: *International Shipbuilding Progress* 60.1-4, pp. 3–105.

Strelets, M. (2001). 'Detached Eddy Simulation of massively separated flows'. In: *39th Aerospace sciences meeting and exhibit*, p. 879.

Sujudi, D., Haimes, R. (1995). 'Identification of swirling flow in 3-D vector fields'. In: p. 1715.

Tahara, Y., Longo, J., Stern, F. (2002). 'Comparison of CFD and EFD for the Series 60 C B= 0.6 in steady drift motion'. In: *Journal of marine science and technology* 7.1, pp. 17–30.

Taira, K., Brunton, S. L., Dawson, S. T., Rowley, C. W., Colonius, T., McKeon, B. J., Schmidt, O. T., Gordeyev, S., Theofilis, V., Ukeiley, L. S. (2017). 'Modal analysis of fluid flows: An overview'. In: *Aiaa Journal* 55.12, pp. 4013–4041.

Toxopeus, S., Jasak, H., Visonneau, M., Bordier, L., Papadakis, G., Stern, F., Aram, S. (2020). *CFD Validation for surface combatant 5415 at 10 deg drift angle, chapter 3*. Tech. rep.

Toxopeus, S., Simonsen, C., Guilmineau, E., Visonneau, M., Xing, T., Stern, F. (2013). 'Investigation of water depth and basin wall effects on KVLCC2 in manoeuvring motion using viscous-flow calculations'. In: *Journal of Marine Science and Technology* 18.4, pp. 471–496.

Tryggeson, H. (2007). 'Analytical vortex solutions to Navier-Stokes equation'. PhD thesis. Växjö University Press.

Van Doormaal, J. P., Raithby, G. D. (1984). 'Enhancements of the SIMPLE method for predicting incompressible fluid flows'. In: *Numerical heat transfer* 7.2, pp. 147–163.

Van Dyke, M. (1982). 'An album of fluid motion'. In:

Versteeg, H. K., Malalasekera, W. (2007). *An introduction to computational fluid dynamics: the finite volume method*. Second Edition. Pearson education.

Visonneau, M., Deng, G., Guilmineau, E., Queutey, P., Wackers, J. (Sept. 2016). 'Local and global assessment of the flow around the Japan bulk carrier with and without energy saving devices at model and full scale'. In: *31st ONR Symposium on Naval Hydrodynamics*. Monterey, United States.

Visonneau, M., Guilmineau, E., Rubino, G. (2018). 'Computational analysis of the flow around a surface combatant at 10° static drift and dynamic sway conditions'. In: *32nd Symposium on Naval Hydrodynamics*.

Visonneau, M., Guilmineau, E., Rubino, G. (2020a). 'Computational Analysis of the Flow Around a Surface Combatant at 10°'. In: *Progress in Hybrid RANS-LES Modelling*. Springer, pp. 389–400.

Visonneau, M., Guilmineau, E., Rubino, G. (2020b). 'Local Flow around a Surface Combatant at Various Static Drift Conditions: The Role Played by Turbulence Closures'. In: *Proceedings of the 33rd Symposium on Naval Hydrodynamics*.

Vuorinen, V., Keskinen, J.-P., Duwig, C., Boersma, B. (2014). 'On the implementation of low-dissipative Runge–Kutta projection methods for time dependent flows using OpenFOAM'. In: *Computers & Fluids* 93, pp. 153–163.

Weiss, J. (2019). 'A tutorial on the proper orthogonal decomposition'. In: *AIAA Aviation 2019 Forum*, p. 3333.

Weller, H. G., Tabor, G., Jasak, H., Fureby, C. (1998). 'A tensorial approach to computational continuum mechanics using object-oriented techniques'. In: *Computers in Physics* 12.6, pp. 620–631.

Wieneke, B. (2017). 'PIV uncertainty quantification and beyond'. PhD thesis. Delft University of Technology.

Wilcox, D. C. (2006). *Turbulence modeling for CFD*. Vol. 3. DCW Industries La Canada, CA.

Xing, T., Bhushan, S., Stern, F. (2012). 'Vortical and turbulent structures for KVLCC2 at drift angle 0, 12, and 30 degrees'. In: *Ocean Engineering* 55, pp. 23–43.

Xue, Y., Kumar, C., Lee, S.-K., Giacobello, M., Manovski, P. (2020). 'Identification and analysis of the meandering of a fin-tip vortex using Proper Orthogonal Decomposition (POD)'. In: *International Journal of Heat and Fluid Flow* 82, p. 108556.

Yang, X., Yin, Y., Lian, J. (2019). 'A numerical study on flow field and maneuvering derivatives of KVLCC2 model at drift condition'. In: *Journal of Marine Engineering & Technology*, pp. 1–12.

Yin, Z., Reddy, K., Durbin, P. A. (2015). 'On the dynamic computation of the model constant in delayed detached eddy simulation'. In: *Physics of Fluids* 27.2, p. 025105.

Zeman, O. (1995). 'The persistence of trailing vortices: a modeling study'. In: *Physics of Fluids* 7.1, pp. 135–143.

A. Existing Experiments

Table A.1 gives an overview over existing experiments and the ones conducted in accordance with the present thesis that were not finally processed at the time of writing.

Table A.1.: Overview of existing experiments on KVLCC2 with focus on steady drift conditions and data on the vortex system/ flow. Abbreviations: M KVLCC2M, D increased draught, T design draught, PF propeller fairing, TW trip wire, P propeller appended, WT wind tunnel, DB double body model, TT towing tank. References: (A) Abdel-Maksoud et al. (2015), (B) Kume et al. (2006), (C) S.-J. Lee et al. (2003)

Reference	Model	Scale	Facility	Drift [°]	Re L_{oa}	Data
TUHH 2020	D, PF, TW	208.5	WT/ DB	0, 12, 30	2.6e6	TPIV for FSV, ABV
(A)	D, PF, TW	208.5	WT/ DB	30	2.7e6	SPIV for FSV, ABV, ASV LDA oil film for limiting streamlines smoke for visualisation
(B)	M, T, TW	64.4	TT	0/ 6/ 12, (9/18)	4.1e6	forces (0/6/9/12/18), hull pressure (0/6/12), 8-hole spherical pitot tube for wake field at prop. plane (0/6/12)
(C)	T, PF	116.0	WT/ DB	0	4.8e6	hot-wire anem. for wake field at near prop. plane, oil film for limiting streamlines

B. Further Details on the Vortex Flow

Additional numerical and experimental results are presented here. Mostly the were referred in Ch. 5. Especially the figures in Sec. B.5 are worth to be considered also without the link to the mentioned chapter. This chapter starts with a summary of frequently used formulas.

B.1. General Flow Variables

Throughout the thesis the time-averaged (**t-a**) flow is compared with the wandering-corrected (**w-c**) flow that is distinguished by both abbreviations in brackets.

The following variables are used throughout the thesis: stagnation pressure q_∞, pressure coefficient c_p, total pressure p_0, normalised helicity (for brevity the addition 'normalised' is dropped) H_n:

$$q_\infty = \tfrac{1}{2}\,\rho\,U_\infty^2 \tag{B.1}$$

$$c_p = \frac{p - p_\infty}{q_\infty} \tag{B.2}$$

$$p_0 = p + \tfrac{1}{2}\,\rho\,|\boldsymbol{U}|^2 \tag{B.3}$$

$$H_n = \frac{\boldsymbol{U}\cdot\boldsymbol{\omega}}{|\boldsymbol{U}|\,|\boldsymbol{\omega}|} = \cos\Big(\angle\big(\boldsymbol{U},\boldsymbol{\omega}\big)\Big) \tag{B.4}$$

with the static pressure p and zero pressure level $p_\infty = 0$. For the single-hull case, the velocity and vorticity vector of both FSV and ABV are oriented in opposite directions. So the negative helicity exhibits the negative vortex rotation around the velocity vector in terms of the right-hand rule.

The second largest invariant of the velocity gradient tensor λ_2 is used for isolines and isosurfaces to visualise the vortex core region. Its unit [1/s] is usually omitted for brevity.

The vortex axis is assumed to be represented by the vorticity vector at the vortex centre. The axial velocity at the vortex centre is defied as the projection of the velocity vector onto the vortex axis, both at the vortex centre here with index 0

$$U_{ax} = \boldsymbol{U_0}\cdot\frac{\boldsymbol{\omega}_0}{|\boldsymbol{\omega}_0|} \tag{B.5}$$

As the vortex axis is inherently considered, wandering correction of U_{ax} considers both: the in-plane displacement and the variation of the vortex axis.

B.2. Numerical Setup

As the boundary layer flow is resolved down to the wall, the mesh becomes fine close to the hull. Figure B.1 depicts the layer cells and the transition to the hexahedral cells.

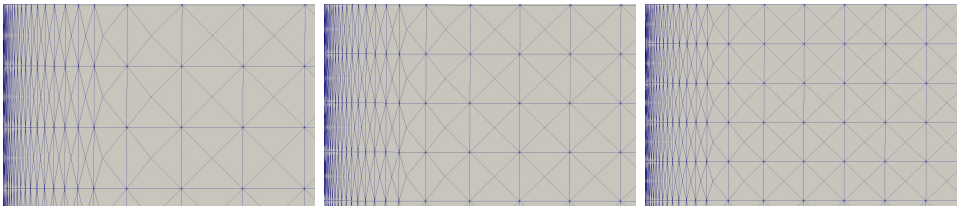

Figure B.1.: Visualisation of the grid close to the hull. From left to right: coarse (g3), medium (g2) and fine (g1) mesh.

B.3. Drift Angle Influence

A simple study on the influence of the drift angle on the vortex wake has been presented in Sec. 5.1. Herein, further results are presented that reveal two aspects:

- The high drift angle is most suitable for DES because enough turbulence develops.
- For the high drift angle, the error of a sensitised RANS turbulence model is largest.

Figure B.2 depicts the relative resolved TKE and the numerical grid and Fig. B.3 visualises the relative axial velocity for the different inflow angles.

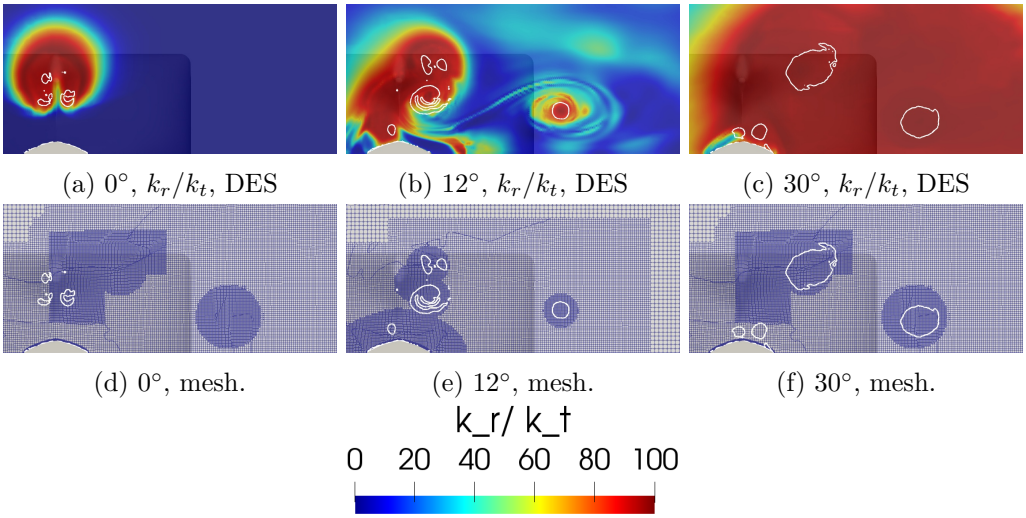

(a) 0°, k_r/k_t, DES (b) 12°, k_r/k_t, DES (c) 30°, k_r/k_t, DES

(d) 0°, mesh. (e) 12°, mesh. (f) 30°, mesh.

Figure B.2.: Resolved part of the turbulence scaled to total part in percent in stern frame plane for three drift angles: straight ahead 0° (left), 12° (centre) and 30° (right column). The white isolines represent $\overline{\lambda_2} = 1e5$. The hull is visible in the background. Similar to Fig. 5.2

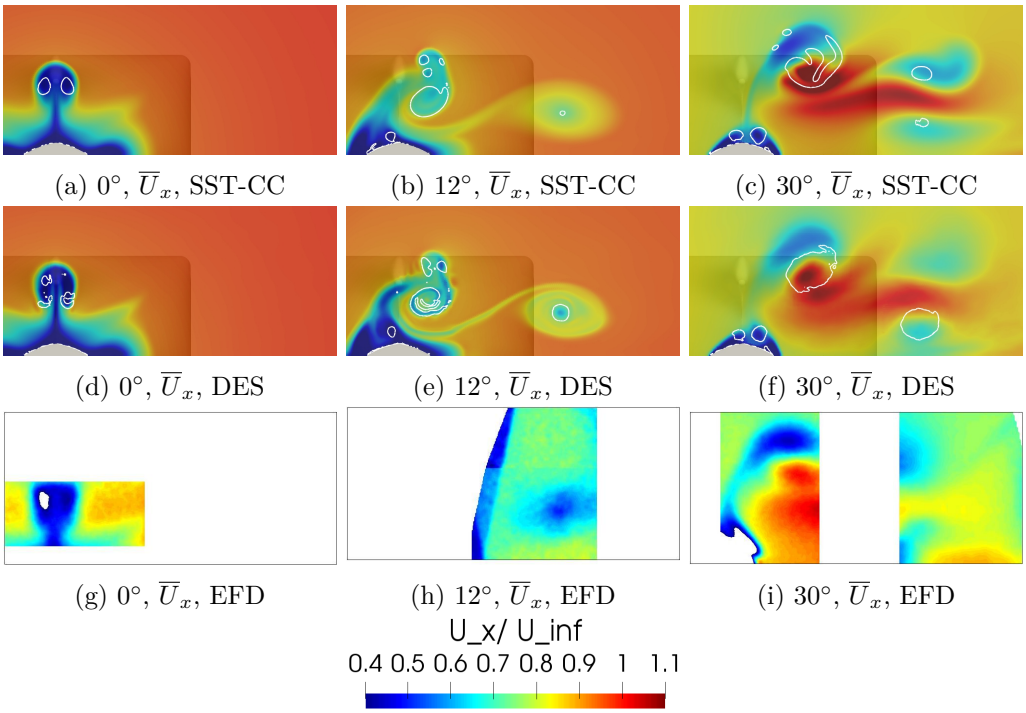

(a) 0°, $\overline{U}_x$, SST-CC (b) 12°, $\overline{U}_x$, SST-CC (c) 30°, $\overline{U}_x$, SST-CC

(d) 0°, $\overline{U}_x$, DES (e) 12°, $\overline{U}_x$, DES (f) 30°, $\overline{U}_x$, DES

(g) 0°, $\overline{U}_x$, EFD (h) 12°, $\overline{U}_x$, EFD (i) 30°, $\overline{U}_x$, EFD

Figure B.3.: Axial flow in transom stern plane for different drift angles, similar to Fig. 5.2. EFD represents preliminary results.

B.4. Verification

Figure B.4 visualises the blending factor for the convection discretisation exemplary for the coarse mesh. Blue regions denote a combination of 99% central differencing and 1% linear upwind, red regions denote pure linear upwind. The vortex system is treated with a low-diffusive scheme.

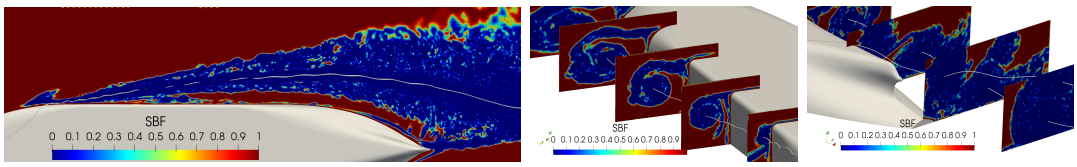

(a) Plane through FSV.

(b) Bow with planes X4, X6, X8, X10 and X12.

(c) Stern region with planes X11, X13, X15, X17.

Figure B.4.: Blending factor (instantaneous field) for convection discretisation using the example of the coarse mesh. Streamlines represent FSV and ABV cores.

Figure B.5 visualises the RANS-LES interface near the hull in the stern region. The initial separation of the bottom's boundary layer is in RANS mode but switches to LES after a short distance.

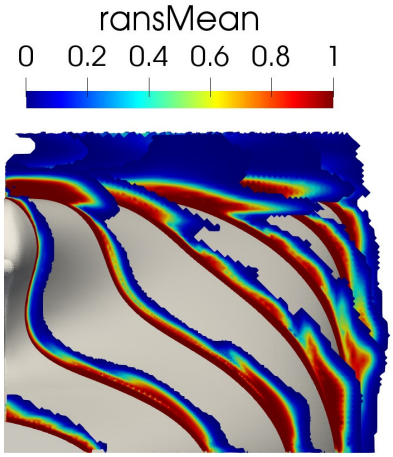

Figure B.5.: Subdivision into RANS- and LES-part in stern region, coarse mesh, time-averaged result, threshold value 0.01. Planes X9, X10, ..., X15.

Concerning the verification of the DES approach, one can state that the grey area is small and the critical amount of 80% resolved TKE is fulfilled, see Fig. B.6. Figure B.7 shows that the wake turbulence is resolved by more than 95% right outside the boundary layer already on the coarse mesh, so the LES resolution is proper.

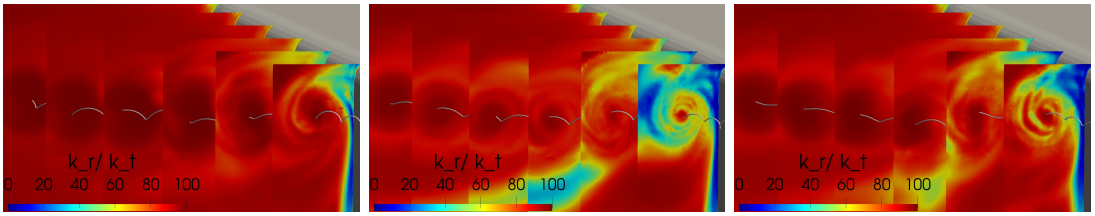

(a) 19 m/s (b) 25 m/s (c) 31 m/s

Figure B.6.: Resolved to total TKE k_r/k_t around initial FSV with planes X4, X5, ..., X9 for different inflow speeds, in addition to Fig. 5.26.

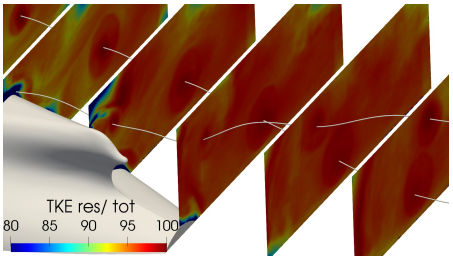

Figure B.7.: Resolved part of TKE scaled to total TKE in the stern region, coarse mesh only.

Grid Study The increased mesh resolution expands the resolved turbulence to higher frequencies as expected (Fröhlich, Von Terzi 2008, p. 358), see Fig. B.8. The end of the inertial range (parallel to $f^{-5/3}$) is shifted to higher frequencies for finer mesh (and temporal) resolution. For the comparison of the g1-curve with the one in Fig. 5.35 mind that the latter shows both curves for X12 and X15 superimposing.

Figure B.9 visualises the influence of grid refinement on the FSV centre flow. Details on the grid are presented in Sec. 4.3. With increasing spatial resolution the vorticity and axial velocity increase and the pressure decreases, indicating a stronger vortex. The same trend occurs for the resolved turbulence energy. And the same trend can be seen for the ABV centre flow in Fig. B.10. All in all, one can state that all grid resolutions predict the same physics of the vortex flow. As the grid refinement also enriches the resolved content of velocity fluctuations, the difference cannot be attributed to numerical diffusion errors only, see e.g. Sagaut et al. (2013).

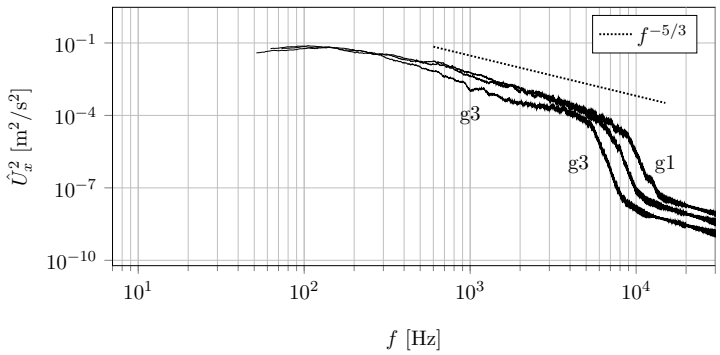

Figure B.8.: Turbulence energy spectrum for single-hull meshes coarse (g3, bottom line), medium (g2, middle line) and fine (g1) at FSV centre in plane X12 (moving mean with 100 samples).

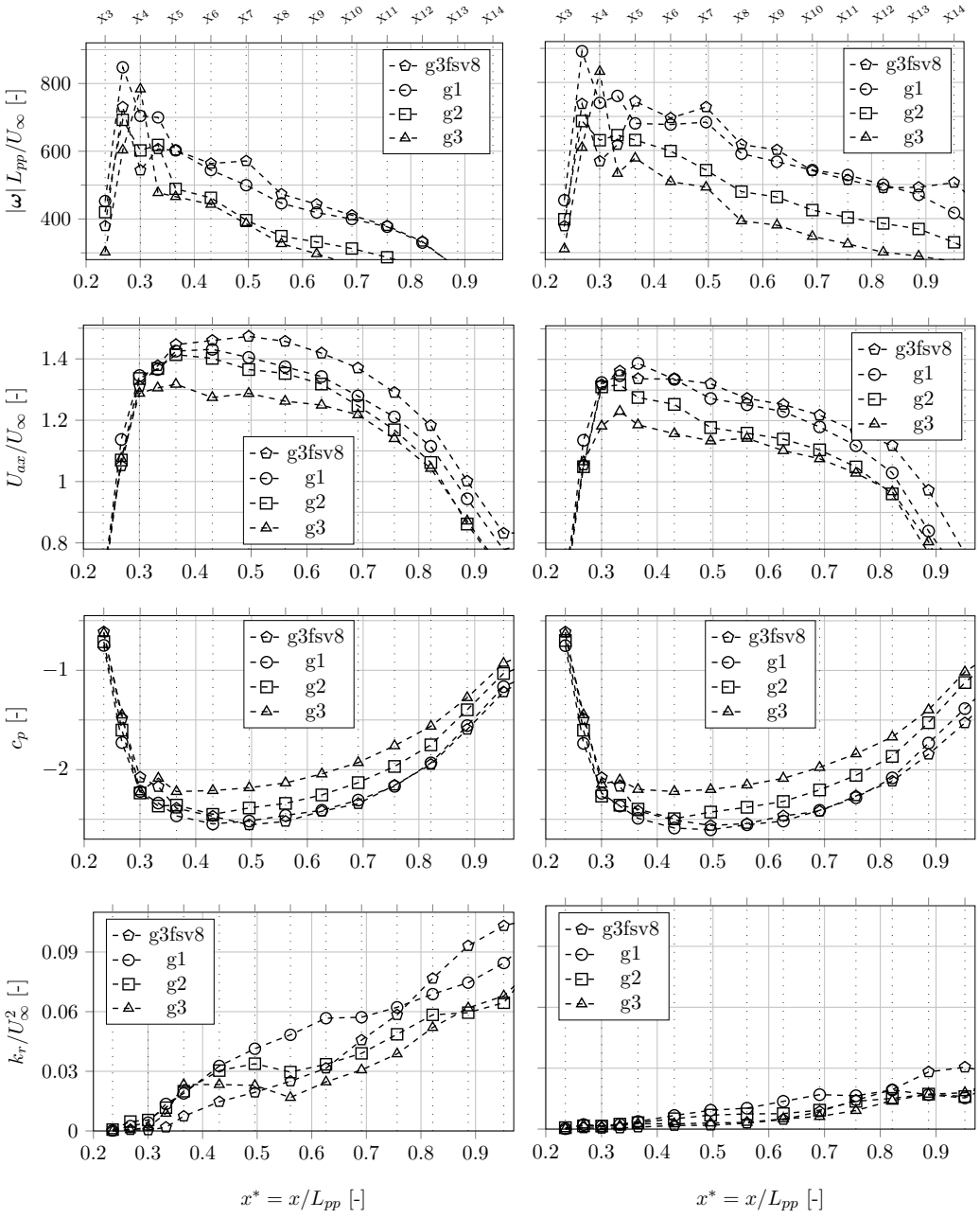

Figure B.9.: Vortex centre flow at FSV for different grids. Left column: time-averaged flow, right one: wandering-corrected flow with same limits. The focus is laid on the region upstream the vortex breakdown.

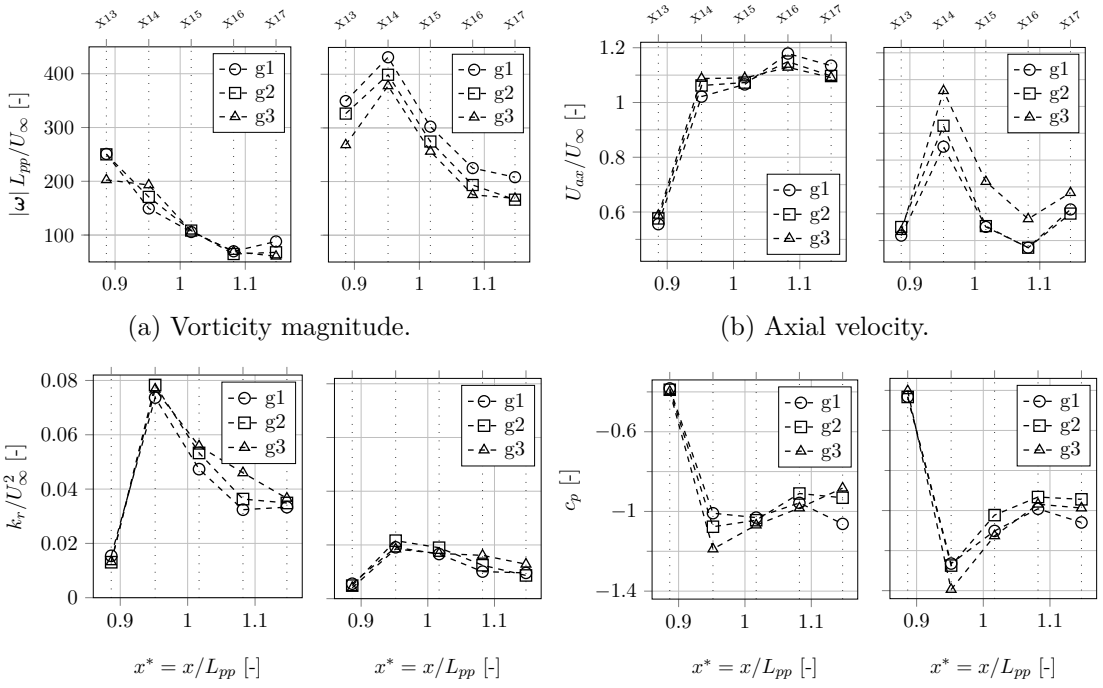

(a) Vorticity magnitude.

(b) Axial velocity.

(c) TKE.

(d) Pressure.

Figure B.10.: Vortex centre flow at ABV for different grids. Left column: time-averaged flow, right one: wandering-corrected flow with same limits. The focus is laid on the region upstream the vortex breakdown.

B.5. Flow Visualisation

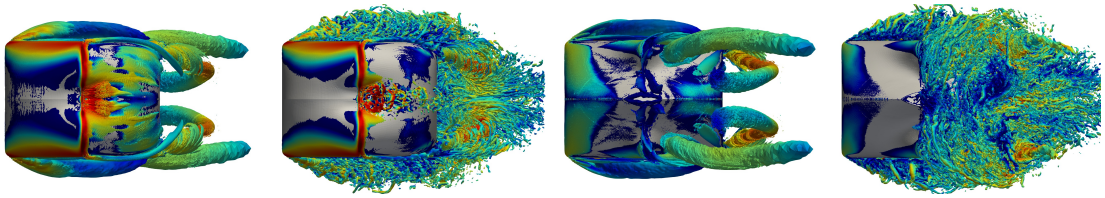

(a) front view, U (b) front view, $\overline{U}$ (c) rear view, U (d) rear view, $\overline{U}$

Figure B.11.: 2D-front and rear view onto vortex system for double-body model, vortex isosurfaces with $\overline{\lambda_2} = 10^5 \mathrm{s}^{-1}$ and $\lambda_2 = 10^6 \mathrm{s}^{-1}$. Coloured by velocity magnitude.

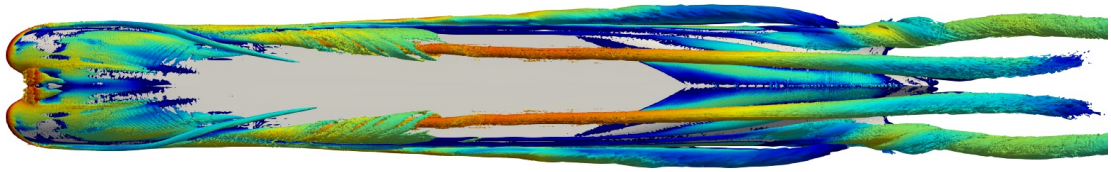

(a) Time-averaged flow $\overline{U}$.

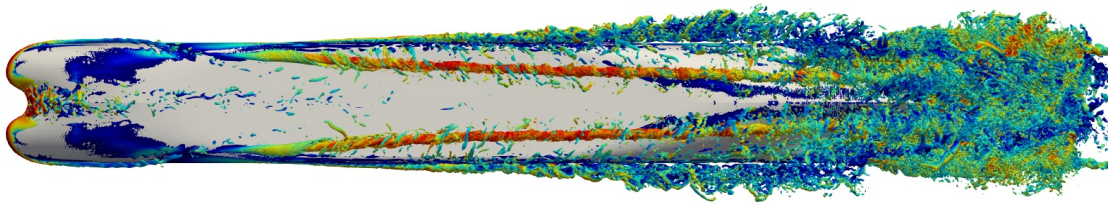

(b) Instantaneous flow U.

Figure B.12.: 2D-Side view onto vortex system for double-body model, vortex isosurfaces with $\overline{\lambda_2} = 10^5 \mathrm{s}^{-1}$ and $\lambda_2 = 10^6 \mathrm{s}^{-1}$. Coloured by velocity magnitude.

Figures B.11 and B.12 visualise the vortex system of the double-body medium mesh in 2D planar view. The time-averaged vortices reveal their deformation and initial merging of FSV and ABV in the wake. The instantaneous structures represent the presence of plenty of secondary vortical structures that surround the major trailing vortices. The potential of scale-resolving simulations is visually highlighted.

For the coarse mesh, Fig. B.13 depicts vortical structures of different strength. This corresponds to a qualitative representation for resolved turbulence: With increasing iso-value, the amount of secondary vortical structures around the upstream FSV decreases and the FSV core is cut further downstream. In the vicinity of the ABV, many structures occur which highlights the strong local separation: concerning the applicability of DES in terms of the grey-area problem, this is a positive result.

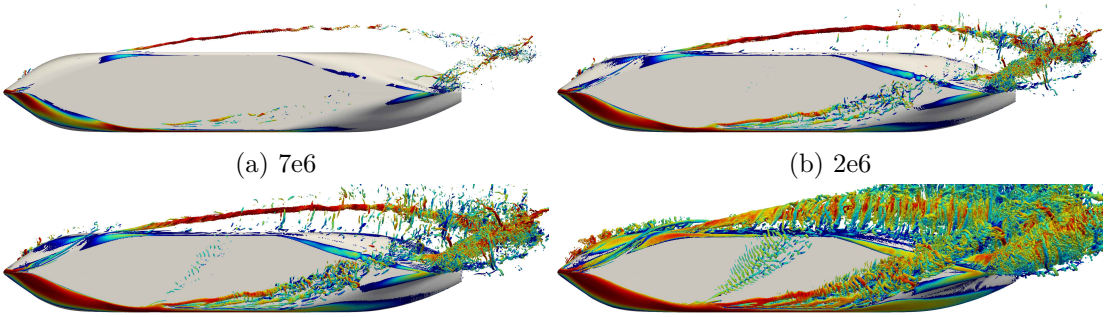

(a) 7e6 (b) 2e6

(c) 1e6. (d) 1e5.

Figure B.13.: Instantaneous vortex system with different λ_2-iso-values [unit: 1/s]. Coloured by velocity magnitude, coarse mesh g3.

Figure B.14 shows the same isosurface $\lambda_2 = 10^6 s^{-1}$ on four different grid densities. The increasing number of resolved vortical structures on finer meshes represents the increase of resolved turbulence, as most of these structures are located inside the free-shear layer of the FSV of the highly turbulent mixing zone in the stern region.

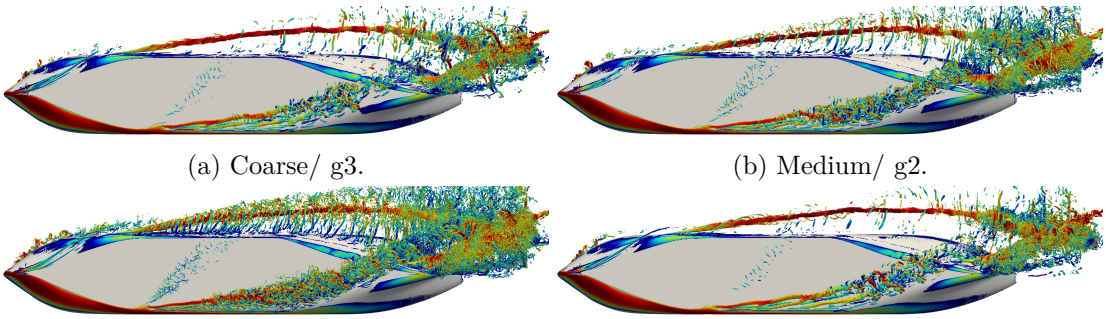

(a) Coarse/ g3. (b) Medium/ g2.

(c) Fine/ g1. (d) Coarse-FSV2/ g3fsv8

Figure B.14.: Instantaneous vortex system on different grid densities. Coloured by velocity magnitude.

B.6. Wandering Analysis

Displacement of the Vortices Devenport, Rife et al. (1996, p. 100) reported that the wandering amplitude corresponds to 30% of the core radius in the far field which leads to a considerable influence. Figure B.15 visualises the amplitude for the time-averaged flow which is an estimation of the upper limit for the wandering-corrected vortex: for the present case the relative amplitude (scaled to the core size) is within the same order of magnitude compared to Devenport. This highlights that wandering may be relevant in the near field.

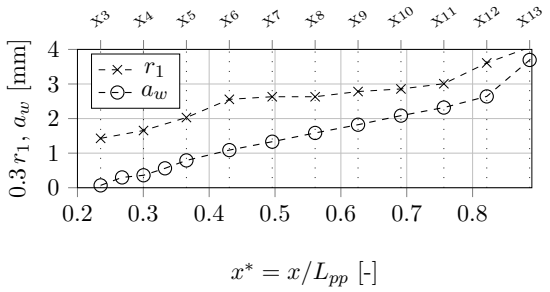

Figure B.15.: Wandering amplitude and 30% of the core radius of FSV.

Angle of the Vortices Figure B.16 reveals in combination with Fig. 5.17 the orientation of the FSV and ABV vortex axes: as the average vortex axis is perpendicular to the y- and z-axis, the vortex axis rotates or bends around the x-axis. This is supported by the nearly equal standard deviation for all axes.[1]

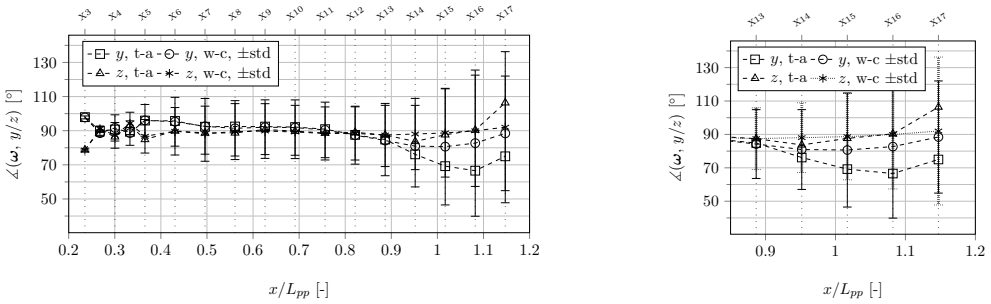

(a) FSV. (b) ABV.

Figure B.16.: Angle between vortex axis and coordinate axes y and z for centre c1. For y and z the curves nearly collapse and are not required to be distinguished for the current conclusions.

Figure B.17 reveals the negligible influence of the varied inflow speed on the alignment of the vortex axis. This is also valid for the angle to the y- and z- axis.

Influence of Double-Body Model Figure B.18 visualises a comparison between the FSV wandering properties of the single- and double-hull. The orientation of the principal axes between the single-hull and the corresponding part of the double-hull (termed 'a') nearly coincides, the other part has an inverted orientation that is due to the different alignment with respect to the z-axis. The amplitudes represented by the length of the arrows in major and minor direction differ very little by less than 10% between single-

[1]The accurate distinction between y and z in the Figure is not important, the important point indeed is that both curves nearly collapse.

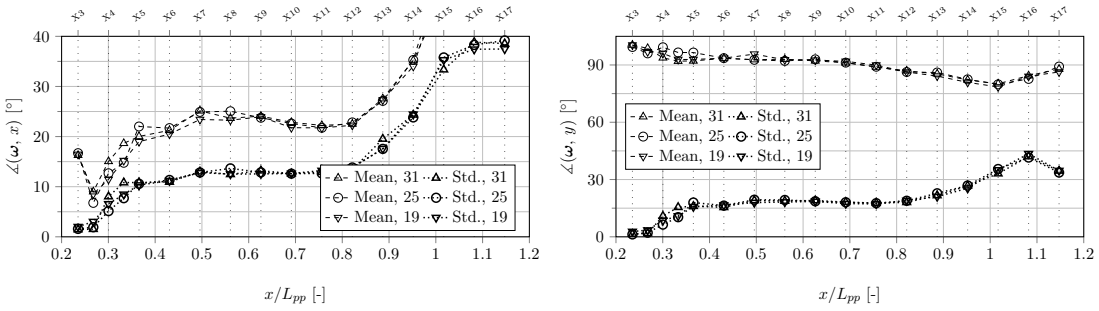

(a) Angle to x-axis.

(b) Angle to y-axis.

Figure B.17.: Vortex angle for different inflow speed, statistics of wandering-corrected vortex axis at centre 1.

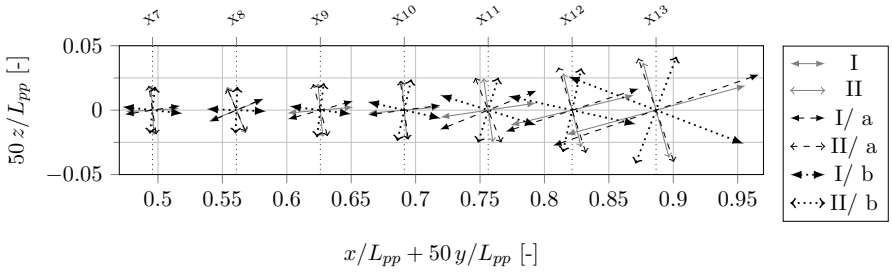

Figure B.18.: Principal axes of wandering displacement: major (I) and minor (II) axis at centre c1 for FSV, comparison of single- (in grey) and double-body model (in black, a, b).

and double-hull. These differences are attributed to the different averaging time. All in all, there is no distinct interaction between the FSV from the a- and b-part of the double-body model, a long-wave instability can be excluded.

B.7. Vortex Core Flow

Analytical Considerations Jacquin, Fabre, Geffroy et al. (2001) and Zeman (1995) proofed that a wandering motion of a laminar vortex creates stress and strain patterns observed in real flows, see also Fig.s 5.21, 5.22. Here, two exemplary results are shown that link to the FSV at X12 considering individual vortex parameters and wandering pattern. Wandering is limited to the in-plane displacement, vortex axis variations are omitted.

Fig. B.19 shows this relation for a vortex with the core parameters ($r_1 = 12$ mm, $V_{\theta 1} = 16$ m/s) of the FSV at X12 shown in Fig. 5.20 and the anisotropic wandering motion ($a_{I/II} = 2.53/\,1.67$ mm) according to Fig. 5.15.[2] Jacquin and colleagues provide

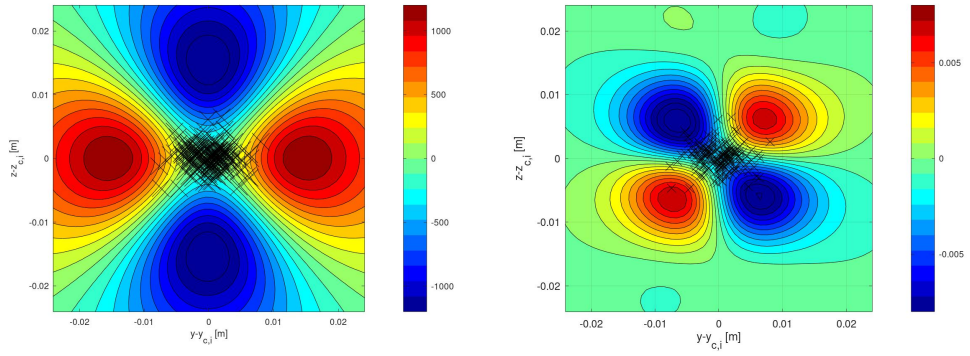

(a) Mean-strain rate $\left(U_{y,z} + U_{z,y}\right)$, unit [1/s].

(b) Reynolds-shear stress $\overline{u'_y u'_z}$, unit [m^2/s^2].

Figure B.19.: In-plane strain and stress field of a laminar q-vortex with wandering. The q-vortex is set to the core parameters at X12 and the wandering motion is statistically equal, the crosses indicate all instantaneous centres and reveal the small anisotropy.

the basic equations for this problem on page 12 in the above mentioned paper. Here, it is evaluated numerically to consider the anisotropic wandering.

An interesting effect is that the four-leaf clover (4LC) pattern occurs even for very small wandering amplitudes, e.g. in the range of $a/r_1 = 1e5$. The extreme values decrease with the amplitude, but not the locations of the extrema. So, even a very small wandering motion leads to the characteristic pattern.

Influence of Inflow Speed Figure B.20 visualises the approximate axial and transverse velocity of the FSV for varying inflow speed. The instantaneous fields represent the inhomogeneity of an LES solution. The transverse velocity U_z is an indication for the vortex breakdown, see also Fig. 5.7. In addition, it visualises that the inhomogeneity outside of the core is higher which is an indication for a decrease of turbulence intensity in the core.

[2] Subfigure c) shows the alignment of the major wandering axis has an angle of 12° to the y-axis, this is reproduced here.

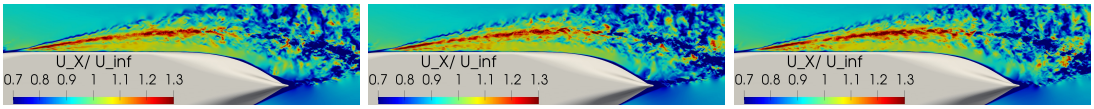

(a) Instantaneous axial flow U_x.

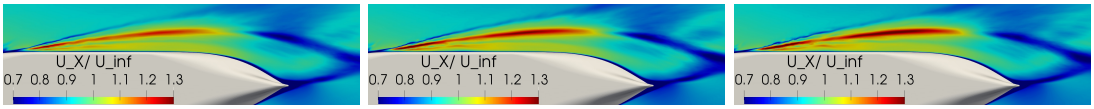

(b) Time-averaged axial flow $\overline{U}_x$.

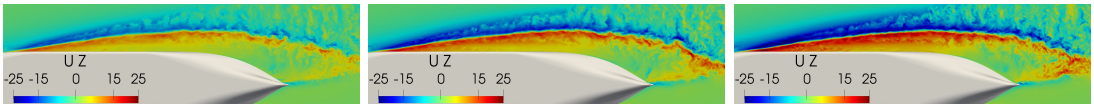

(c) Instantaneous transverse flow U_z.

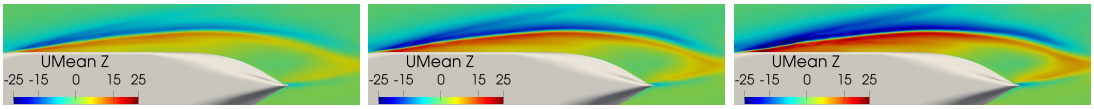

(d) Time-averaged transverse flow $\overline{U}_z$.

Figure B.20.: Instantaneous and time-averaged flow in plane through FSV, in addition to Fig. 5.27. From left to right: 19 m/s, 25 m/s and 31 m/s inflow speed.

B.8. Vortex Centre Flow

Different Representations for the Axial Flow According to Fig. B.21 the time-averaged projection onto the vortex axis U_{ax}, see Eq. B.5, and the velocity magnitude coincide. This follows already from the definition of the swirling flow centre: The transverse velocities approach zero. The x-velocity component differs very little, because the FSV is nearly parallel to the x-axis, see Fig.s 5.17 and B.16. However, wandering reduces the axial velocity most. A possible explanation is the unsteadiness of the vortex axis that reduces the axial component of a bulk velocity in x-direction. Another finding is that wandering-correction does not unveil a distinct increase, only a small one of about 5% right upstream of the breakdown. This indicates the absence of a coherent maximum that would be smeared during time-averaging. Instead, the axial velocity shows probably a high non-uniformity or in other words: high axial normal stresses.

All in all, one can state the U_{ax} contains an implicit correction for the variation of the vortex axis whereas U_x and $|\boldsymbol{U}|$ are corrected only for the displacement. From this point of view, the significant contribution of the axis variation becomes clear.

Different Centre Representations c1, c2, c3 The present paragraph compares different centre representations: the centre of the swirling flow inside the x-plane 'c1', the maximal vorticity magnitude 'c2' and the minimum pressure 'c3'.

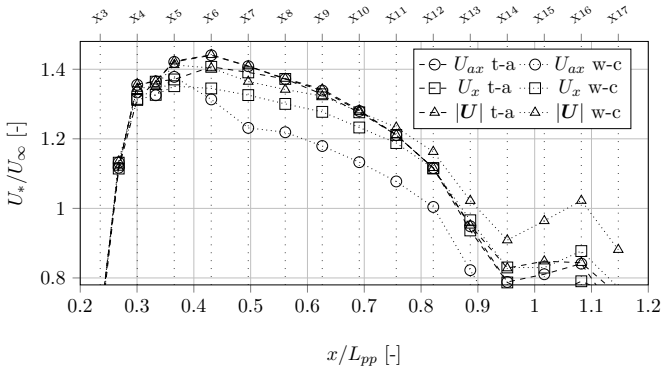

Figure B.21.: Influence of wandering on different representations for the 'axial' velocity at the swirling centre c1: projection onto vortex axis U_{ax}, x-component of velocity vector U_x and velocity magnitude $|\boldsymbol{U}|$. The dashed lines represent the time-averaged flow, the dotted ones the wandering-corrected flow.

A snapshot of the instantaneous flow of the FSV core in plane X11 in Fig. B.22 reveals the difference between the three centre representations. And this figure shows that the swirling flow is much more coherent than the vorticity field which shows several local extrema. The pressure field also has a distinct extremum.

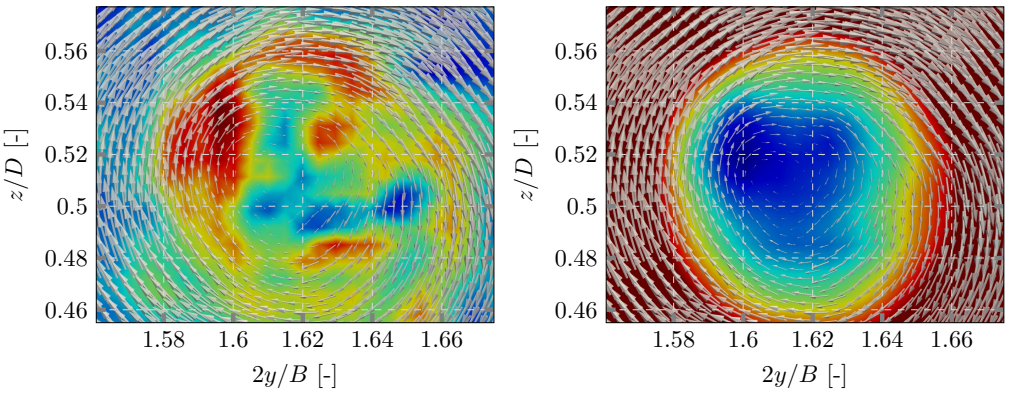

(a) Vorticity. (b) Pressure.

Figure B.22.: Exemplary visualisation of the different centre representations for the instantaneous core flow of the FSV at X11: swirling flow c1 with arrows as well as vorticity and pressure as contour plots.

Considering the FSV centre flow, Fig. B.23, the time-averaged curves coincide which follows from the same position. For the wandering-corrected flow a minor deviation occurs for the axial velocity, the pressure and the helicity. However, the vorticity reveals a distinct difference. This can be explained with the high gradients and the inhomogeneous field, see Fig. B.22.

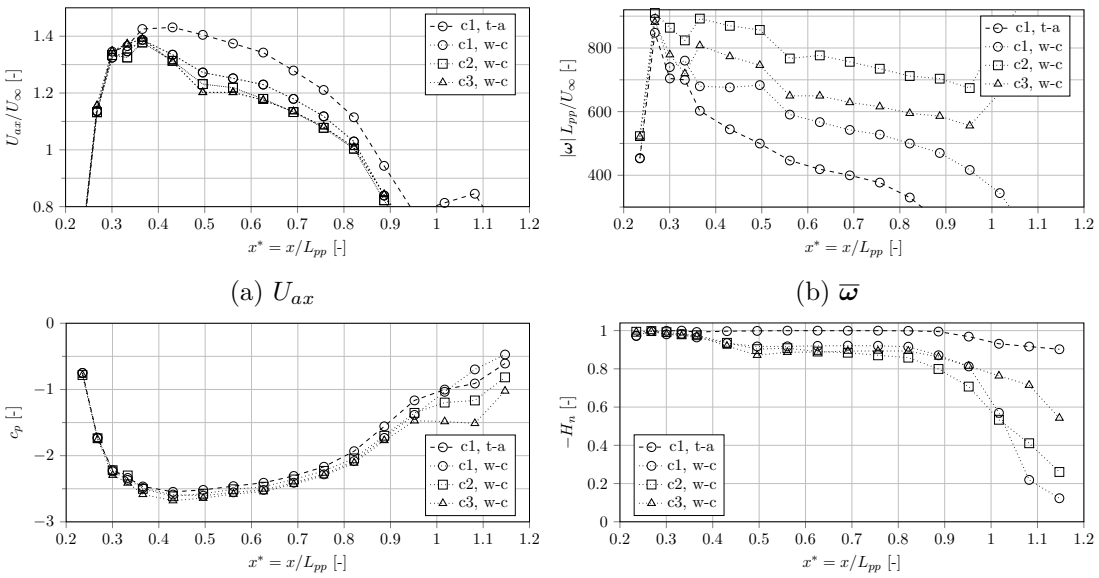

(a) U_{ax} (b) $\overline{\omega}$

(c) p (d) Hn

Figure B.23.: Flow at different centre representations for FSV: c1, c2 and c3.

Figure B.24 visualises the influence of different centre representations for the ABV. The wandering-corrected values differ larger than the time-averaged ones. Compared to the FSV, no coincidence can be observed for the wandering corrected flow. This is probably a consequence of the strong stern separation that leads to the emergence a highly complex core flow inside the ABV. In addition, the interaction with the FSV may influence the core flow.

Influence of Inflow Speed Figure B.25 reveals the insensitivity of the axial velocity at the ABV centre towards a variation of the inflow speed. This is the reason why only the FSV is investigated for different inflow speeds.

As Fig. B.26 indicates, the variation of the inflow speed has no influence on the position of the FSV breakdown near X13.

Referring to the visualisation presented in Anderson, Lawton (2001) (see also Sec. 2.2.3) Fig. B.27 indicates the missing linear relation between the relative axial centre velocity and the circulation parameter. For consistency, the time-averaged value of the velocity magnitude is selected. In accordance with Anderson and Lawton, the circulation parameter is calculated from the span which is twice the draught. Besides, a modification for the distinct 'tip' shape of the hull is not considered: the influence on the circulation parameter is very small and there is no influence on the linear relation to the relative axial velocity.

Influence of Double-Body Model Considering possible differences between the single- and double-body models, the FSV centre flow is shown in Fig. B.28 because the FSV is located closer to the symmetry plane than the ABV. The grey lines represent the single-body and both black lines the double-body: within an uncertainty of about 5% the difference between the single-body case and the 'right' and 'left' vortex vanishes. So the flow, including also the breakdown point, can be accurately described with a single-hull model.

Turbulence Properties Figure B.29 reveals the turbulent stresses and the resolved TKE for the different wandering-corrected centres c1 and c3. The time-averaged components are shown in Fig. 5.31. The trivial results in subfigure a are discussed for Fig. 5.31. They follow from the vanishing transverse velocity components at the swirling centre. For the pressure centre the normal in-plane components $\overline{u_y'^2}$ and $\overline{u_z'^2}$ differ from zero but are smaller compared to the time-averaged ones. This represents that the correlation between the swirling and pressure centre.

The turbulence properties for the ABV are shown in Fig.s B.30 and B.31. In accordance with previous observations for the FSV, TKE reduces for the wandering-corrected flow.

Figure B.32 shows that the Cartesian components and the velocity magnitude nearly coincide within the inertial subrange (between 300 and 5000 Hz). This represents the high degree of isotropy of the turbulent oscillations due to vortex stretching. Inside the energy-containing range (smaller than 300 Hz) the y- and z-components dominate. This may be an indication for the wandering motion: the in-plane velocity depends on the rotational vortex flow that changes at a lower frequency compared to changes of the axial velocity field that bear no clear link towards the vortex location.

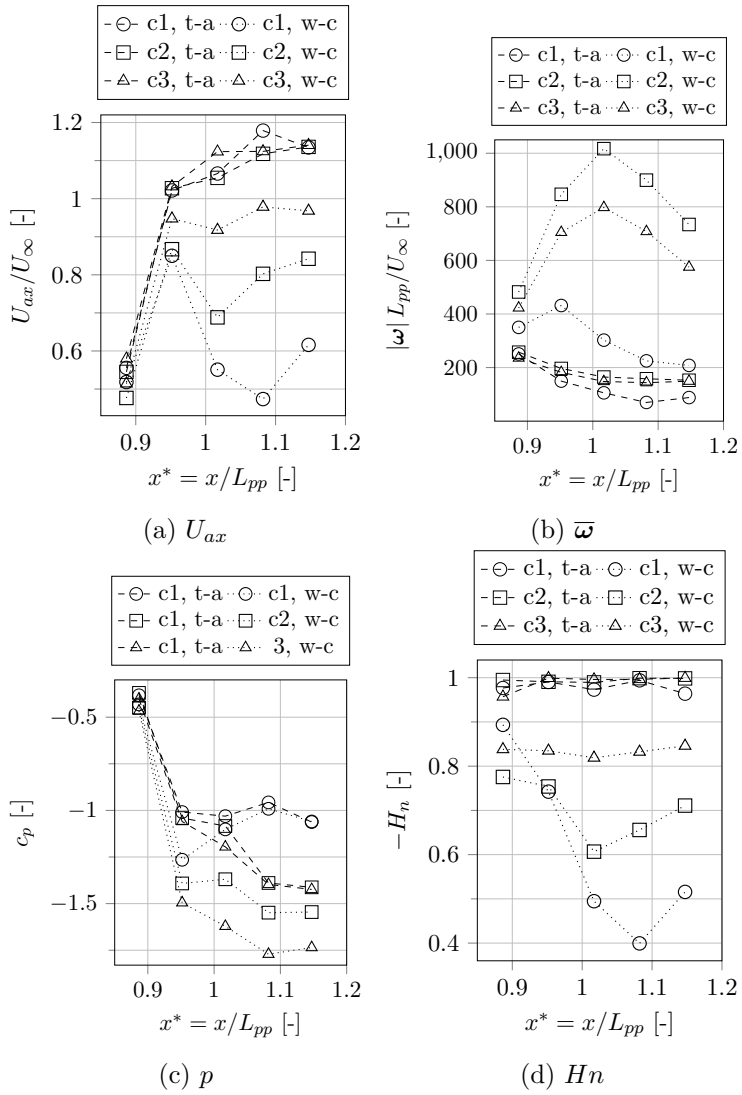

(a) U_{ax} (b) $\overline{\omega}$

(c) p (d) Hn

Figure B.24.: Flow at different centre representations for ABV: c1, c2 and c3, fine mesh.

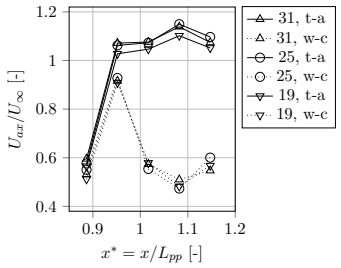

Figure B.25.: Axial velocity at ABV centre (c1) for varying inflow speed.

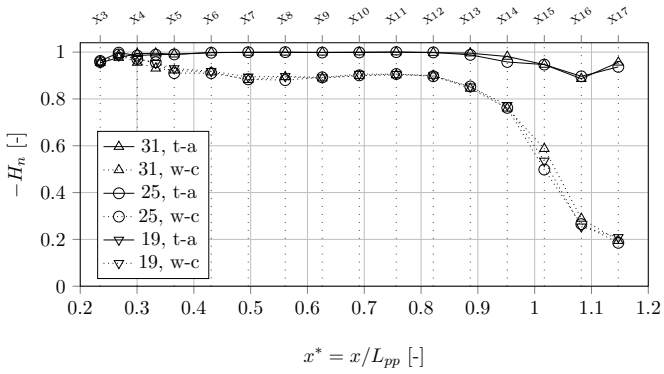

Figure B.26.: Helicity at FSV's centre (c1) for different inflow speed.

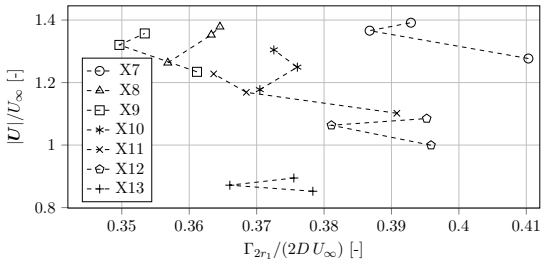

Figure B.27.: Relative axial velocity as a function of circulation parameter at selected x-planes, like in Anderson, Lawton (2001). Data from centre c1 and time-averaged velocity magnitude. All data is normalised with the associated inflow, e.g. $U_\infty = 19$ m/s for the slow inflow.

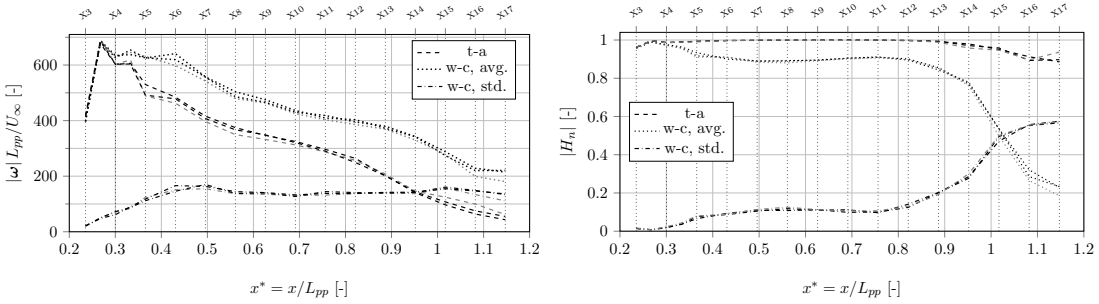

(a) Vorticity magnitude $\overline{\boldsymbol{\omega}}$.

(b) Helicity normalised Hn.

Figure B.28.: Flow at the FSV centre, for single-body in grey and double-body hull in black. (Medium mesh g2.)

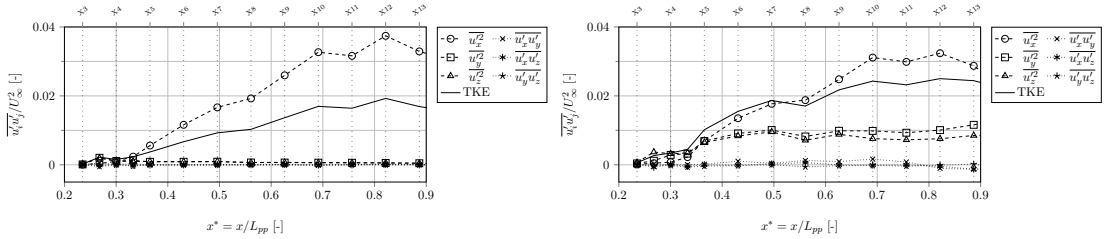

(a) Swirling centre c1.

(b) Pressure centre c3.

Figure B.29.: Turbulence at the FSV centre: wandering-corrected Reynolds-stress components and resolved TKE $k_r = \overline{u'_i u'_j}/2$.

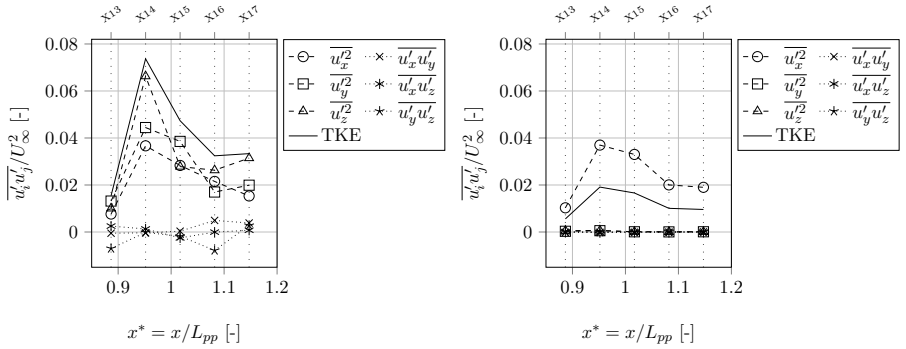

(a) Time-averaged for c1, see Fig. 5.33a.

(b) Wandering-corrected for c1.

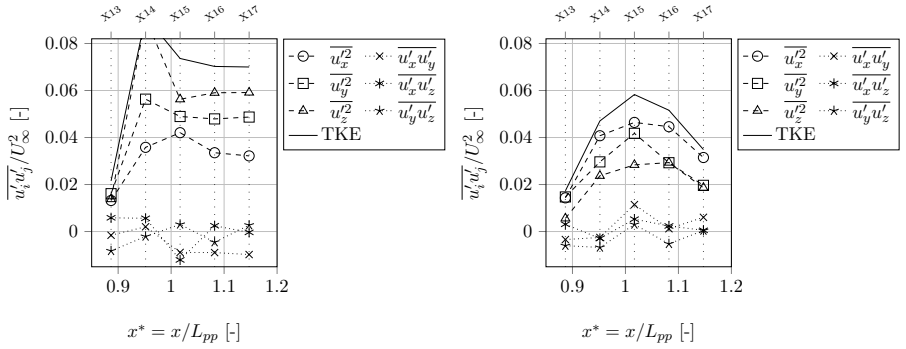

(c) Time-averaged for c3.

(d) Wandering-corrected for c3, see Fig. 5.33b.

Figure B.30.: Turbulence at the ABV centre: wandering-corrected Reynolds-stress components and resolved TKE $k_r = \overline{u'_i u'_j}/2$.

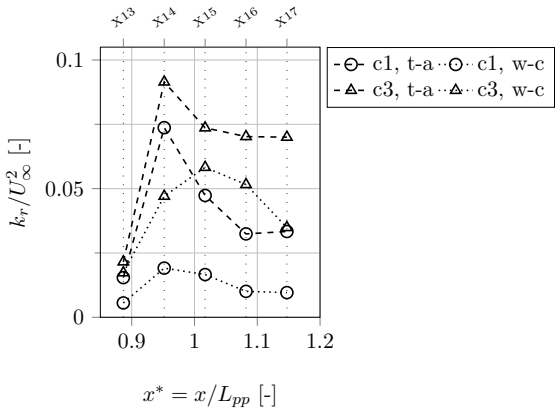

Figure B.31.: Turbulence at the ABV centre: time-averaged and wandering-corrected TKE.

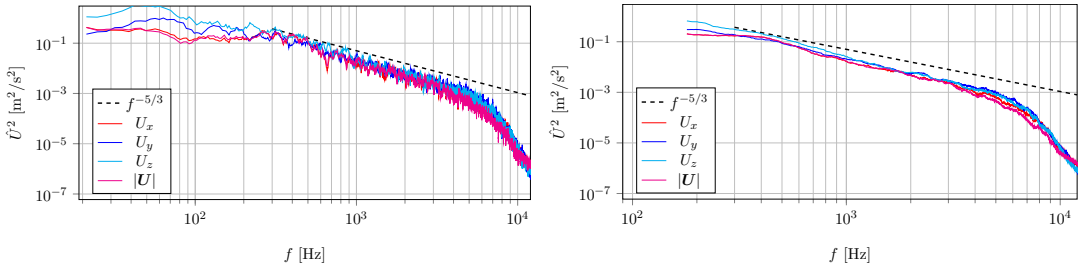

(a) Moving mean with 10 samples.

(b) Moving mean with 100 samples.

Figure B.32.: Turbulence energy spectrum (PSD) for different velocity components at FSV centre in plane X12. Slight differences to Fig. 5.35 originate from the different time range due to processing reasons.